Visible and Mid-Infrared Supercontinuum Generation and Their Respective Application to 3D Imaging and Stand-off Reflection Spectroscopy

by

Malay Kumar

A dissertation submitted in partial fulfillment
of the requirements for the degree of
Doctor of Philosophy
(Electrical Engineering)
in The University of Michigan
2011

Doctoral Committee:

Professor Mohammed N. Islam, Co-Chair
Professor Fred L. Terry Jr., Co-Chair
Professor Almantas Galvanauskas
Professor Michael J. Welsh

© Malay Kumar 2011

To my wife – *Nidhi*

ACKNOWLEDGEMENTS

I would like to begin by thanking my research advisor, Prof. Islam for his guidance and support over the course of my PhD. I would also like to thank my other committee members, Prof. Terry, Prof. Welsh and Prof. Galvanauskas for their valuable advice and insight.

I would also like to express gratitude to all my colleagues for the fruitful discussions I had with them in the lab: Vinay, Ojas, Zhao, Chenan, Kevin, Jeremiah and Mike.

Above all, I would like to thank my parents, my sister, and especially my wife, Nidhi, for their love and emotional support throughout this endeavor.

Table of Contents

Dedication **ii**
Acknowledgements **iii**
List of figures **vi**
List of tables **viii**
Abstract **ix**

Chapter 1: Introduction **1**
1.1 Visible supercontinuum generation 2
1.2 Application of visible SC to 3D imaging 3
1.3 Mid-IR SC generation 4
1.4 Application of mid-IR SC to spectroscopy 5
1.5 Significance of my doctoral research 7
1.5 Thesis layout 8

Chapter 2: Visible supercontinuum generation in photonic crystal fiber **11**
2.1 Introduction 11
2.2 Experimental setup 13
2.3 Experimental results 15
2.4 Numerical simulations 18
2.5 Discussion 21
2.6 Summary 23

Chapter 3: High resolution line-scan 3D imaging system for solder ball inspection **26**
3.1 Introduction 26
3.2 Experimental setup 28
3.3 System calibration 31
3.4 Experimental results 38
3.5 Discussion 43
3.6 Summary 44

Chapter 4: Mid-infrared supercontinuum generation in ZBLAN fiber **48**
4.1 Introduction 48
4.2 Experimental setup 50
4.3 Experimental results 52
4.4 Discussion 55
4.5 Summary 57

Chapter 5: Stand-off reflection spectroscopy using a mid-infrared supercontinuum source **60**
5.1 Introduction 60
5.2 Experimental setup – transmission spectroscopy 63
5.3 Experimental results – transmission spectroscopy 64
5.4 Experimental setup – reflection spectroscopy 68
5.5 Experimental results – reflection spectroscopy 73
5.6 Sample identification algorithm 79
5.7 Discussion 82
5.8 Summary 90

Chapter 6: Summary and future work **95**
6.1 Visible SC generation 95
6.2 Line scan 3D imaging 97
6.3 Experimental results 99
6.4 Discussion 101

LIST OF FIGURES

Fig. 1.1. Schematic of photonic crystal fiber structure 3
Fig. 1.2. Steps in flip chip bonding a ball grid array to an external circuit 4
Fig. 1.3. Loss spectra for common IR fiber glasses 5
Fig. 1.4. Mid-IR absorption bands of common chemical species 5
Fig. 1.5. Near-IR absorption bands of different molecular bonds 6
Fig. 2.1. All fiber integrated high power 1553 nm pump system 13
Fig. 2.2. Experimental setup for SHG and visible SC generation 14
Fig. 2.3. SHG efficiency versus peak pump power 15
Fig. 2.4. SC output spectrum from 1.5 m PCF for an input peak power of 420W 16
Fig. 2.5. SC spectral evolution as a function of input peak power 17
Fig. 2.6. SC average output power versus pulse repetition rate 17
Fig. 2.7. Comparison of experimental and simulation spectra for 1.5m PCF at 420W peak power 19
Fig. 2.8. Output after 0.3m PCF for different λ_0 (a) Simulation output (b) Theoretical MI power gain 21
Fig. 2.9. MI induced pulse break-up after propagation through 0.5m PCF with λ_0=745nm and 420W input peak power 21
Fig. 2.10. Spectra from two stage model: 0.5m 745 nm λ_0 PCF followed by ideal n_2 material 22
Fig. 2.11. Spectra from single stage model: 0.50-0.70m of 745 nm λ_0 PCF 22
Fig. 3.1. Solder ball grid array 27
Fig. 3.2. Experimental setup for visible SC based Fourier domain line scan interferometer 29
Fig. 3.3. Conversion from single CCD image to height profile along imaged line 31
Fig. 3.4. Experimental determination of coherence length 32
Fig. 3.5. 3D view of calibration step height standard measured by the line scan system 33
Fig. 3.6. Sample depth dependent decrease in system sensitivity 35
Fig. 3.7. 3D scan of steel ball bearing – (a) Polished ball - top view, (b) Polished ball - side view, ... 37
(c) Roughened ball - top view, (d) Roughened ball - side view 37
Fig. 3.8. 3D height map (microns) of solder ball grid array 39
Fig. 3.9. 3D view of solder ball defects –(a) Flat top, (b) Incomplete sphere, (c) Incorrect grid location 41
Fig. 3.10. 2D microscope view of solder ball defects – (a) Flat top, (b) Incomplete sphere, (c) Incorrect grid location 42

Fig. 3.11. Height map of 8 mm x 3.5 mm section of Lincoln's face on a copper penny 42
Fig. 3.12. 3D view of a size 4-20 screw head 42
Fig. 4.1. Experimental setup for mid-IR SC generation 50
Fig. 4.2. Copper heat sink with machined groove for power-amp gain fiber 51
Fig. 4.3. Power-amp efficiency versus peak power before and after optimized splice 53
Fig. 4.4. SC output from 9m ZBLAN fiber with 3.9W output power 54
Fig. 4.5. SC output from 9m ZBLAN fiber with 3.9W output power 55
Fig. 4.6. Schematic of ZBLAN fiber end-cap 56
Fig. 5.1. Experimental setup for SC based transmission spectroscopy 64
Fig. 5.2. Comparison of acetone transmission spectrum from SC and NIST database 66
Fig. 5.3. Comparison of ethanol transmission spectrum from SC and NIST database 66
Fig. 5.4. FTIR transmission spectrum of ammonium nitrate 68
Fig. 5.5. FTIR transmission spectrum of urea 68
Fig.5.6. Experimental setup for SC based stand-off diffuse reflection spectroscopy 69
Fig. 5.7. Chemical structure and formula of NESTT samples – TNT, RDX, PETN, Potassium nitrate 73
Fig. 5.8. Absorbance spectra of NESTT sample set #1 – TNT, RDX, PETN, Potassium Nitrate. 73
Fig.5.9. Reflection spectra of sample set #2 –Gypsym, Pine wood, Ammonium Nitrate, Urea. 76
Fig. 5.10. Reflection spectra of sample set #3 –automotive and military CARC paints 77
Fig.5.11 Variation of SC output at 4000 nm over 300 seconds. 78
Fig.5.12. Comparison of urea reflection spectrum obtained using the SC and FTIR 79
Fig. 5.13. Flowchart describing algorithm to demonstrate selectivity between two samples. 80
Fig. 5.14. Variation in predicted system SNR versus sample stand-off distance 85
Fig. 5.15. Definition of absorption band depth. 87
Fig. 6.1. Proposed experimental setup for visible SC generation using a 1060 nm Yb amplifier 96
Fig. 6.2. Design of a line scan system based hand-held waviness meter 98
Fig. 6.3. Mechanical mount for coupling power-amp output fiber to ZBLAN fiber 100
Fig. 6.4. Proposed dual beam detection setup for cancellation of SC fluctuations 102

LIST OF TABLES

Table 3.1. Performance metrics of line scan system 38
Table 3.2. Average solder ball heights and standard deviation over 10 independent scans..... 40
Table 4.1. Spectral power distribution of SC output 54
Table 5.1. Correlation table for sample set#1: NESTT - TNT, RDX, PETN, Potassium nitrate..... 81
Table 5.2. Correlation table for sample set #2: Ammonium nitrate, Urea, Gypsum, Pine wood 81
Table 5.3. Correlation table for sample set #3: Military CARC-green and auto-black, auto- red, and auto-green paints 81
Table 5.4. Comparison of optical stand-off detection techniques 89
Table 6.1. Expected specifications for a hand-held waviness meter 99

ABSTRACT

Visible and Mid-Infrared Supercontinuum Generation and Their Respective Application to 3D Imaging and Stand-off Reflection Spectroscopy

by

Malay Kumar

Co-Chairs: Mohammed N. Islam and Fred L. Terry Jr.

The thesis describes broadband supercontinuum (SC) generation in optical fibers for both the visible and mid-infrared regions of the spectrum, and their respective application to 3D imaging and stand-off reflection spectroscopy. Both SC sources leverage mature telecom technology, and are based on a common all-fiber integrated platform comprising a ~1.55 μm distributed feedback seed laser diode amplified to high peak powers in two stages of cladding pumped Erbium or Erbium-Ytterbium fiber amplifiers.

A visible SC extending from 0.45-1.20 μm with 0.74 W of time-averaged power is

demonstrated using a two step process. The output of the Er-Yb power amplifier is frequency doubled to ~0.78 μm using a periodically poled lithium niobate crystal, followed by non-linear spectral broadening in 2m of high nonlinearity photonic crystal fiber. Numerical simulations based on solving the generalized non-linear Schrödinger equation are also presented to verify the underlying SC generation mechanisms and predict further improvements.

The above SC source is used in a Fourier domain line scan interferometer to measure the height and identify shape defects of ~300 μm high solder balls in a ball grid array. The 3D imaging system has an axial resolution of ~125 nm, transverse resolution of ~15 μm, and an angular measurement range between 20 to 60 degrees depending on the sample surface roughness.

The mid-infrared SC source is generated by pumping a 9m long ZrF_4-BaF_2-LaF_3-AlF_3-NaF (ZBLAN) fiber to obtain a spectrum spanning 0.8-4.3 μm with 3.9 W time-averaged power. The output power is linearly scalable with pump power, but requires optimization of the critical splices and thermal management of the gain fiber and pump diodes to ensure stable high power operation.

Finally, an application of the mid-IR SC is demonstrated by measuring the diffuse reflection spectra of solid samples at a stand-off distance of 5 m and 100 ms integration time. The samples can be distinguished using a correlation algorithm based on distinct spectral features in the reflection spectrum. Signal to noise ratio calculations show that the distance is limited by space constraints in our lab and can be extended to ~150 m.

Chapter 1

Introduction

Supercontinuum (SC) generation is a process in which a narrow bandwidth laser undergoes substantial spectral broadening through an interplay of several non-linear phenomena such as modulation instability, self phase modulation, four wave mixing, stimulated Raman scattering etc. In essence, the SC source combines the broad bandwidth of a lamp type source with the high spectral power density and spatial coherence of a conventional monochromatic laser. SC generation was first observed in the early 70s and has since has been widely studied using a variety of laser sources and non-linear materials [1-6].

The work performed in this thesis will focus on SC generation in both the visible and mid-infrared spectral regions using two distinct non-linear fibers for each case. An optical fiber was chosen as the non-linear broadening element for two reasons. First, light in an optical fiber is confined within a small core region that enables the generation of high intensities. Second, the wave guiding nature of a fiber allows the use of long fiber lengths. Since the non-linear mechanisms responsible for spectral broadening are dependent on both the light intensity and interaction length within the material [7], an optical fiber enables the generation of much stronger non-linear effects compared to a free space beam focused through a sample.

The type of fiber chosen for SC generation depends on many factors. First, the fiber type must have low loss in the wavelength region that the continuum is expected to cover. This enables the use of longer fiber lengths for obtaining larger non-linear effects. Second, it is preferable to have a fiber with large nonlinear coefficient $\gamma = (2\pi n_2)/(\lambda A_{eff})$ where n_2 is the non-linear refractive index of the fiber glass material and A_{eff} is the effective mode area of the guided light in the core. For a given wavelength and material system, one can choose a single mode fiber with a small core size for enhanced SC generation. Finally, the dispersion properties of the fiber also affect the shape and extent of the generated continuum [8,9]. By pumping the fiber in the normal dispersion regime, the SC generation is dominated by self phase modulation while pumping the fiber in the anomalous dispersion regime generates an SC dominated by modulation instability and soliton self frequency shift.

We developed a laser source in the 1.55 μm wavelength range to take advantage of the wide availability of economical components such as seed lasers, fiber amplifiers, pump laser diodes, isolators, filters and couplers for the telecommunications industry. The result was an all-fiber integrated laser that provided both high average power and high peak power pulses suitable for broad SC generation [10,11]. The same platform was used for both the visible and mid-IR SC generation with a different non-linear fiber in each case. In the case of the visible SC experiments, an additional frequency doubling stage was added to shift the pump wavelength to ~0.78 μm to begin the SC generation process closer to the target wavelength range [12].

1.1 Visible SC generation

For SC generation in the visible region of the spectrum, we choose photonic crystal fibers (PCF) as the non-linear medium. These fibers are comprised of a solid glass high index core embedded in an air-filled cladding structure where a number of air holes are arranged in a pattern that runs along the length of the fiber creating a hybrid air-silica material with a refractive index lower than the core. A schematic of such a fiber is shown

in figure 1.1 [13]. By controlling the ratio of the hole size d to hole pitch Λ, the dispersion properties of the fiber can be tailored [8]. While the lowest possible zero dispersion wavelength (ZDW) in conventional fused silica fibers is ~1300 nm and limited by the material dispersion, PCFs can have ZDW as low ~650 nm. This allows for pumping in the anomalous dispersion regime using light sources in the ~800 nm range such as mode locked Ti:sapphire lasers or frequency doubled Erbium fiber lasers.

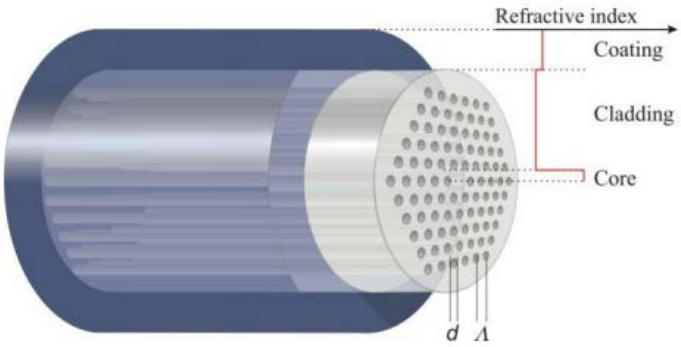

Fig. 1.1. Schematic of photonic crystal fiber structure

1.2 Application of visible SC to 3D imaging

After development of the visible SC source, we wanted to demonstrate an application of the above source to a relevant industrial problem. Since this part of my research was funded by NIST under the Advanced Technology Program on “2 micron manufacturing and machining”, we chose to demonstrate a sub-micron axial resolution 3D imaging system using the visible SC source. In addition, the availability of high sensitivity silicon CCD cameras for the visible region of the spectrum made imaging a natural choice for an application of the SC laser.

The predominant use of SC lasers in imaging has been in the field of optical coherence tomography [14-18] which provides depth resolved images of biological tissues. Since the axial resolution of OCT systems is inversely proportional to the bandwidth of the light source used [19], the advent of broadband SC generation paved the way for replacement of low spatial coherence sources such as white light lamps with the new SC sources. The 3D imaging system demonstrated in this thesis is based on the same

interferometric principles as OCT. However, due to the non transparent nature of the sample, it produces a 3D map of just the sample top surface instead of lower layers as in the case of tissues. The SC source was used in a Fourier domain line scan interferometer configuration to produce high resolution 3D images of both flat and curved surfaces.

We chose a solder ball grid array (BGA) used in the semiconductor industry as the sample of interest for the 3D line scan imaging system. Due to an increased density of chips on a wafer, conventional wire leads on a chip are being replaced with the lower area footprint ball grid arrays. Figure 1.2 shows the steps involved in flip chip bonding the BGA to an external circuit using the solder balls to complete the electrical connection. Since the reliability of the electrical contact depends on the uniformity of height and shape of these balls, the 3D inspection of the BGA is essential for quality control.

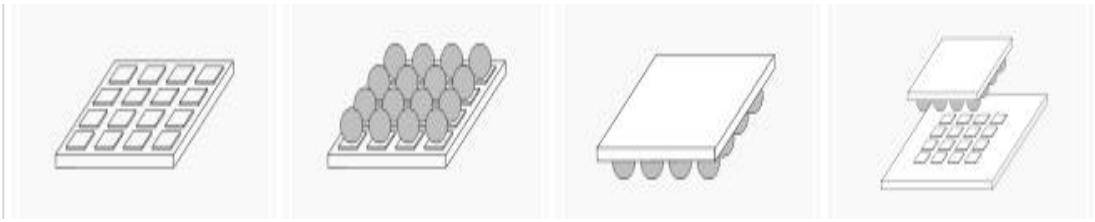

Fig. 1.2. Steps in flip chip bonding a ball grid array to an external circuit

1.3 Mid-IR SC generation

The choice of fiber for mid-IR SC generation was based primarily on the fiber loss curves (Fig.1.3) for the different IR transparent fibers [20]. The figure shows that for SC generation in the 1-4 μm wavelength range, fluoride fiber is the best candidate. While the other IR fibers also suffered from drawbacks such as handling difficulties due to the brittle nature, photo-degradation and inability to manufacture long lengths, the fluoride fiber did not suffer from these problems and was chosen due to relative maturity of its technology compared to others. In particular, the fluoride fiber used in our experiments was based on the ZBLAN (ZrF_4-BaF_2-LaF_3-AlF_3-NaF) glass, which is considered the most stable of all fluoride glasses [21].

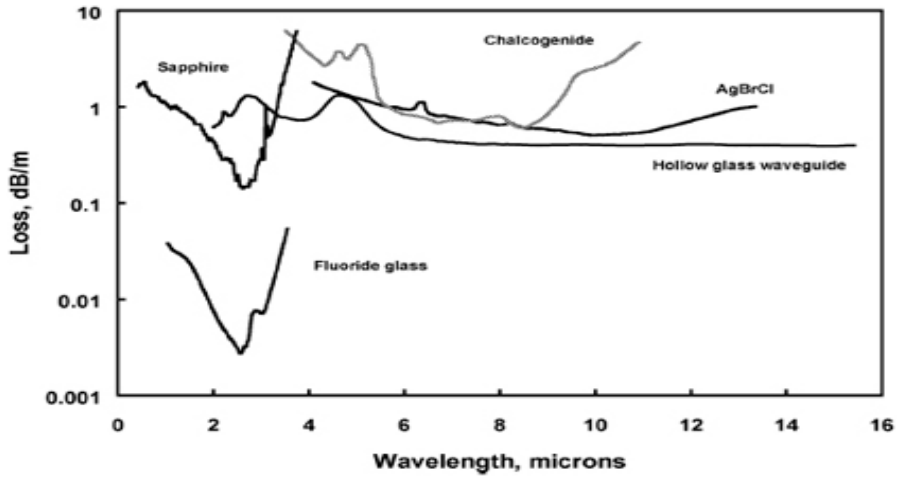

Fig. 1.3. Loss spectra for common IR fiber glasses

1.4 Application of mid-IR SC to spectroscopy

The broadband SC source is ideally suited for the spectroscopic identification of unknown samples due to the large number of distinct spectral fingerprints in the mid-IR region of the spectrum associated with the rotational and vibrational structure of the molecule. Figure 1.4 [22] shows the absorption bands of some common chemical species in the 2-11 μm range while Fig. 1.5 [23] describes the chemical bonds responsible for absorption lines in the near-IR range from 0.7-2.5 μm.

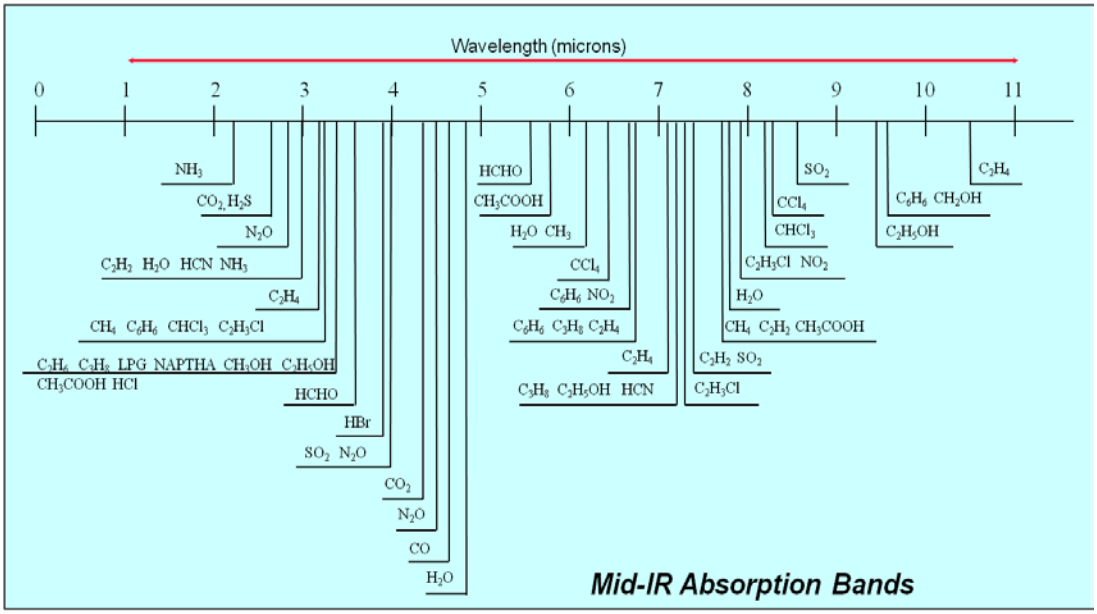

Fig. 1.4. Mid-IR absorption bands of common chemical species

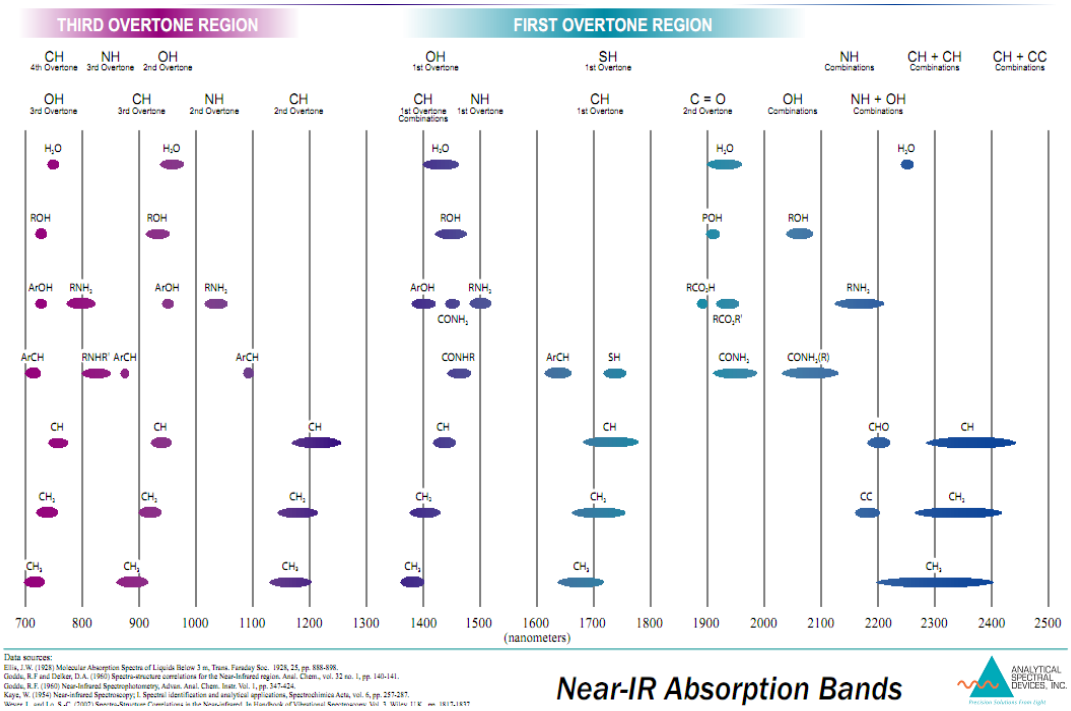

Fig. 1.5. Near-IR absorption bands of different molecular bonds

We chose stand-off detection of solid samples using diffuse reflectance spectroscopy (DRS) [24,25] as the relevant application to demonstrate the capabilities of the mid-IR SC source. While DRS using solar illumination has been used for many decades in the field of remote sensing [26] and hyper-spectral imaging [27], the use of an active light source such as the SC enables newer applications of the well established technique [28,29]. While the broad SC bandwidth (800-4300 nm) allows for the detection of various species (high selectivity), the high SC output power (3.9W) and single mode beam quality enables the measurement of the samples from a large stand-off distance (high sensitivity). Due to the growing need of the homeland security and defense industries in remote detection of dangerous substances [30], our test samples included fertilizers such as ammonium nitrate and urea that are used for making homemade bombs in addition to conventional explosives such as TNT, RDX and PETN. We also measured the spectral signatures of automotive and military grade paints. The wide range of samples measured are just a few examples that demonstrate the feasibility of the technique.

1.5 Significance of my doctoral research

The research performed in our group led by Prof. Islam is focused on supercontinuum generation in optical fibers, and its applications in a wide range of fields. Initial work performed by my colleagues Dong-Joon Lee and Chenan Xia was based on SC generation in the near-IR using high nonlinearity fused silica fibers. With the help of Dr. Mike Freeman, detailed simulation models were developed, which explained the underlying mechanisms behind the SC generation process. Later, the SC generation was extended to the mid-IR using ZBLAN fibers, and power scaling of the output power was demonstrated using cladding pumped fiber amplifiers.

Using the above research as a starting point, I developed a SC source in the visible region of the spectrum, and also extended the spectral range of the previously demonstrated mid-IR SC source. My research on visible SC generation was a significant contribution to the field, since it was the first to demonstrate SC generation in the visible region of the spectrum using a near-IR telecommunication laser source. Compared to existing systems using bulky and complicated mode-locked Ti-sapphire lasers, our system was based an all-fiber, compact and power-scalable laser source using Erbium-Ytterbium fiber amplifiers. Our research group believes that a true test of the performance of a newly developed laser is demonstrating its use in an application. In order to leverage the wide bandwidth of the source, we picked sub-micron resolution 3D imaging of solder ball grid arrays as the application of choice. The novelty of the demonstrated system was its unique ability to measure both height and shape information of non-flat surfaces.

The latter half of my research was based on increasing the output power in the long wavelength bands of the existing mid-IR SC source in our lab. Through a re-design of the power-amplifier stage, careful optimization of splices, and improved thermal management of the various components, I was able to demonstrate a SC extending out to 4.3 μm with >500 mW average power in the long wavelength band >3.8 μm. In

comparison, the previously version of the SC source in our lab only had ~10 mW average power in the same spectral band. However, my primary contribution was the development of a mid-IR SC based stand-off detection system using diffuse reflection spectroscopy. The previous demonstrations of the use of SC sources in spectroscopy have been limited to transmission spectroscopy of gases [31] in the near-IR. We believe that our research is the first to demonstrate stand-off (up to ~150m) reflection spectroscopy on solid targets covering both the near and mid-IR regions of the spectrum.

1.6 Thesis layout

The different chapters in my thesis are organized as follows. Chapter 2 demonstrates a power scalable visible SC source from 0.45-1.20 μm with 0.74W average output power. Numerical simulations are performed to confirm the underlying SC generation mechanisms and to predict new methods to increase the SC bandwidth. In chapter 3, the visible SC source from chapter 2 is used to demonstrate a line scan 3D imaging system with ~125 nm axial and ~15 μm transverse resolution. In particular, the Fourier domain interferometry based system is used for inspection of ~300 μm high semiconductor solder ball grid arrays to determine the ball height along with shape defects of the ball top. Next, mid-IR SC generation in ZBLAN fibers with an output spanning 0.8-4.3 μm and 3.9W average output power is described in chapter 4. The application of the above source for stand-off detection of solid samples using diffuse reflection spectroscopy is shown in chapter 5. The different samples are distinguished using a correlation algorithm that is based on the unique spectral features in the reflection spectrum of each sample. Finally, the results of the previous four chapters are summarized in chapter 6 and the scope for improvement and future work is also discussed.

References

1. R. R. Alfano, “The supercontinuum laser source: fundamentals with updated references,” 2nd ed., Springer, New York (2006)
2. J. M. Dudley, G. Genty, and S. Coen, “Supercontinuum generation in photonic crystal fiber,” Rev. Mod. Phys. 78, 1135-1184 (2006)
3. G. Genty, S. Coen, and J. M. Dudley, "Fiber supercontinuum sources (Invited)," J. Opt. Soc. Am. B **24**, 1771-1785 (2007)
4. A.M. Zheltikov, “Let there be white light: supercontinuum generation by ultrashort laser pulses,” Physics-Uspekhi **49**, 605-628 (2006)
5. Q. Lin, O. J. Painter, and G. P. Agrawal, "Nonlinear optical phenomena in silicon waveguides: modeling and applications," Opt. Express **15**, 16604-16644 (2007)
6. S.L. Chin, S.A. Hosseini, W. Liu, Q. Luo, F. Theberge, N. Akozbek, A. Becker, V.P. Kandidov, O.G. Kosareva, H.Schroeder, “The propagation of powerful femtosecond laser pulses in optical media: physics, applications and new challenges,” Canadian Journal of Physics **83**, 863-905 (2005)
7. G. P. Agrawal, Nonlinear Fiber Optics, 3rd edition, (Academic, San Diego, 2001).
8. Philip St.J. Russell, "Photonic-Crystal Fibers," J. Lightwave Technol. **24**, 4729-4749 (2006)
9. S. Smirnov, J.D. Ania-Castanton, T.J. Ellingham, S.M. Kobtsev, S. Kukarin, S.K. Turitsyn, “Optical spectral broadening and supercontinuum generation in telecom applications,” Opt. Fiber Tech. **12**, 122-147 (2006)
10. C. Xia, M. Kumar, O. P. Kulkarni, M. N. Islam, F. L. Terry, Jr., M. J. Freeman, M. Poulain, and G. Mazé, "Mid-infrared supercontinuum generation to 4.5 μm in ZBLAN fluoride fibers by nanosecond diode pumping," Opt. Lett. **31**, 2553-2555 (2006)
11. C. Xia, M. Kumar, M.Y. Cheng, O.P. Kulkarni, M.N. Islam, M.N, A. Galvanauskas, F.L. Terry, M.J. Freeman, D.A. Nolan, W.A. Wood, "Supercontinuum Generation in Silica Fibers by Amplified Nanosecond Laser Diode Pulses," IEEE J. Sel. Top. Quant. Elec. **13**, 789-797 (2007)
12. M. Kumar, C. Xia, X. Ma, V.V. Alexander, M.N. Islam, F.L. Terry, C. Aleksoff, A. Klooster, D. Davidson, "Power adjustable visible supercontinuum generation using amplified nanosecond gains-witched laser diode," Opt. Express **16**, 6194-6201 (2008)
13. NKT Photonics, http://www.nktphotonics.com
14. D. Huang, E.A. Swanson, C.P. Lin, J.S. Schuman, W.G. Stinson, W. Chang, M.R. Hee, T. Flotte, K. Gregory, C.A. Puliafito, J.G. Fujimoto, “Optical Coherence Tomography,” Science **254**, 1178-1181 (1991)
15. A.F. Fercher, W. Drexler, C.K. Hitzenberger, T. Lasser, “Optical coherence tomography – principles and applications”, Reports on Progress in Physics **66**, 239-303 (2003)
16. J.M. Schmitt, “Optical coherence tomography: A Review”, IEEE J. Sel. Top. Quant.

Elec. **5**, 1205-1215 (1999)
17. D.L. Marks, A.L. Oldenburg, J.J. Reynolds, S.A. Boppart, "Study of an ultrahigh-numerical-aperture fiber continuum generation source for optical coherence tomography," Opt. Lett. **27**, 2010-2012 (2002)
18. A. Unterhuber, B. Povazay, K. Bizheva, B. Hermann, H. Sattmann, A. Stingl, T. Le, M. Seefeld, R. Menzel, M. Preusser, H. Budka, C. Schubert, H. Reitsamer, P.K. Ahnelt, J.E. Morgan, A. Cowey, W. Drexler, "Advances in broad bandwidth light sources for ultrahigh resolution optical coherence tomography", Phys. in Med. And Biology **49**, 1235-1246 (2004)
19. R. Leitgeb, C. Hitzenberger, and Adolf Fercher, "Performance of fourier domain vs. time domain optical coherence tomography," Opt. Express **11**, 889-894 (2003)
20. J.A. Harrington, "Infrared Fibers," in *Handbook of Optics: Fiber and Integrated Optics*, Vol. 4, M. Bass, J. M. Enoch, E. W. Van Stryland, and W. L. Wolfe, Eds., McGraw-Hill, New York (2000)
21. I.D. Aggarwal, G. Lu, *Fluoride Glass Fiber Optics*, Academic Press, New York (1991)
22. J.S. Sanghera, I.D. Aggarwal, *Infrared fiber optics*, CRC Press, Boca Raton (1998)
23. Analytical Spectral Devices Inc., http://www.asdi.com
24. E. L. Simmons, "Diffuse reflectance spectroscopy: a comparison of the theories," Appl. Opt. **14**, 1380-1386 (1975)
25. K. Krishnan, S.L. Hill, R.H. Brown, "FTIR spectroscopy using diffuse reflectance and a diamond cell", American Laboratory **12**, 104-106 (1980)
26. J.L. Roujean, M. Leroy, P.Y. Deschamps, "A bidirectional reflectance model of the earth's surface for the correction of remote sensing data", Journal of geophysical research-Atmospheres **97**, 20455-20468 (1992)
27. E.A. Cloutis, "Hyperspectral geological remote sensing: Evaluation of analytical techniques", International journal of Remote Sensing **17**, 2215-2242 (1996)
28. Y. Chen, E. Raikkonen, S. Kaasalainen, J. Suomalainen, T. Hakala, J. Hyyppa, R. Chen, "Two-channel hyperspectral LIDAR with a supercontinuum laser source", Sensors **10**, 7057-7066 (2010)
29. O.L. Muskens and A. Lagendijk, "Broadband enhanced backscattering spectroscopy of strongly scattering media," Opt. Express **16**, 1222-1231 (2008)
30. S. Wallin, A. Pettersson, H. Ostmark, A. Hobro, "Laser-based standoff detection of explosives: a critical review", Anal. and Bioanal. Chem. **395**, 259-274 (2009)
31. D.M. Brown, K. Shi, Z. Liu, C. R. Philbrick, "Long-path supercontinuum absorption spectroscopy for measurement of atmospheric constituents," Opt. Express **16**, 8457-8471 (2008)

Chapter 2

Visible supercontinuum generation in photonic crystal fiber

2.1 Introduction

Visible SC generation in photonic crystal fibers has been widely studied using a variety of pump sources [1]. Mode-locked Ti:sapphire femtosecond lasers around ~750 nm produce SC covering the visible, but these sources are expensive and have limited average power output. Higher SC average power outputs in excess of a watt have been obtained by pumping with mode locked picosecond pulses from a Yb fiber laser at 1060 nm [2,3]. Various techniques have been demonstrated to extend the SC spectrum towards the blue. Supercontinuum extending down to 400 nm was demonstrated using a microchip laser at 1064 nm to pump a PCF with modified group index in the infra red to efficiently phase match with deeper blue wavelengths [4]. Another method as demonstrated by Kudlinski et. al. was used to generate SC with a short wavelength edge of 400 nm and >2 mW/nm spectral density by using tapers with continuously decreasing dispersion [5]. Multi-wavelength pumping schemes involving a pump and its second harmonic [6] or four wave mixing pump conversion [7] have also been demonstrated to increase spectral coverage in the visible.

The techniques mentioned above using mode locked lasers suffer from one primary drawback – lack of average power scalability due to fixed repetition rate. The ability to vary the pulse repetition rate is inherent to many SC systems using microchip lasers [7,8] and master oscillator power amplifier type pumps. For example, Matos et. al. demonstrated a repetition rate tunable chirped pulse amplification erbium system which was frequency doubled to generate SC in PCF with 160 mW average power [9]. However, the control of the SC average power by varying the repetition rate while keeping the peak power constant has not been demonstrated earlier. In this chapter, a simple nanosecond source based on frequency doubling amplified gain switched pulses from a standard 1.55 μm telecom laser diode is demonstrated as a robust alternative to mode-locked laser based setups.

An overview of the key results obtained in this chapter is described below. We demonstrate generation of a power-scalable visible supercontinuum (SC) source extending between 0.45-1.2 μm with up to 0.74 W average power. The SC is obtained by pumping a 1.5 m long photonic crystal fiber (PCF) with a frequency doubled, amplified, gain-switched, telecom laser diode. By controlling the non-linearity in the amplifier, the SC output is scalable in average power through an increase in the pulse repetition rate while maintaining a constant peak power. The continuum generation is initiated by modulation instability (MI), and simulations verify that the broadest spectrum is generated by pumping in the anomalous dispersion regime close to the PCF zero dispersion wavelength (λ_0). By leveraging mature telecom technology, the demonstrated SC source is economical, compact and robust. The broad spectrum and average power control make the SC source particularly useful for applications in optical coherence tomography and surface metrology.

The layout of the chapter is as follows. Section 2.2 describes details of experimental setup used to generate the visible SC. The experimental results showing evolution of the SC spectrum with peak power and power scalability of the SC output are shown in

section 2.3. In section 2.4, numerical simulations of the non-linear Schrödinger equation are performed to determine the SC generation mechanisms and understand the limits of the wavelength edge. Finally, section 2.5 discusses a new method to extend the short wavelength edge using a two stage SC generation process. The first stage uses MI to produce high peak power femtosecond pulses while the second stage uses a low dispersion but high non-linearity material to achieve large spectral broadening through self phase modulation.

2.2 Experimental setup

A block diagram of the all fiber integrated high power pump system at 1.55 μm is illustrated in Fig. 2.1. A 1553 nm DFB laser diode is driven by a pulse generator to produce 2 ns pulses at variable repetition rates and amplified using dual stage fiber amplifiers. The first stage consists of a 1 m long 4/125 μm Erbium doped fiber amplifier (EDFA) forward pumped by a 400 mW 980 nm single mode laser diode. In order to improve the noise performance of the system, the amplified spontaneous emission (ASE) generated by the first stage amp is filtered using a 100 GHz band pass filter centered at the seed laser wavelength. An isolator between the two gain stages prevents damage to the components in the pre-amp from backward propagating light in the power-amp stage. The power-amp stage comprises a 5m long 7/125 μm cladding pumped Erbium-Ytterbium co-doped fiber amplifier (EYFA) backward pumped by two 8W 976 nm multimode laser diodes coupled into the gain fiber via a 6+1:1 pump combiner. At the highest operating repetition rate of 1 MHz, the power-amp produced an output of 3.2W average power (1.6 kW peak power).

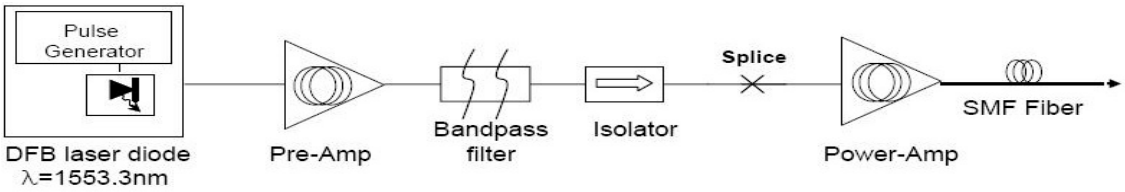

Fig. 2.1. All fiber integrated high power 1553 nm pump system

The light at 1553 nm is then frequency doubled using a periodically poled lithium niobate (PPLN) crystal before being coupled into the PCF. The experimental setup for the second harmonic generation process (SHG) followed by visible SC generation is shown in Fig. 2.2. A quarter wave plate and half wave plate at the output of the power-amp are used to adjust the polarization state of the light. The light then passes through a free space optical isolator before being coupled into a 10 mm long PPLN crystal temperature stabilized at 160C. The crystal temperature and the spot size of the focused beam within the PPLN are optimized for maximum SHG efficiency.

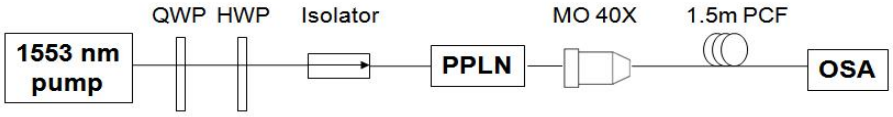

Fig. 2.2. Experimental setup for SHG and visible SC generation

Since the PPLN crystal has a limited doubling bandwidth of ~1 nm, spectral broadening in the amplifier reduces the SHG efficiency. To reduce non-linearity, the length of the SMF-28 output fiber in the power-amp was shortened to ~0.5 m. Next, the input peak power was varied to obtain maximum SHG efficiency ~70% at 1 kW (Fig. 2.3). The theoretical efficiency for a lossless crystal at the given peak power is ~99%. But, the transmission loss through the crystal at low power was measured to be ~30%, and thus the maximum conversion efficiency possible experimentally was achieved. With a further increase in peak power, the efficiency starts to drop as the amplifier output spectrum broadens and more power shifts outside the 1 nm conversion bandwidth of the crystal.

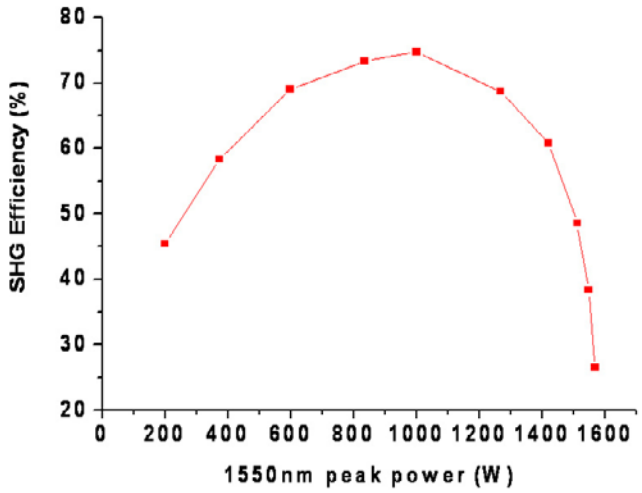

Fig. 2.3. SHG efficiency versus peak pump power

The frequency doubled output from the PPLN at 776.5 nm acts as the pump source for continuum generation in the PCF. The light is then coupled into a 1.5 m long PCF (core diameter = 1.9 μm, λ_0 = 745 nm, dispersion slope at λ_0 = 0.85 ps.nm^{-2}km^{-1}) with ~50% coupling efficiency using a 40X microscope objective. The output spectrum is recorded using an optical spectrum analyzer with a 2 nm resolution.

2.3 Experimental results

The output spectrum from the PCF for a pump (776.5 nm) peak power of 420 W is shown in Fig. 2.4. The continuum extends from 450-1200 nm with 0.74 W time averaged power. The spectrum is smooth from 550-750 nm with better than 2dB flatness across this wavelength range. Apart from the peak at the pump wavelength, several addition peaks can be observed in the output spectrum. The peak at ~518 nm is due to third harmonic generation from the PPLN, while the peak at ~388 nm arises from phase matched four wave mixing. To calibrate the vertical axis of the spectrum, the area under the spectral curve was numerically computed and equated to the total SC power as determined by a thermal power meter.

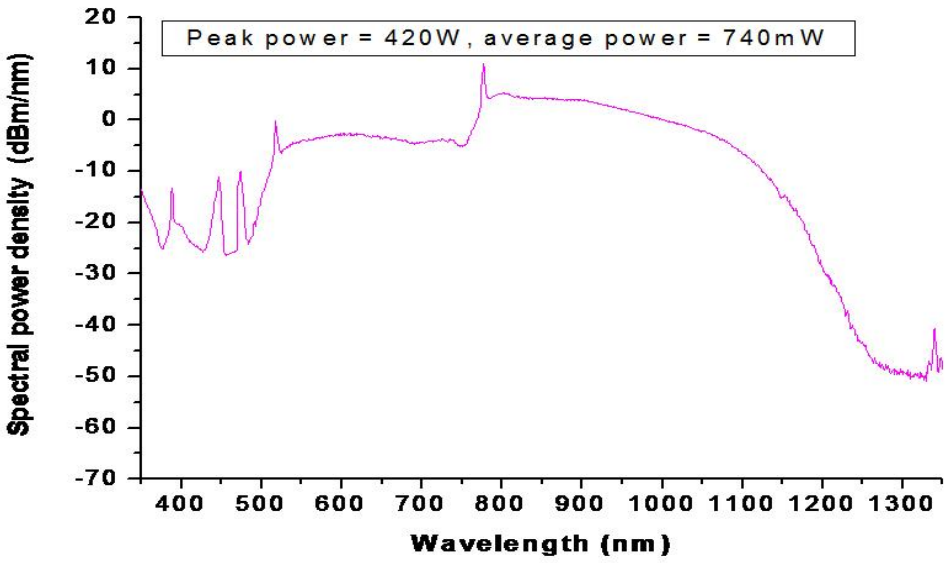

Fig. 2.4. SC output spectrum from 1.5 m PCF for an input peak power of 420W

Next, the SC spectral evolution as a function of input peak power was studied (Fig. 2.5). Since the fiber is pumped with nanosecond pulses in the anomalous dispersion region, we expect the SC growth to be initiated by MI [8,10]. In the time domain, this implies that the 2 ns pulse breaks up into a train of periodic femtosecond solitons. As the peak power is increased to 110 W, the characteristic MI spectral sidebands around the pump wavelength are observed. The asymmetry in the spectral power density of the short and long wavelength regions arises due to the different continuum generation mechanisms responsible for each side. The long wavelength side of the spectrum experiences additional gain due to stimulated Raman scattering, which, transfers power from shorter to longer wavelengths. On the other hand, wavelengths below the pump are generated primarily by phase matched FWM [8,11]. The smooth nature of the continuum can be attributed to the ensemble average of spectra produced by multiple solitons within the 2ns pulse envelope [12].

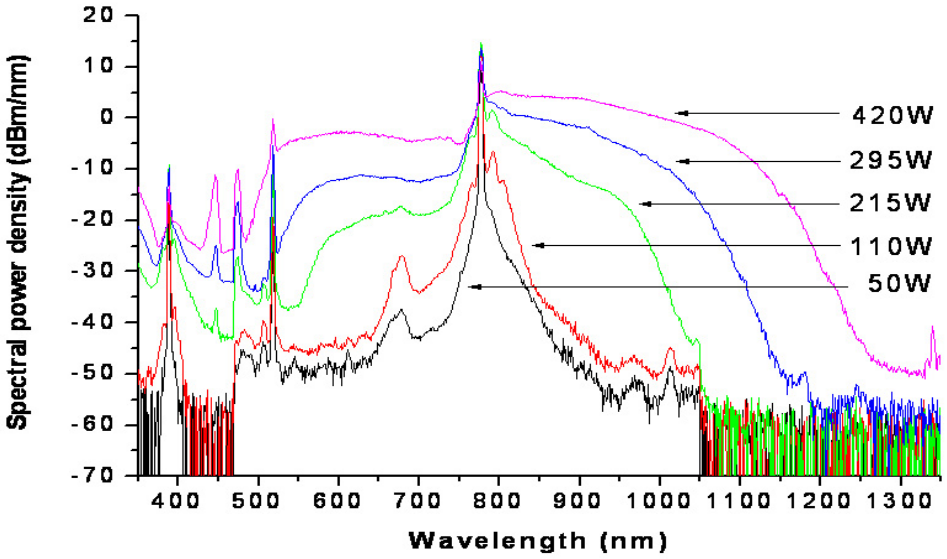

Fig. 2.5. SC spectral evolution as a function of input peak power

Finally, the scalability of the SC average output power was demonstrated. The nonlinear phenomena responsible for SC generation are dependent on the length of the PCF and the peak power of the 776.5 nm pulses. The average power in the continuum was scaled up by increasing the repetition rate of the seed laser diode while adding more pump power (at 976 nm) to keep the peak power (and hence, the spectral shape) constant around 1kW [13]. Figure 2.6 shows the linear increase in SC average power from 250 mW to 740 mW with an increase in repetition rate from 300 kHz to 1 MHz. The average power could be further increased by using a larger core gain fiber (to reduce amplifier non-linearity) and increasing the pumping power by additional 976 nm pump diodes.

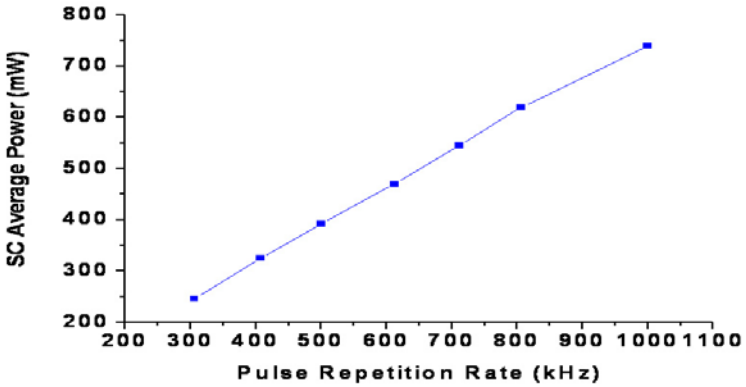

Fig. 2.6. SC average output power versus pulse repetition rate

2.4 Numerical simulations

To determine the wavelength limits of the generated SC and identify the generation mechanisms, numerical simulations of the generalized non-linear Schrodinger equation were performed using the adaptive split-step Fourier method. The complex envelope $A(z,\tau)$ of a pulse, under the slowly varying approximation satisfies the generalized NLSE given by,

$$\frac{\partial A}{\partial z} = (\hat{D} + \hat{N})A$$

$$\hat{D} = -\frac{i}{2}\beta_2 \frac{\partial^2 A}{\partial \tau^2} + \frac{1}{6}\beta_3 \frac{\partial^3 A}{\partial \tau^3} + \frac{i}{24}\beta_4 \frac{\partial^4 A}{\partial \tau^4} - \frac{\alpha}{2}$$

$$\hat{N} = i\gamma(1 + \frac{i}{\omega_0}\frac{\partial}{\partial t})\int_{-\infty}^{+\infty}[(1 - f_R)\delta(t) + f_R h_R(t)]\,|A(z, t-t')|^2\, dt'$$

where the pulse moves along z in the retarded time frame $\tau = t - z/v_g$ with the center angular frequency of ω_0. The linear terms in the differential operator $\hat{D}$ account for the second (β_2), third (β_3) and the fourth order (β_4) dispersion as well as the loss (α) of the fiber. The terms in the operator $\hat{N}$ result from nonlinear interactions, which describe self-phase modulation, self-steepening and stimulated Raman scattering effects. In particular, the effective nonlinearity is defined as $\gamma = n_2\omega_0 / cA_{eff}$, where n_2 and A_{eff} are the nonlinear refractive index and effective mode area of the fiber respectively. In addition, $h_R(t)$ represents the Raman response function, and f_R is the fractional contribution of the Raman response to the nonlinear polarization. To reduce computation time, a 20 ps super-Gaussian pulse at 776.5 nm was fed as the input to our simulator. Simulations with broader pulse widths (up to 200 ps) were also performed and showed no significant difference in the spectrum obtained.

Figure 2.7 shows comparison between experiment and simulation results for 1.5 m of PCF with $\gamma = 65\ W^{-1}km^{-1}$. The pump wavelength is 776.5 nm and the peak power is 420 W. The differences between the 2 curves can be explained as follows. On the short wavelength side, the experimental spectrum shows additional peaks between 350-550 nm that are not present in the simulation. As mentioned earlier in section 2.3, the peak at 518 nm is due to third harmonic generation from the PPLN crystal, while that at 388 nm is due to four wave mixing between the 518 nm and 777 nm signals. The additional peaks at 440 nm and 475 nm are also attributed to the same phase matched process. Since the simulator only assumes a delta function input at the second harmonic frequency of 776.5 nm, and does not include the weak third harmonic at 518 nm, the various phase matched peaks due to the four wave mixing process are not present in the simulated spectrum. On the long wavelength side, simulation results show higher power than the experimentally obtained spectrum. While the simulator assumes a constant mode field diameter (MFD) across the entire wavelength range, the MFD actually increases for long wavelengths as the guiding properties of the fiber become weaker. Thus, the effective non-linearity at long wavelengths is smaller in the experiment compared to the simulations, resulting in a lower continuum level.

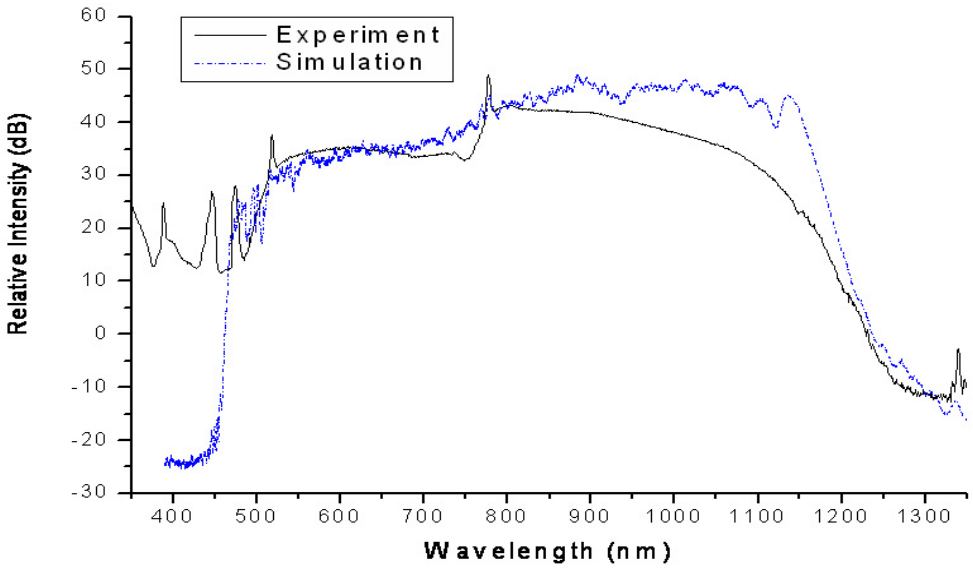

Fig. 2.7. Comparison of experimental and simulation spectra for 1.5m PCF at 420W peak power

To confirm that the SC generation is initiated by MI, simulations with fibers having different zero dispersion wavelengths but the same dispersion slope 0.85 ps.nm^{-2}km^{-1} were performed. In each case, the common parameters were the pump wavelength λ_p = 776.5 nm, peak power P = 420 W and non-linear coefficient γ = 65 W^{-1}km^{-1}. Figure 2.8(a) shows the output spectrum after propagation through 0.3 m of fibers with λ_0 ranging from 745 nm to 775 nm. We observe symmetrical side bands around the pump wavelength and obtain maximum broadening for the fiber with λ_0=775 nm. This is consistent with MI, since MI phase matches only when the pump is in the anomalous dispersion region and the gain bandwidth is inversely proportional to the separation of the pump wavelength from the fiber λ_0. The theoretical MI gain coefficient is given by,

$$g = \sqrt{(\gamma P)^2 - \left[\left(\frac{\Delta k}{2}\right) + \gamma P\right]^2}\ ,\ \Delta k = -\frac{\lambda^2}{2\pi c}\left[\left.\frac{dD}{d\lambda}\right|_{\lambda_0}\left(\lambda_p - \lambda_0\right)\right]\left(\omega_p - \omega_s\right)^2$$

After propagation through a length L of the fiber, the power gain experienced by the Stokes signal is given by, $G = \frac{P_s(L)}{P_{s0}} = 1 + (\gamma P L)^2 \frac{\sinh^2(gL)}{(gL)^2}$. Figure 2.8(b) plots G after L = 0.3 m for fibers with different λ_0 and the results are in excellent agreement with Fig. 2.8(a). This confirms that modulation instability is the dominant non-linear effect in the initial propagation through the PCF. Initially, anomalous dispersion plays an important role in breaking up the quasi-CW pulse into ultra short pulses required for SC generation. Thus, while MI seeds the SC generation process, MI alone cannot account for the final continuum bandwidth obtained. The resulting ultra short pulses further broaden the spectrum as they propagate down the fiber through an interplay of self phase modulation, stimulated Raman scattering and phase matched four wave mixing. But, as the continuum evolves towards the blue wavelength region, the large normal dispersion of the PCF prevents efficient four wave mixing. In other words, the short wavelength edge of the continuum is limited by phase mismatch caused by the fiber dispersion.

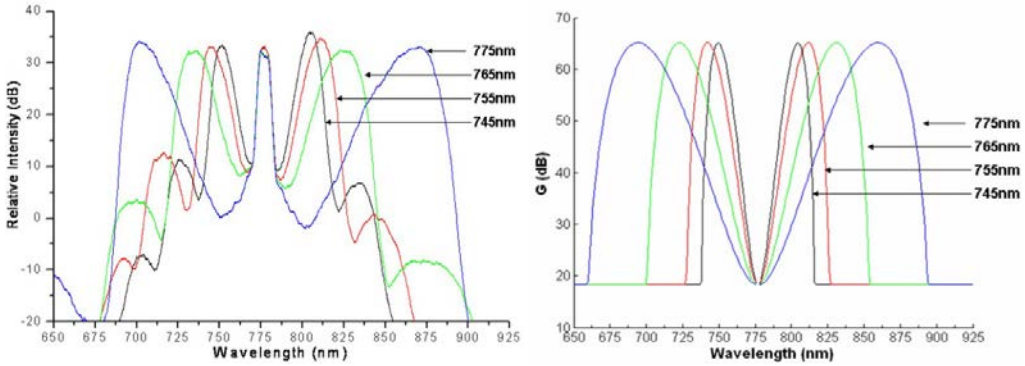

Fig. 2.8. Output after 0.3m PCF for different λ_0 (a) Simulation output (b) Theoretical MI power gain

2.5 Discussion

In this section, a 2 stage model based on separation of the pulse break-up and spectral broadening stage is proposed to optimize the short wavelength SC generation process. In the first stage, a short length of PCF is pumped in the anomalous dispersion regime to break-up the nanosecond pulse into a train of ultra short femtosecond pulses through MI. In the second stage, a material with high Kerr non-linearity (large non linear refractive index n_2) and minimal dispersion is used to maximize spectral broadening. Simulation results for the 2 stage model are presented below. Figure 2.9 shows the temporal output after propagating through 0.5 m of PCF with λ_0 = 745 nm and λ_p = 776.5 nm. The initial 20 ps super-Gaussian pulse is broken up into ~20 fs wide pulses with ~3x the original intensity. The separation between pulses is ~74 fs and is in excellent agreement with the theoretical separation given by $T = 2\pi / \sqrt{2\gamma P_0 / |\beta_2|}$ = 73 fs, where P_0 = 420 W, γ = 65 $W^{-1}km^{-1}$ and β_2 = -7.39e-3 ps^2/m.

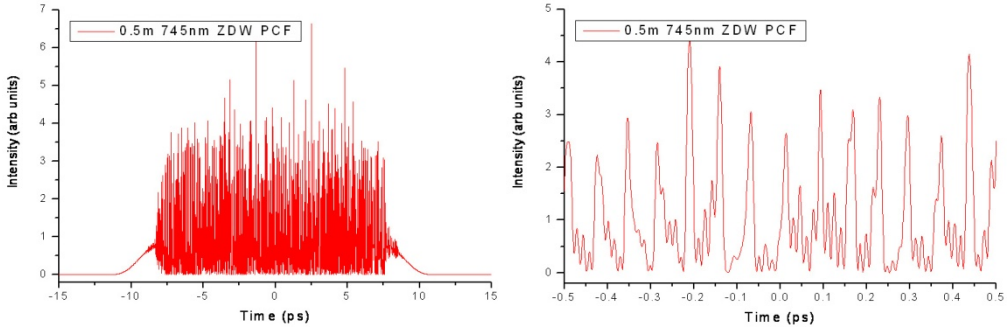

Fig. 2.9. MI induced pulse break-up after propagation through 0.5m PCF with λ_0=745nm and 420W input peak power

The narrow pulses from the 1st stage PCF are then launched into an ideal 2nd stage dispersion less material with non-linearity comparable to the PCF. The output spectra for different lengths of the 2nd stage material are shown in Fig. 2.10. We observe symmetric and smooth broadening around the pump wavelength indicative of SPM as the primary broadening mechanism. On the other hand, Fig. 2.11 shows the results for the same propagation length in a single stage PCF. The corresponding spectra are asymmetric and much narrower as further spectral broadening is ultimately limited by fiber dispersion. The 20 dB SC bandwidth after just 4 cm of stage 2 material is ~425 nm compared to ~230 nm for the single stage, an enhancement of almost 2x.

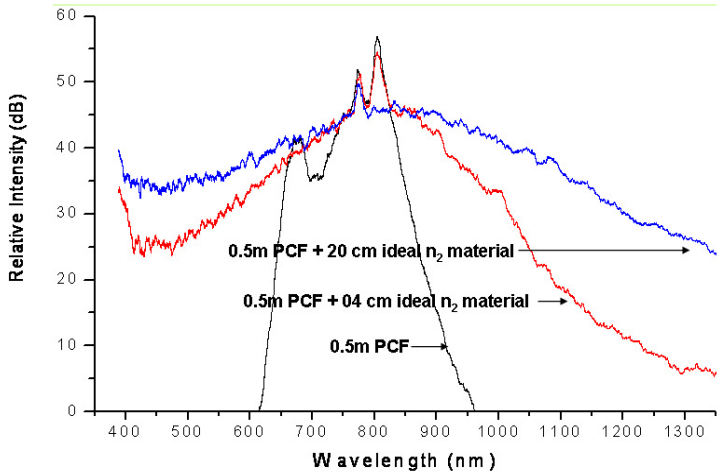

Fig. 2.10. Spectra from two stage model: 0.5m 745 nm λ_0 PCF followed by ideal n_2 material

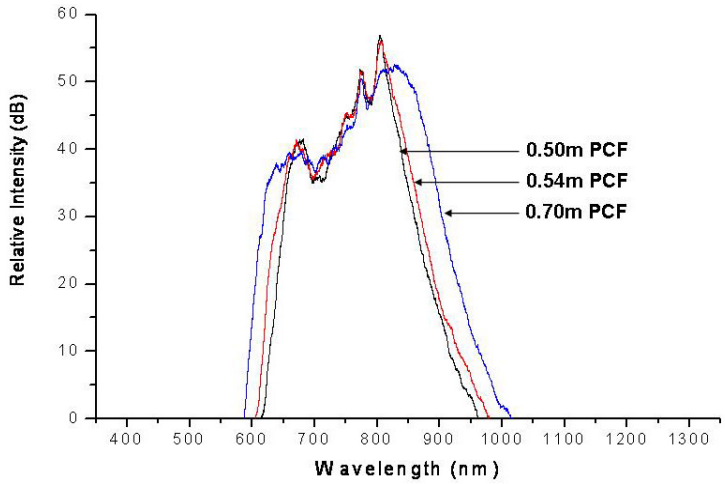

Fig. 2.11. Spectra from single stage model: 0.50-0.70m of 745 nm λ_0 PCF

The choice of the 2nd stage material is based on the relative values of the dispersion length (L_D) and non-linear length (L_{NL}). The dispersion length is given by $L_D = \tau_0^2 / |\beta_2|$ and the nonlinear length is $L_{NL} = 1/(\gamma P)$, where τ_0 is the FWHM of the soliton from the 1st stage and P is the peak power. While it is essential for the 1st stage PCF to be pumped in the anomalous regime, the 2nd stage can be normally dispersive provided $L_{NL} << L_D$. This ensures that significant SPM broadening takes place before the pulses are reduced in intensity due to the normal dispersion. As an example, PCF filled with liquid carbon disulfide [14] not only exhibits large non-linearity ~ $6W^{-1}m^{-1}$ at 775 nm, but can also be tailored to minimize dispersion at the pump wavelength.

2.6 Summary

In summary, SC extending from 450-1200 nm with 0.74 W average power was generated in PCF using frequency doubled light from a dual stage fiber amplifier. The average SC power was shown to be linearly scalable with the pulse repetition rate while the maximum output power was limited by the core size of the gain fiber and available pump power. Numerical simulations confirmed that the broadest SC spectrum required pumping in the anomalous dispersion regime close to the PCF λ_0. Further enhancement of the continuum bandwidth is possible through a two step SC generation process – MI induced pulse breakup in a short length of anomalous dispersion PCF followed by SPM broadening in an ideal dispersion less high non-linearity material.

References

1. J. M. Dudley, G. Genty, and S. Coen, “Supercontinuum generation in photonic crystal fiber,” Rev. Mod. Phys. **78**, 1135-1184(2006)
2. A. Rulkov, M. Vyatkin, S. Popov, J. Taylor, and V. Gapontsev, "High brightness picosecond all-fiber generation in 525-1800nm range with picosecond Yb pumping," Opt. Express **13**, 377-381 (2005)
3. T. Schreiber, J. Limpert, H. Zellmer, A. Tunnermann, and K. Hansen, "High average power supercontinuum generation in photonic crystal fibers", Opt. Comm. **228**, 71-78 (2003)
4. J. M. Stone and J. C. Knight, "Visibly “white” light generation in uniform photonic crystal fiber using a microchip laser," Opt. Express **16**, 2670-2675 (2008)
5. A. Kudlinski, A. K. George, J. C. Knight, J. C. Travers, A. B. Rulkov, S. V. Popov, and J. R. Taylor, "Zero-dispersion wavelength decreasing photonic crystal fibers for ultraviolet-extended supercontinuum generation," Opt. Express **14**, 5715-5722 (2006)
6. P. A. Champert, V. Couderc, P. Leproux, S. Février, V. Tombelaine, L. Labonté, P. Roy, C. Froehly, and P. Nérin, "White-light supercontinuum generation in normally dispersive optical fiber using original multi-wavelength pumping system," Opt. Express **12**, 4366-4371 (2004)
7. C. Xiong, A. Witkowska, S. G. Leon-Saval, T. A. Birks, and W. J. Wadsworth, "Enhanced visible continuum generation from a microchip 1064nm laser," Opt. Express **14**, 6188-6193 (2006)
8. W. Wadsworth, N. Joly, J. Knight, T. Birks, F. Biancalana, and P. Russell, "Supercontinuum and four-wave mixing with Q-switched pulses in endlessly single-mode photonic crystal fibres," Opt. Express **12**, 299-309 (2004)
9. C. J. S. de Matos, R. E. Kennedy, S. V. Popov, and J. R. Taylor, "20-kW peak power all-fiber 1.57-μm source based on compression in air-core photonic bandgap fiber, its frequency doubling, and broadband generation from 430 to 1450 nm," Opt. Lett. **30**, 436-438 (2005)
10. C. Xia, M. Kumar, O. P. Kulkarni, M. N. Islam, F. L. Terry, Jr., M. J. Freeman, M. Poulain, and G. Mazé, "Mid-infrared supercontinuum generation to 4.5 μm in ZBLAN fluoride fibers by nanosecond diode pumping," Opt. Lett. **31**, 2553-2555 (2006)
11. S. Coen, A. H. L. Chau, R. Leonhardt, J. D. Harvey, J. C. Knight, W. J. Wadsworth, and P. S. J. Russell, "Supercontinuum generation by stimulated Raman scattering and parametric four-wave mixing in photonic crystal fibers," J. Opt. Soc. Am. B **19**, 753-764 (2002)
12. C. Xia, M. Kumar, M.Y. Cheng, O.P. Kulkarni, M.N. Islam, M.N, A. Galvanauskas, F.L. Terry, M.J. Freeman, D.A. Nolan, W.A. Wood, "Supercontinuum Generation in Silica Fibers by Amplified Nanosecond Laser Diode Pulses," IEEE J. Sel. Top. Quantum Electron vol.**13**, no.3, 789-797 (2007)

13. C. Xia, M. Kumar, M. -Y. Cheng, R. S. Hegde, M. N. Islam, A. Galvanauskas, H. G. Winful, F. L. Terry, Jr., M. J. Freeman, M. Poulain, and G. Mazé, "Power scalable mid-infrared supercontinuum generation in ZBLAN fluoride fibers with up to 1.3 watts time-averaged power," Opt. Express **15**, 865-871 (2007)
14. R. Zhang, J. Teipel, and H. Giessen, "Theoretical design of a liquid-core photonic crystal fiber for supercontinuum generation," Opt. Express **14**, 6800-6812 (2006)

Chapter 3

High resolution line-scan 3D imaging system for solder ball inspection

3.1 Introduction

The continuous reduction in size of semiconductor devices has led to an increased density of chips on a wafer. Consequently, conventional wire leads that extend outside the chip's physical dimensions are being replaced by solder ball grid arrays (Fig. 3.1) that can directly be flip-chip bonded with an external circuit. The reliability of electrical contact depends on the shape and size of solder balls deposited on the chip, and, thus, inspection of the balls is very important for quality control [1]. Current 2D inspection techniques using machine vision can measure ball diameter and location, but provide no information regarding the height of different balls. 3D methods such as laser triangulation and confocal microscopy have been used to measure the ball height, but they do not provide any shape information [1]. Ohta et.al. [2,3] demonstrated 3D measurement of tilted and curved surfaces with ~1 m stand-off distance and 1.5 μm axial resolution using an all-fiber integrated point-scan interferometer operating at 1.55 μm. In comparison, the SC based line scan technique demonstrated in this chapter enables determination of top shape of the ball by measuring the 3D profile over a +/-20 degree angle from the vertical axis of the ball with 125 nm axial resolution. Thus, this method enables the measurement of individual ball heights along with the ability to detect defective ball shapes.

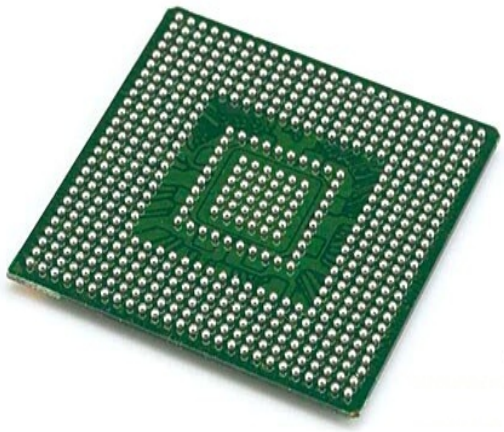

Fig. 3.1. Solder ball grid array

The key results obtained in this chapter are described below. We demonstrate a line scan system with 125 nm axial (z) and 15 μm lateral (x-y) resolution for 3D inspection of curved surfaces. The system comprises of the visible super-continuum (SC) laser described in chapter 2 coupled to a Fourier domain Michelson interferometer via cylindrical optics. While the broad bandwidth (600-700 nm) of the SC source is responsible for the high axial resolution [4], the high laser average output power (~5 mW) enables the measurement of curved surfaces that reflect most light in a direction away from the receiver. The maximum measurable angular tilt from the sample surface normal for a given source power is observed to depend on the surface roughness of the sample. As an example, the line scan system is used to demonstrate height measurement over +/- 20 degrees from the normal on a solder ball grid array (BGA) used in the semiconductor industry and over +/- 60 degrees on a rough steel ball bearing sample.

The different sections in the chapter are organized as follows. The optical layout of the line scan interferometer and the algorithm for extracting sample height is described section 3.2. In section 3.3, calibrated samples are used to measure the system's axial and transverse resolution, axial measurement range, sensitivity and angular measurement capability in order to determine the performance metrics of the system. Section 3.4 describes the measurements performed on a ball grid array sample to determine individual ball heights and detect different types of shape defects. Finally, the limitations

of the system and scope for improvement are discussed in section 3.5 before summarizing the results in section 3.6.

3.2 Experimental setup

3.2.1 Fourier domain line scan interferometer

Figure 3.2 illustrates the optical layout for the line scan interferometer. While the setup resembles a conventional point-scan FD-OCT system, the introduction of a cylindrical lens and replacement of a 1D array with a 2D CCD camera enables the measurement along an entire line instead of a single point with each camera image [5]. The interferometer layout was modeled using ZEMAX software to provide the best imaging performance using standard off-the-shelf optics. While the total SC spectrum extends from 500 – 1200 nm, the line scan interferometer design only utilizes 100 nm of the SC spectrum from 600 – 700 nm to minimize the effects of chromatic aberration caused by the cylindrical lens.

First, the light from the supercontinuum source was collimated to an 8 mm diameter beam using a 10X microscope objective. Using a 600 nm long pass and 700 nm short pass filter, the average power in the above spectral region was measured to be ~5 mW. The collimated beam then passes through a 100 mm focal length plano-convex cylindrical lens CL1 followed by an equal focal length spherical achromatic doublet L1 separated from CL1 by 200 mm. This imaging geometry transforms the 8 mm circular beam at the input of CL1 to an 8 mm long (y-axis) by 15 μm wide (x-axis) line at the focal plane of lens L1. The positioning of the non-polarizing cube beam splitter just after lens L1 ensures that an identical focused line is generated in both the sample and reference arms. After reflection from the sample and reference mirror M2, the object and reference beams are re-combined at the beam splitter and produce an interference pattern. Variable neutral density filters ND1 and ND2 are used to adjust the balance between the light intensities in the two arms of the interferometer. In order to extract the sample

height information from the interference pattern, it must be spectrally dispersed and imaged onto a camera.

The interferogram is spectrally dispersed along the x-axis by passing the light through a 600 groves/mm transmission diffraction grating while achromatic doublet lenses L2 and L3 (both with 100 mm focal length) are used to image the wavelength resolved interferogram onto a 2048 x 2048 pixel CCD camera. Since L2 and L3 are identical lenses, the 8 mm long line on the sample is imaged 1:1 along the camera's y-axis. Thus, while the CCD rows contain spatial information along the line (y-axis), the spectral information is contained along the CCD columns. Hence, a single image frame of the CCD provides height information along the entire line [6,7] and a complete 3D scan of the sample only requires a 1D translation of the sample along the x-axis.

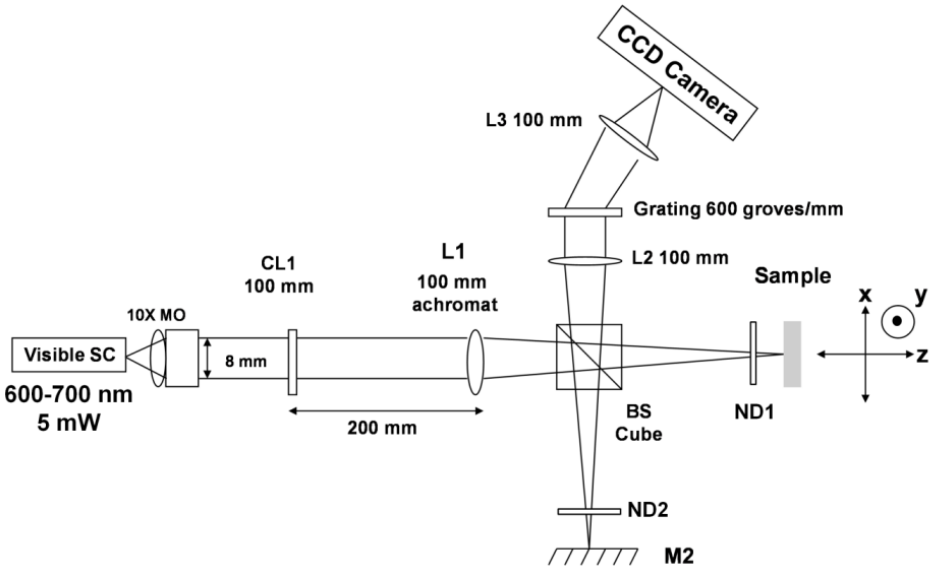

Fig. 3.2. Experimental setup for visible SC based Fourier domain line scan interferometer

3.2.2 Extraction of sample height from CCD images

The extraction of meaningful sample height data along the imaged line requires post-processing of the images acquired by the CCD camera. A 4 step algorithm was used to perform the required image processing analysis in Matlab. The detected spectrum as a function of frequency in each CCD row is given by [8]-

$$S_{out}(\omega) = |E_R(\omega)|^2 + |E_S(\omega)|^2 + 2\,\mathrm{Re}\{E_R(\omega)^* E_S(\omega)\} \qquad (1)$$

The above equation represents the total intensity from three terms – only reference arm power, only sample arm power and interference between the sample and reference arms. However, the useful information about sample height information is only contained within the third interference term and the axial scan is obtained by taking the Fourier transform of this term. Thus, the first step in the algorithm is to remove the dominant DC term by performing a background image subtraction. This is accomplished by blocking the light in the sample arm and capturing an image with the light reflected from just the reference arm. This background image is then subtracted from each image before proceeding to the next step. In the 2nd step, a sub-frame is selected from the entire 2048 x 2048 pixels image frame to define the spatial extent of the imaged line and the spectral range of the continuum to be used for processing. In our experiments, each row pixel corresponds to 7.4 μm of the line length while each column pixel represents a spectral bandwidth of 0.116 nm. We used 768 rows corresponding to the central 5.7 mm section of the 8 mm long line and 860 columns corresponding to the 100 nm wavelength range from 600–700 nm.

The Fourier transform (FT) process requires equally sampled points in the frequency space while the light from the grating is spread across the CCD columns in equal wavelength increments. Thus, in step 3, the wavelength interferogram along each row is converted to a frequency interferogram and then re-sampled using a cubic-spline interpolation algorithm [9,10] to generate 1024 equally spaced points in the frequency domain. In the final step, the result is Fourier transformed to the z-space using a 32,768 point fast Fourier transform algorithm.

Since the samples used in this experiment were not multi layered biological tissues but instead metallic, the analysis was simplified by assuming that all reflections originate from a single layer at the top of the sample surface. Under this assumption, the z position of the peak of the FT curve is assigned as the distance of the corresponding point on the

sample from the interferometer zero delay position. Repeating this procedure for each row of the image produces a height profile of the sample along the imaged line (y-axis). By processing multiple images corresponding to different sample positions along the x-axis, one can build up a complete 3D map of the surface. An important precaution to take while performing this experiment was to always place the sample entirely on one side of the zero delay position. A sample surface that straddles the zero delay position would have ambiguous height measurements since the FD technique only measures the magnitude of the sample distance and not the sign. Figure 3.3 summarizes the procedure to obtain the height profile along the imaged line from the CCD image.

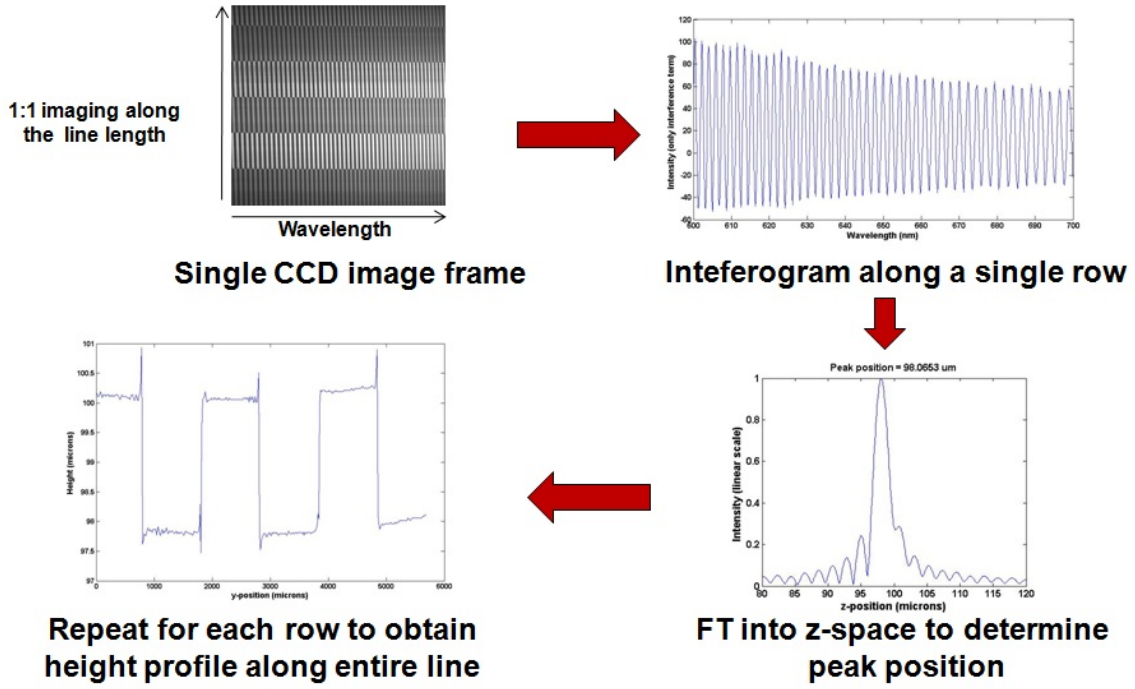

Fig. 3.3. Conversion from single CCD image to height profile along imaged line

3.3 System calibration

3.3.1 Transverse and axial resolution

In this section, the system resolution along each linear axis is obtained. Along the x-axis, the resolution is defined as the $1/e^2$ width of the line shaped focus at the sample surface. This value was determined to be ~15 μm using a razor edge scan to sample the beam profile. The resolution along the y-axis is determined by the imaging geometry of the

interferometer design. Since lenses L2 and L3 in Fig. 3.2 have an equal focal length of 100 mm, the 8 mm long line on the sample surface is imaged with a magnification ratio of 1:1 along the CCD's y-axis. Thus, the y-resolution of the system is now simply defined as being equal to the camera pixel size of 7.4 μm.

The z (axial) resolution of the system is related to coherence length of the light source used, which in turn depends on the optical bandwidth. The theoretical value of the coherence length for a light source with a Gaussian spectrum is given by [3]-

$$l_{coh} = (2\ln 2/\pi) * \lambda_0^{\,2} / \Delta\lambda \approx 0.44\,\lambda_0^{\,2} / \Delta\lambda \qquad (2)$$

where λ_0 is the center wavelength and $\Delta\lambda$ is the full width at half maximum of the source spectrum. However, for a light source with a rectangular spectrum such as the visible SC, the multiplicative factor in eq. (2) ~ 0.60. In our system, we have λ_0 = 650 nm and $\Delta\lambda$ = 100 nm which gives l_{coh} ~ 2.54 μm. The coherence length of the SC source was also determined experimentally by placing a flat silver mirror in the sample arm at a distance of 50 μm from the zero delay position and obtaining the z-profile (Fig. 3.4) at the center of the line. The experimentally measured coherence length is defined as the FWHM of the peak and was determined to be ~2.50 μm which is in good agreement with the theoretical value.

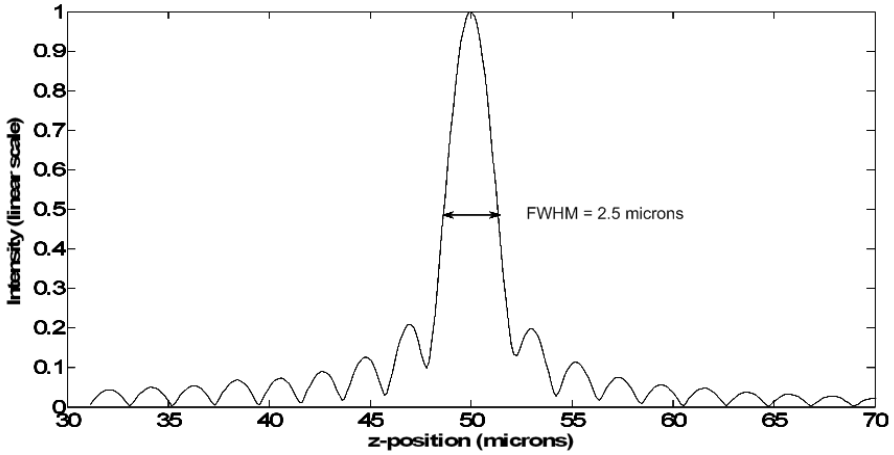

Fig. 3.4. Experimental determination of coherence length

The relationship between the axial (z) resolution and coherence length depends on the nature of the sample under test. For a tissue sample in an OCT setup, the two values are defined as being equal due to the multiple reflections from different layers. However, unlike OCT, we are not trying to determine the layers within the sample but instead determine the 3D shape of the sample surface. Under the assumption of a metallic sample as described in Sec 3.2.2, the location of the peak of the curve can be super-resolved to much better than the nominal 3 dB width [3]. In our system, we achieved a factor of 20 improvement and thus define the axial resolution to be $1/20^{th}$ of the measured coherence length i.e. 125 nm.

Finally, the estimate of the system's axial resolution was verified by measuring a calibrated silicon step height standard coated with reflective aluminum. Figure 3.5 shows a 3D view of the 1mm x 1mm sample as measured with the line scan interferometer. The step in the middle is clearly resolved and the step height was measured to be 125.2 nm +/- 17.7 nm. The error bar was obtained by determining the standard deviation of the heights in each individual plane of the step and calculating the square root of the sum of their squares to estimate the standard deviation of the step height measurement. The experimentally observed value was in close agreement with the 131.0 nm measured by a calibrated Dektak stylus profilometer.

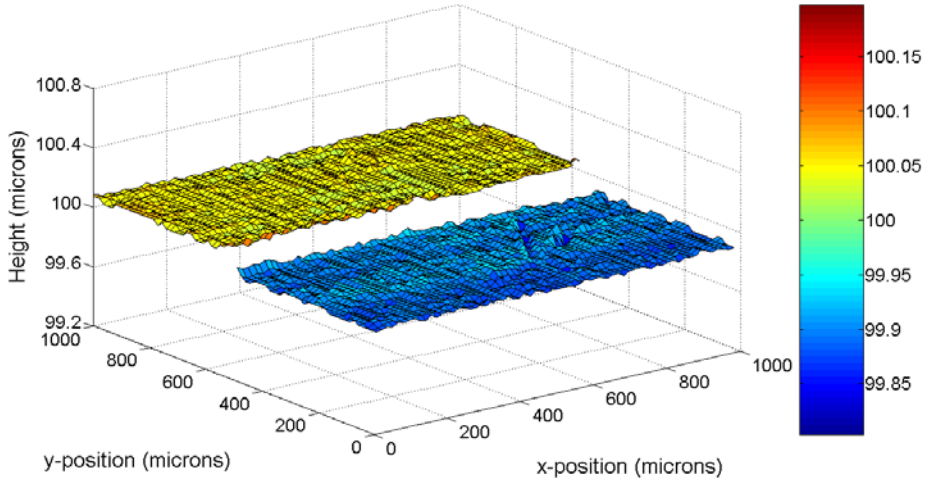

Fig. 3.5. 3D view of calibration step height standard measured by the line scan system

3.3.2 Sensitivity

The sensitivity of the system is a measure of the smallest reflectivity of the sample arm that produces a minimum detectable SNR = 1. The theoretical expression for shot noise limited sensitivity in the Fourier domain configuration is given by [12],

$$SNR_{FD} = \eta P_{sample} \tau_i / h\nu \qquad (3)$$

where P_{sample} is the sample arm power returning to the detection arm, η is the efficiency of the spectrometer system, τ_i is the camera integration time, h is the Planck's constant and ν is the center frequency of the light. While the above equation was obtained for a point-scan system, it is still valid for our line scan system provided we redefine P_{sample} as the sample arm power returning to the detection arm towards each individual CCD row and not the entire camera. With an ideal reflector in the sample arm, 0.5 mW average power was measured returning to the detection arm and imaged across ~1000 CCD rows resulting in $P_{sample} \sim 0.5$ μW. The spectrometer efficiency η was determined to be 0.20, the integration time was set to 100 μs and the center wavelength was 650 nm. Thus, the theoretically expected sensitivity is $SNR_{FD} = 75.1$ dB.

The sensitivity of the system was also determined experimentally by using a weak reflector in the sample arm. A 99% reflectivity mirror was placed in the sample arm with a 10 dB neutral density filter in front of it to provide a total of 20 dB attenuation to the light in the sample arm. The mirror was placed at varying distances from the interferometer zero delay position and the height along the line was measured for each position using the technique described in section 3.2.2. Figure 3.6 shows the obtained FT z-space curves at the center of the imaged line for the different positions of the sample arm mirror.

The system sensitivity at a given position of the sample was calculated by adding the SNR of the corresponding curve (20 times the log ratio of the peak to the standard deviation of the noise floor) to the known attenuation of the sample arm [13]. At z = 100 μm, the SNR is measured as 50.4 dB, resulting in a system sensitivity of 70.4 dB. The

deviation of 4.7 dB from the theoretically expected value is attributed largely to the excess relative intensity noise in the SC source above the shot-noise limit. In addition, numerical sampling errors and mechanical vibrations in the interferometer setup also contribute to the degraded system sensitivity.

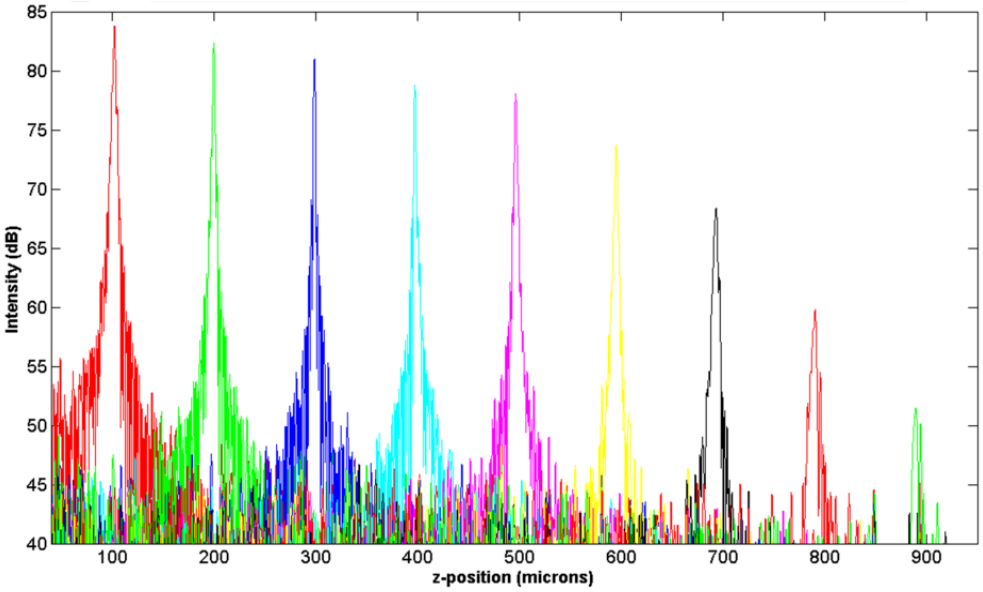

Fig. 3.6. Sample depth dependent decrease in system sensitivity

3.3.3 Axial measurement range

The axial measurement range in a Fourier domain system is limited by the finite spectrometer resolution. The axial position of the sample is encoded as a function of the periodicity of the interference fringes. The wavelength separation between adjacent fringe maxima decreases as the sample distance from the zero delay position increases. The maximum measurable range is reached when the fringe period becomes less than 2 pixels wide. The theoretical maximum measurement range for an FD-OCT system is given by [6]

$$z_{\max} = \lambda_0^{\,2} / 4\delta\lambda \qquad (4)$$

where $\delta\lambda$ is the spectrometer resolution. In our system, the 100 nm wide spectrum centered at 650 nm is spread across 860 horizontal pixels (columns) to give $\delta\lambda$ = 0.116 nm. This gives a maximum measurement range z_{max} = 910 μm and is consistent with the

experimentally obtained data shown in Fig. 3.4. A characteristic depth dependant decrease in system sensitivity was observed due to increase in sampling errors at longer delays attributed to finite spectrometer resolution [12]. At the far end of the measurement range near z = 900 um, the sensitivity was almost 32 dB lower than the maximum obtained near the zero delay position.

3.3.4 Angular measurement range

The angular measurement range of the line scan system depends on a combination of source power, camera exposure time and sample surface finish. Two chrome steel ball bearing samples of identical size (3.17 mm diameter) but different surface finish were used to determine the system's angular measurement capability. Sample #1 was left in its original high reflectivity polished state while sample #2 was roughened using a 240-grit sandpaper to provide enhanced diffused scatter. The ball bearing samples were scanned along the x-axis in 15 μm increments and the resulting CCD images were processed using the algorithm described in Section 3.2.2. Before plotting the results on a color coded height map, an additional step was performed to delete points on the ball with an insufficient SNR to accurately determine the ball height at that point. All points with an SNR < 10 dB in the FT z-space curve were not assigned any color and instead just plotted as a white pixel.

The 3D height maps obtained for the polished and roughened ball bearing samples are shown in Fig. 3.7(a), 3.7(b) and 3.7(c), 3.7(d) respectively. In the case of the polished ball, measurements were only possible over an angular range of +/- 20 degrees from the ball normal. The system was unable to map out the ball bearing surface at steeper angles since the non-specular reflection from the ball surface at these angles was below the sensitivity limit of the system. On the other hand, the line scan system was able to obtain height information over +/- 60 degrees from the roughened sample due to the surface reflectance being more diffuse as opposed to specular. The difference in observable angular range between the two samples is due to the difference in reflectivity fall-off

rates from the normal to off-normal angles. In the polished ball bearing, the reflectivity falls of much more rapidly in non-specular directions compared to the gradual decrease in the roughened ball. Table 3.1 summarizes the performance metrics of the line scan system.

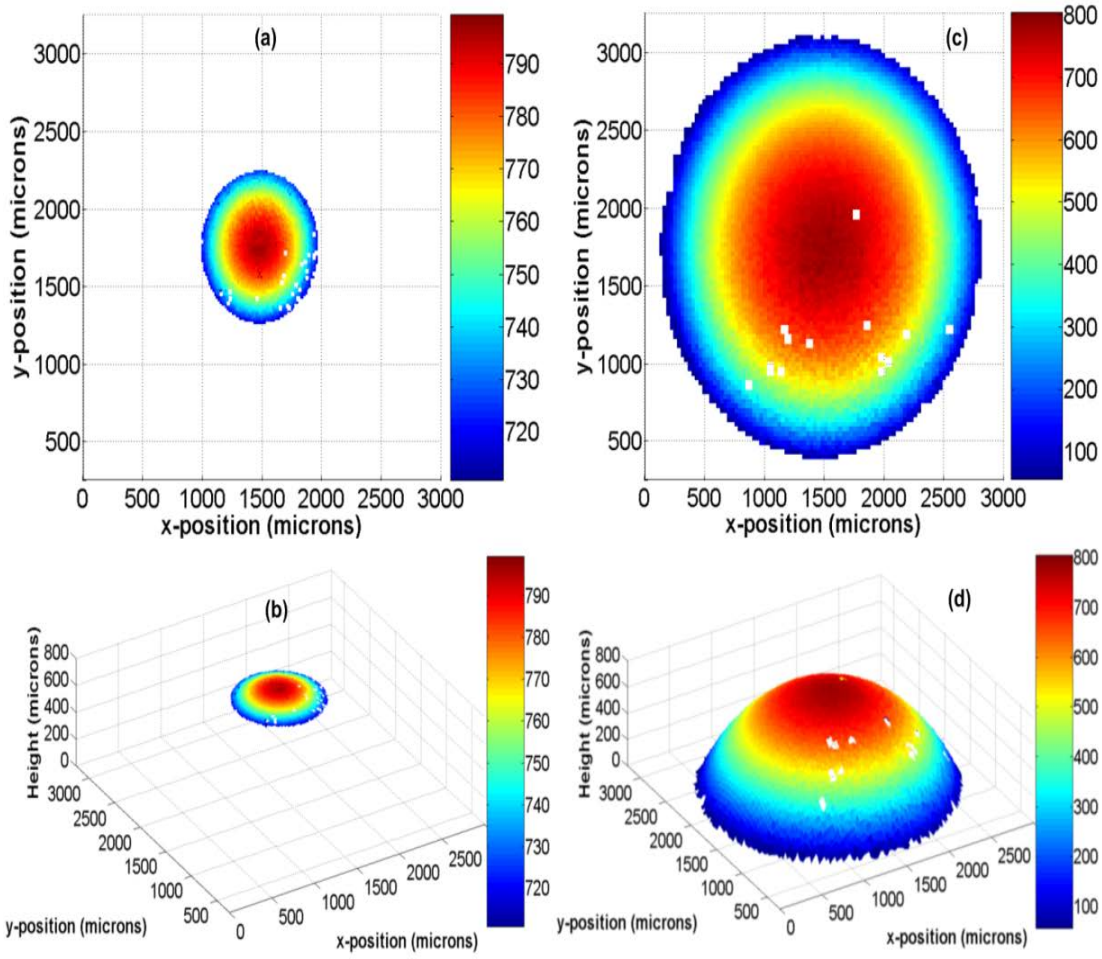

Fig. 3.7. 3D scan of steel ball bearing – (a) Polished ball - top view, (b) Polished ball - side view, (c) Roughened ball - top view, (d) Roughened ball - side view

Parameter	Value
x resolution	15 μm
y resolution	7.4 μm
z resolution	125 nm
Line length	5.7 mm
Axial measurement range	910 μm
Angular measurement range	Depends on surface roughness (between +/-20 to +/-60 degrees)
Sensitivity	70.4 dB

Table 3.1. Performance metrics of line scan system

3.4 Experimental results

3.4.1 Ball grid array surface map

After completing the characterization of the system's performance metrics, a complete 3D scan of a solder ball grid array sample was performed. The sample consists of 75 spherical solder balls on a 4.5 mm x 5 mm silicon die. The solder balls are ~300 μm high and are positioned on a square gird with adjacent ball spacing (center to center) of ~500 μm. The sample was placed on a stepper motor and a Labview program was used to scan the sample along the x-axis in 15 μm increments. The program also controlled a frame grabber card that captured interference images from the CCD camera at a rate of 2 frames/sec resulting in a net linear scan rate of 30 μm/s. The program acquired 300 images (4.5 mm) to cover the entire area of the die and then processed the images in Matlab using the algorithm described in section 3.2.2. Finally, any horizontal and vertical tilt resulting from errors in the initial positioning of the sample was removed in the processed 3D image.

The final obtained image in Fig. 3.8 shows the resulting 3D map of the sample with a leveled substrate and ball tops of different heights and shapes. The color bar shows the height of each pixel as measured from the interferometer zero delay plane. Locations on the sample which did not reflect sufficient light back towards the camera are shown in white as they did not produce a measurable interference pattern to extract a meaningful

height value. While almost all points from the base of the sample could be measured, we could only measure +/- 20 degrees on most ball tops due to the mostly specular reflection from the shiny solder balls.

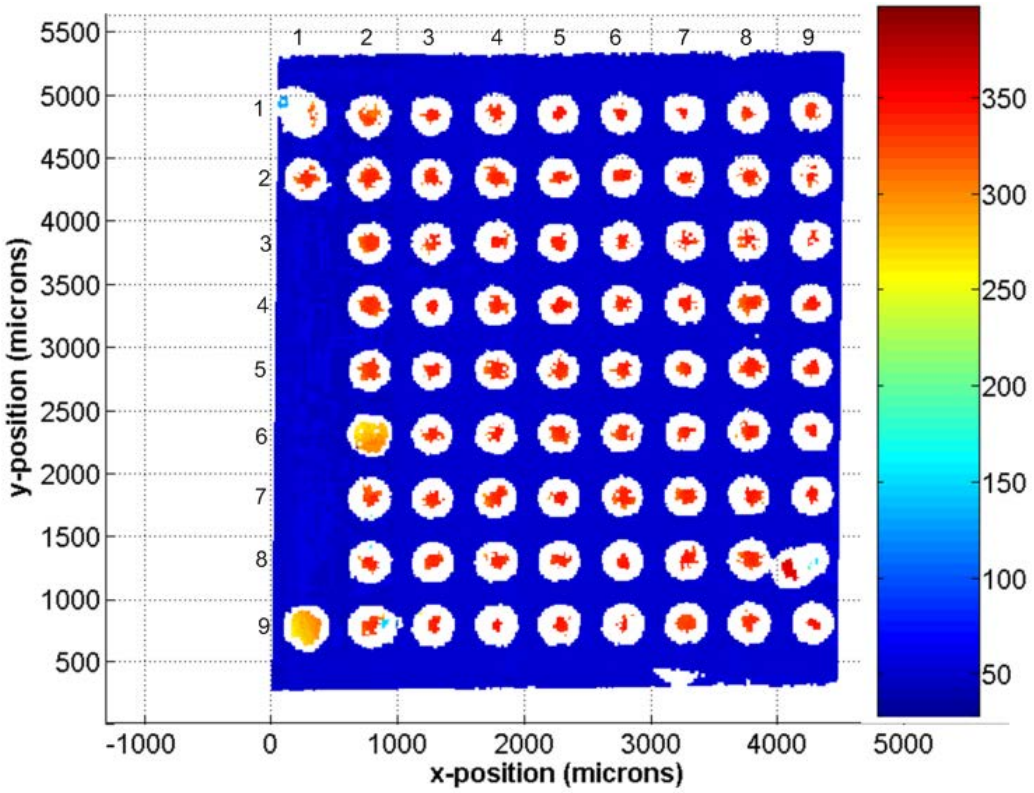

Fig. 3.8. 3D height map (microns) of solder ball grid array

3.4.2 Determination of ball heights and dynamic repeatability

The overall 3D map of the sample needs to be further processed to extract information regarding the height of each ball. The dynamic height repeatability was obtained by removing the BGA sample from the stepper motor stage at the end of each scan and then placing it in the sample holder again before the start of the next scan. Thus, for each independent scan performed in the above manner, vertical and horizontal tilt correction was performed to the height map before determination of ball heights. The height of each ball was defined as the average of the 9 highest pixels on each ball minus the average height of the surrounding flat base.

Table 3.2 below shows the mean height and standard deviation obtained for the 9 balls in column 3 of the die after 10 independent scans of the same region. The overall dynamic repeatability of the height measurements is defined as the worst case standard deviation of ~167 nm. We believe the variations in the values of the standard deviation in the table below arise due to the relatively large pixel size (15 μm x-pixel and 7.4 μm y-pixel) compared to the ball size (~290 μm). Thus, repeated scans of the same ball produce different height results as each scan might sample slightly different regions on the ball due to differences in initial sample positioning. While the repeatability results were adequate for the intended application, further improvements can be made to the repeatability using a better algorithm based on obtaining a best fit sphere for the points.

Ball (Col 3)	Mean Height (μm)	Standard deviation (μm)
1	292.6	0.135
2	291.0	0.065
3	293.6	0.080
4	289.2	0.127
5	284.4	0.071
6	288.6	0.061
7	290.0	0.076
8	289.8	0.122
9	294.9	0.167

Table 3.2. Average solder ball heights and standard deviation over 10 independent scans

3.4.3 Identification of solder ball shape defects

In addition to determining ball height, the line scan system also enables the measurement of the solder ball top shape. While a normal ball has a round top, one can see from Fig. 3.6 that some balls have other shapes. Examples of three of the most common defect types are discussed below. First, we look at the following two balls – Col 1 Row 9 and Col 2 Row 6. Both these balls are shown in orange on the color map indicating a lower

height than most of the other balls which are in red. This defect is known as a flat top and looks like a ball that has been squished from the top. Thus, we get a distinct image with a large number of pixels on the ball with similar height distribution and lower average height than non defective balls.

The second type of defect consists of incomplete spheres such as the balls in Col 1 Row 1 and Col 2 Row 9. One way to indentify these defects is the occurrence of a large number of white pixels (due to absence of reflecting material resulting in low SNR) at the location of the top of the ball. In addition, the presence of two or more clusters of points separated by a discontinuity also indicates the presence of missing solder from the ball shape. Finally, the third type of defect as seen in the ball in Col 9 Row 8 represents a ball that is positioned at the incorrect grid location. This defect can be identified by determining the x-y position of the ball center and comparing its distance to the centers of neighboring balls. Figures 3.9(a), 3.9(b) and 3.9(c) show the line scan 3D view of each type of defect while Figs. 3.10(a), 3.10(b) and 3.10(c) show the corresponding 2D microscope image.

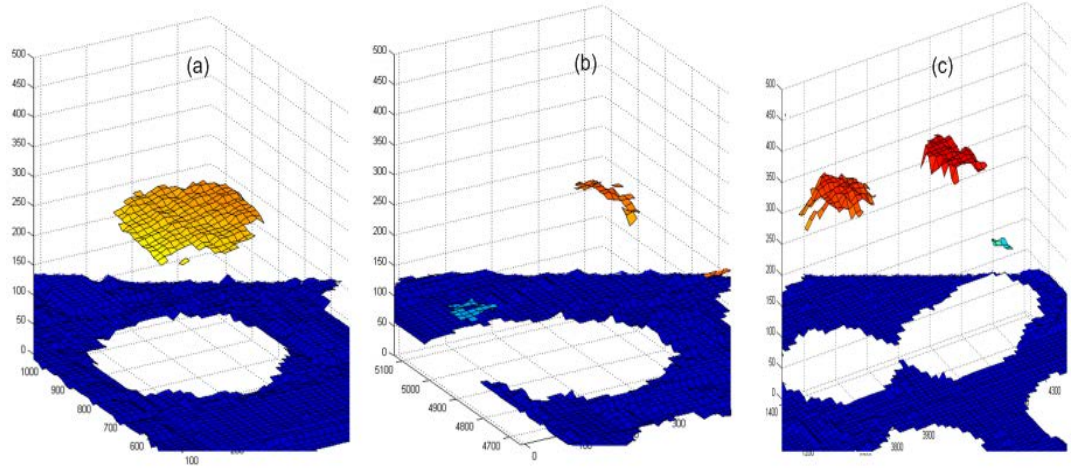

Fig. 3.9. 3D view of solder ball defects –(a) Flat top, (b) Incomplete sphere, (c) Incorrect grid location

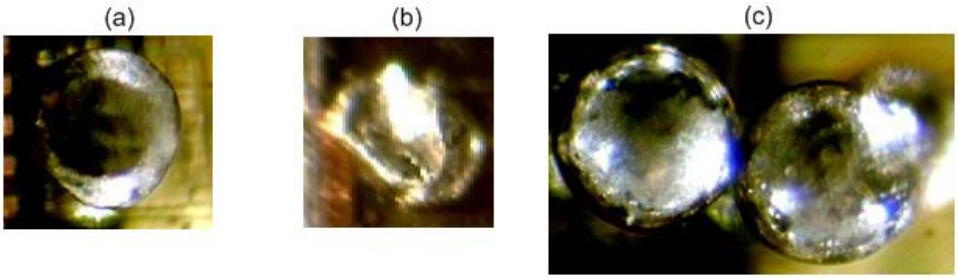

Fig. 3.10. 2D microscope view of solder ball defects – (a) Flat top, (b) Incomplete sphere, (c) Incorrect grid location

3.4.4 Measurement of other samples – copper penny and screw head

In addition to the primary ball grid array sample, the line scan system was also used for the 3D measurement of other flat and curved samples described below. Figure 3.11 shows the height map of an 8 mm x 3.5 mm section of Lincoln's face on a copper penny with the raised features such as the noise and hair clearly visible. Figure 3.12 shows the 3D view of a size 4-20 screw head with a clearly distinguishable ridge pattern.

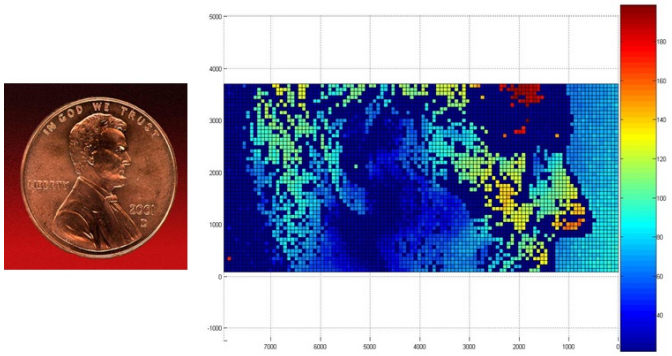

Fig. 3.11. Height map of 8 mm x 3.5 mm section of Lincoln's face on a copper penny

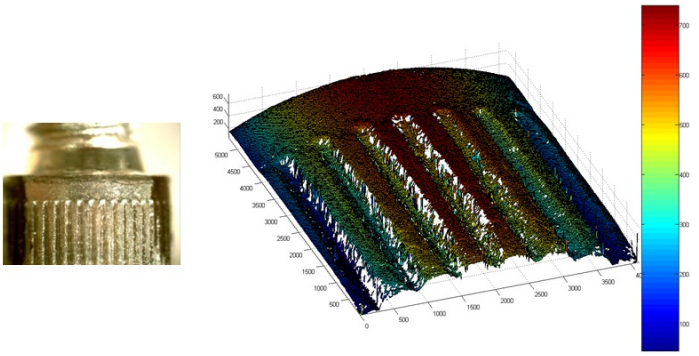

Fig. 3.12. 3D view of a size 4-20 screw head

3.5 Discussion

An important factor that limits the measurement of weak reflections at steeper angles from the sample is the system sensitivity. As can be seen from eq. (3), the system sensitivity can be increased by increasing the source power incident on the sample or the camera exposure time. While the above equation is only valid for a shot noise limited light source, the SC source in our setup was generated by a modulation instability process and hence suffered from additional amplitude fluctuations [11]. The noise of the SC source was determined to be ~1.5x higher than the shot noise limit producing a degradation of 3.5 dB in the system sensitivity. However, in section 3.3.2, the difference between the theoretical and experimental sensitivity was measured as 4.7 dB. Possible reasons for the additional 1.2 dB degradation include numerical errors in the interferogram re-sampling process and mechanical vibration instabilities in the interferometer.

The problem of excessive noise can be solved by replacing the SC source with a low noise broadband super-luminescent diode (SLD). SLDs with a center wavelength of 825 nm, 60 nm of 3 dB bandwidth and >15 mW of single mode fiber coupled output power are already commercially available. While the SLD would offer near shot noise limited performance, the main drawback would be the reduction in the system's axial resolution. While our 100 nm wide SC centered at 650 nm has a theoretical coherence length of 2.1 μm, the SLD based system would only have 5.7 μm of coherence length. Given an identical improvement factor using super-resolution, the SLD based system would have ~340 nm of z-resolution compared to the 125 nm of the current SC based system.

Finally, the limitation in the scan speed of the line scan system and the potential for improvements is investigated. The system demonstrated in this paper measures a 5.7 mm x 15 μm area every 0.5s with a typical camera exposure time of 100 μs. Even though the camera is capable of 15 fps operation, our custom Labview program used to control the sample stepper motor and frame grabber card currently operates at just 2 fps. Thus, while

there is sufficient source power to make measurements with just 100 μs of camera exposure time, the speed bottleneck arises from the extremely slow frame rate of the camera. In theory, one can achieve a 1000x improvement in speed using a 2,000 fps camera and still be limited by the frame rate and not a lack of SNR. Watanabe et. al. [15] have demonstrated a high speed line field FD-OCT system using a 1500 fps CMOS camera for in-vivo measurement of a human finger-tip.

Another way to increase speed with limited camera frame rates is to increase the line length incident on the sample surface. In our system, an 8 mm line was incident on the sample of which only the central 5.7 mm was used for processing to ensure more uniform sample illumination intensity. The length of the line was determined by the imaging performance of the cylindrical lens CL1 in Fig. 3.1. While large diameter high performance spherical lenses are easily available off the shelf, obtaining an achromatic and diffraction limited performance cylindrical lens of >1" diameter requires expensive custom design and manufacturing. However, with a combination of longer line length and higher scanning speed, the system may potentially be suitable for rapid in-line inspection of bumped wafers.

3.6 Summary

In summary, a visible supercontinuum based line scan FD interferometer with an axial resolution of 125 nm, lateral resolution of 15 μm and sensitivity of 70.4 dB was demonstrated. The above system was used for the simultaneous height and top shape measurement of ~300 μm high solder balls on a semiconductor die sample. By measuring over a +/- 20 degree angle down the ball tops, solder ball shape defects such as flat top, damaged center and incorrect location were successfully identified. The ability to measure curved surfaces at large incidence angles was strongly dependent on the surface roughness of the sample and was limited by the intensity fluctuations of the SC source. The line scan system successfully demonstrated measurement over +/- 60 degrees on a rough 3.17 mm diameter steel ball bearing sample. Finally, it was determined that the

commercial viability of a wafer inspection system required an increase in scan speed of the system, which was currently limited by the camera frame rate.

References

1. Akira Ishii and Jun Mitsudo, “Constant-magnification varifocal mirror and its application to measuring three-dimensional (3-D) shape of solder bump,” IEICE Trans. Electron. E90-C, 6-11 (2007)
2. Takefumi Ohta, Norihiko Nishizawa, Tetsuya Ozawa, and Kazuyoshi Itoh, "Highly-sensitive and high-resolution all-fiber three-dimensional measurement system," Appl. Opt. **47**, 2503-2509 (2008)
3. Takefumi Ohta, Norihiko Nishizawa, Tetsuya Ozawa, and Kazuyoshi Itoh, "High-speed three-dimensional measurement using electronically controlled wavelength-tunable ultrashort pulse fiber laser," Opt. Lett. **34**, 1921-1923 (2009)
4. D. Reolon, M. Jacquot, I. Verrier, G. Brun, and C. Veillas, "Broadband supercontinuum interferometer for high-resolution profilometry," Opt. Express **14**, 128-137 (2006)
5. Takashi Endo, Yoshiaki Yasuno, Shuichi Makita, Masahide Itoh, and Toyohiko Yatagai, "Profilometry with line-field Fourier-domain interferometry," Opt. Express **13**, 695-701 (2005)
6. Yoshiaki Yasuno, Takashi Endo, Shuichi Makita, Gouki Aoki, Masahide Itoh, and Toyohiko Yatagai, “Three-dimensional line-field Fourier domain optical coherence tomography for in vivo dermatological investigation”, J. Biomed. Opt. **11**, 014014 (2006)
7. Yoshifumi Nakamura, Shuichi Makita, Masahiro Yamanari, Masahide Itoh, Toyohiko Yatagai, and Yoshiaki Yasuno, "High-speed three-dimensional human retinal imaging by line-field spectral domain optical coherence tomography," Opt. Express **15**, 7103-7116 (2007)
8. Maciej Wojtkowski, Vivek Srinivasan, Tony Ko, James Fujimoto, Andrzej Kowalczyk, and Jay Duker, "Ultrahigh-resolution, high-speed, Fourier domain optical coherence tomography and methods for dispersion compensation," Opt. Express **12**, 2404-2422 (2004)
9. Christophe Dorrer, Nadia Belabas, Jean-Pierre Likforman, and Manuel Joffre, "Spectral resolution and sampling issues in Fourier-transform spectral interferometry," J. Opt. Soc. Am. B **17**, 1795-1802 (2000)
10. Michael Choma, Marinko Sarunic, Changhuei Yang, and Joseph Izatt, "Sensitivity advantage of swept source and Fourier domain optical coherence tomography," Opt. Express **11**, 2183-2189 (2003)
11. Malay Kumar, Chenan Xia, Xiuquan Ma, Vinay V. Alexander, Mohammed N. Islam, Fred L. Terry, Carl C. Aleksoff, Alex Klooster, and Douglas Davidson, "Power adjustable visible supercontinuum generation using amplified nanosecond gain-switched laser diode," Opt. Express **16**, 6194-6201 (2008)

12. N. Nassif, B. Cense, B. Park, M. Pierce, S. Yun, B. Bouma, G. Tearney, T. Chen, and J. de Boer, "In vivo high-resolution video-rate spectral-domain optical coherence tomography of the human retina and optic nerve," Opt. Express **12**, 367-376 (2004)
13. Michael A. Choma, Kevin Hsu, and Joseph A. Izatt, “Swept source optical coherence tomography using an all-fiber 1300-nm ring laser source”, J. Biomed. Opt. **10**, 044009 (2005)
14. R. Leitgeb, W. Drexler, A. Unterhuber, B. Hermann, T. Bajraszewski, T. Le, A. Stingl, and A. Fercher, "Ultrahigh resolution Fourier domain optical coherence tomography," Opt. Express **12**, 2156-2165 (2004)
15. Yuuki Watanabe, Kazuhiko Yamada, and Manabu Sato, "Three-dimensional imaging by ultrahigh-speed axial-lateral parallel time domain optical coherence tomography," Opt. Express **14**, 5201-5209 (2006)

Chapter 4

Mid-infrared supercontinuum generation in ZBLAN fiber

4.1 Introduction

Light sources in the mid-IR wavelength range are useful for a number of applications including spectroscopy [1], remote sensing [2], free-space communication [3] and bio-medical ablation [4]. While conventional blackbody radiators such a silicon carbide 'Globar' source provide continuous spectral coverage from 2-20 μm, the low output power and poor spatial coherence make them unsuitable for most applications other than a light source for an FTIR spectrometer. On the other hand, laser based sources may overcome the above disadvantages but are typically either single line or tunable over a limited wavelength range. The most common way of producing laser light in the mid-IR light is using optical parametric oscillators [5] / optical parametric amplifiers [6] or quantum cascaded lasers [7]. While the former requires a complicated setup with multiple free space optical components, the latter often requires cryogenic temperatures for high power operation. A supercontinuum laser source, on the other hand, combines the broad continuous wavelength coverage of a lamp and the high spatial coherence and output power of a laser. The all-fiber integrated mid-IR SC source demonstrated in this chapter is power scalable with no moving or free space parts, operates at room temperature, covers multiple atmospheric transmission windows and has excellent beam quality due to the single mode fiber output.

Mid-IR SC generation in optical fibers has been demonstrated using a variety of laser sources and fiber materials. The conventional approach involves the use of high peak power femtosecond pulses from a mode locked laser [8] to pump a low mid-IR loss fiber composed from fluoride [9], chalcogenide [10] or tellurite [11] glass. A novel technique to eliminate the need for mode-locked lasers was demonstrated by Xia et. al. [12] using a two step SC generation process. In the first step, modulation instability in standard SMF is used to initiate pulse break-up of quasi-continuous wave nanosecond laser diode pulses at 1.55 μm. In the next step, the high peak power pulses from the first stage are coupled into ZBLAN fluoride fiber to generate a broad supercontinuum through stimulated Raman scattering and other non-linear effects such as self phase modulation and four wave mixing. While the experiments in this chapter are based on the sample platform as [12], we achieve substantially higher output power in the longer wavelength bands of the SC. We achieved this by scaling up the amplifier gain fiber size, using higher power pump diodes, improved thermal management and careful selection of ZBLAN fiber parameters such as core size, cut-off wavelength and numerical aperture [13].

The key results obtained in this chapter are described below. We demonstrate a mid-IR SC source extending from 800-4300 nm with 3.9 W total output power (with 50% modulation) and 0.5W average power in the region beyond 3800 nm. Light at 1543 nm from a seed laser diode was amplified to ~ 20 kW peak power in a dual stage cladding pumped Er-Yb fiber amplifier (EYFA) system before being coupled into a 9 m ZBLAN fiber with an 8 μm core and 0.27 NA. The SC output was power-scalable and the maximum output power was limited by the available pump power.

The layout of this chapter is organized as follows. The experimental setup for mid-IR SC generation is described in section 4.2. Section 4.3 describes the experimental results related to the power-amp characterization, output from the ZBLAN fiber and scalability of the SC output power. A discussion related to the fiber output end degradation is contained in section 4.4 followed by a summary of the results in section 4.5.

4.2 Experimental setup

Figure 4.1 below shows the layout of the system used for generation of the mid-IR SC extending from 0.8 – 4.3 μm. First, a pulse generator is used to produce 0.5 ns pulses at variable repetition rates from a 1543 nm DFB seed laser diode. The entire system was modulated at 500 Hz with a 50% duty cycle to reduce the thermal load on the various components. The light is then amplified in a pre-amp stage comprising 2 m of a 7/125 μm cladding pumped Er-Yb gain fiber. The gain fiber is forward pumped by a 1W 976 nm pump diode coupled into the gain fiber via a 6+1:1 pump combiner. The light is then filtered by a narrowband (0.8 nm FWHM) filter centered at the seed wavelength to remove the out of band ASE from being further amplified in the next amplifier stage.

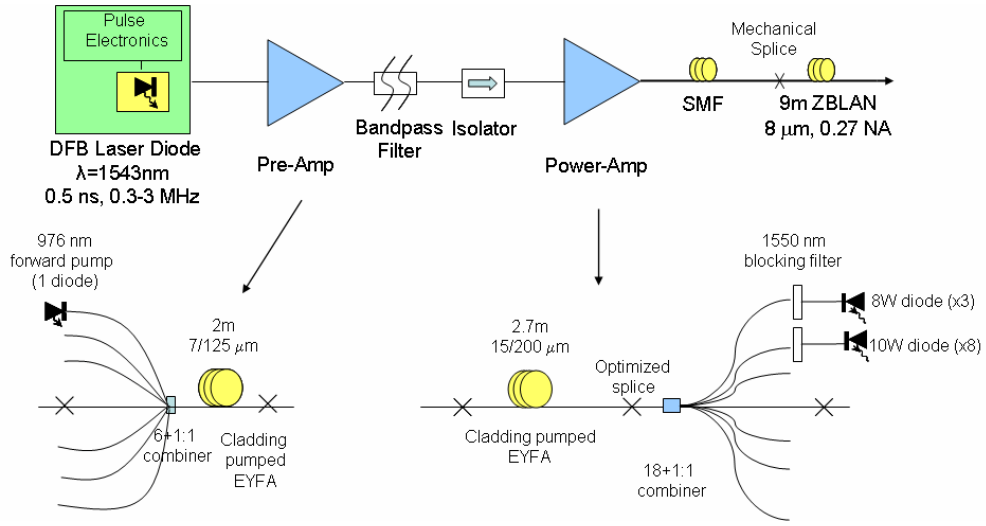

Fig. 4.1. Experimental setup for mid-IR SC generation

After passing through an isolator, the light is further amplified to ~20 kW of peak power by the power-amp stage comprising of a backward pumped 2.7 m long 15/200 μm EYFA. An 18+1:1 pump combiner is used with eight 976 nm 10 W pump diodes and three 976 nm 8 W pump diodes for a maximum pump power of 104 W (52W with modulation). Protection filters in front of each pump diode provide 30 dB of blocking at the seed wavelength (1543 nm) with only 0.3 dB of insertion loss at the pump wavelength (976 nm).

After the experiments described in this chapter were performed, it was found that the vendor for the 18+1:1 no longer manufactured the above part. Thus, the setup was modified as follows for the spectroscopy experiments described in the next chapter. First, the 18+1:1 combiner was replaced with a 6+1:1 combiner from the same vendor. Next, the 10W and 8W pump diodes were replaced with 30W diodes in order to obtain the same pump power as before with a lower number of available ports. Finally, we added TE coolers to cool the new pump diodes instead of the passive heat sinks that were sufficient before. Despite all the changes, we obtained nearly identical results as before thus confirming that the power-amp output was only dependent on total pump power regardless of the power of each individual diode and number of combiner ports.

Since the power-amp gain fiber to combiner splice is the highest power point in the whole system, thermal management [14] of the splice to prevent damage is extremely important. It is also necessary to recoat the bare spliced fibers with a low index epoxy to confine the pump light in the cladding and prevent it from leaking out. A commercial re-coater was used to coat the fiber splice area with a uniform 200 μm thin layer of low index epoxy followed by placing the first 40 cm of the gain fiber in a copper heat sink (Fig. 4.2) with a machined groove equal in size to the jacket diameter (350 μm) of the gain fiber. Initial testing with a much shorter heat sink length showed brown discoloration of the section of gain fiber just beyond the heat sink after a few hours. Since the switch to the longer 40 cm heat sink, no discoloration or other indication of thermal damage on the gain fiber was observed.

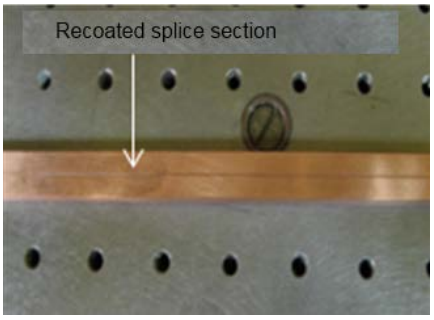

Fig. 4.2. Copper heat sink with machined groove for power-amp gain fiber

Finally, the output from the power-amp was coupled into a 9 m ZBLAN fiber (8/125 μm, 0.27 NA) via a mechanical fiber alignment stage. Since ZBLAN has a much lower melting point of 265ºC compared to 1200ºC for fused silica, it is not possible to fusion splice the SMF output from the power-amp stage to the input end of the ZBLAN fiber. Instead, the following procedure was used to couple light into the ZBLAN fiber. First, the output end of the SMF was angle cleaved at ~8 degrees to avoid harmful back reflections into the power-amp stage. Next, the ZBLAN input end was also cleaved at the same angle and mounted on a rotation stage. Both ends were placed on a v-groove, placed on a 3-axis nano-max coupling stage and aligned under a microscope till a maximum coupling efficiency ~ 70% was achieved.

4.3 Experimental Results

4.3.1 Characterization of power-amp output

In order to obtain the best possible efficiency from the power-amp stage, the splice point between the dual clad Er/Yb power-amp gain fiber and the 18+1:1 combiner must be carefully optimized. There are two main reasons why the quality of this splice is critical. First, if the spice is of poor quality, the amplified 1543 nm signal from the gain fiber can get coupled into the cladding of the combiner. Since our power amplifier stage is backward pumped, this amplified signal can make its way back to the pumps and could possibly damage them. Second, the backward pumped 976 nm light from the combiner may not get fully coupled into the gain fiber due to a poor splice, which would reduce the amount of pump power absorbed.

The splice parameters such as arc current and fusion time were modified to minimize the splice loss between the two fibers. The 1543 nm signal leaking into the combiner pump ports was used as a metric to check the quality of the splice. With an optimized splice, only ~0.7% of the power-amp output leaked into each pump port of the combiner compared to ~3.0% before the optimization. The power-amp efficiency (power-amp average output power / input pump power) as a function of output peak power is shown

in Fig. 4.3 and was measured both before and after optimization of the splice. In both cases, there is a decrease in efficiency with increasing peak power due to non-linear spectral broadening of the signal within the gain fiber itself. However, under the operating condition of 20 kW, the power-amp efficiency before the splice optimization was ~11% and after optimization was ~16%. Thus, we achieved a 45% improvement in efficiency through optimization of the splice parameters.

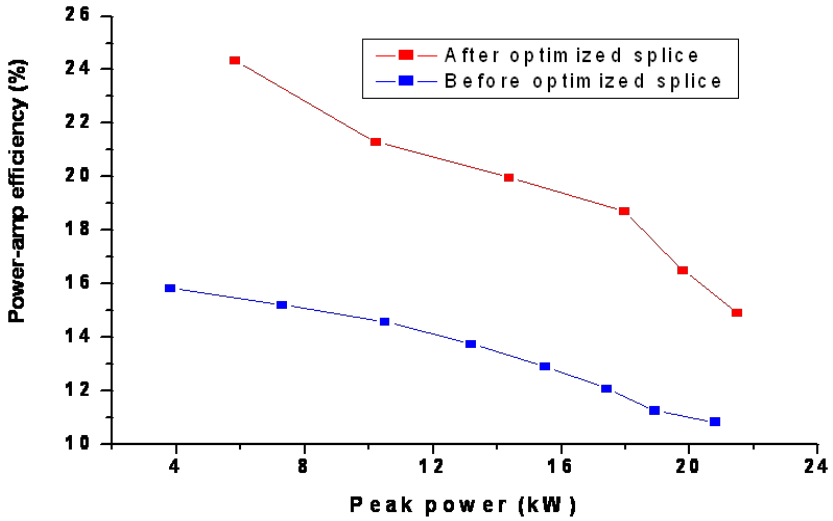

Fig. 4.3. Power-amp efficiency versus peak power before and after optimized splice

4.3.2 Mid-IR SC generation in ZBLAN fiber

At the highest pump power of 52W (modulated), we measured 3.9W of average output power and a SC spectrum extending from 800-4300 nm (Fig.4.4) from the output of the ZBLAN fiber. The spectrum had better than 2 dB flatness from 2500-4200 nm. The shape of the SC spectrum was corrected for both the detector and grating response and the y-axis was scaled to represent the total SC output power as the area under the curve. Table 4.1 shows the power in different wavelength bands of the SC measured by using appropriate long pass filters and a power meter. Based on previous work by Xia et.al [12], we believe that the broad SC is generated by non-linear effects such as modulation instability and stimulated Raman scattering while the long wavelength edge is limited by the inherent material absorption loss of the ZBLAN glass.

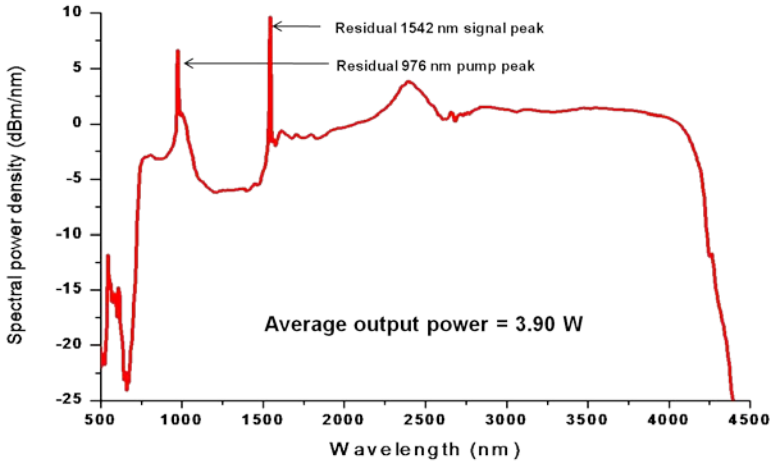

Fig. 4.4. SC output from 9m ZBLAN fiber with 3.9W output power

Pump power (976 nm)	52 W
Power-amp output (1543 nm)	9.60 W
ZBLAN output (entire SC)	3.91 W
1800 nm LP	2.67 W
2500 nm LP	1.98 W
3000 nm LP	1.29 W
3500 nm LP	0.68 W
3800 nm LP	0.51 W

Table 4.1. Spectral power distribution of SC output

4.3.3 Power-scalability of SC output

A unique feature of the SC system is the ability to scale the average output power, while maintaining the same spectral shape, and hence, the same fractional distribution of power in different wavelength bands. We accomplish this by increasing the repetition rate of our seed laser along with a proportional increase in the 976 nm pump power, while maintaining a constant peak power going into the ZBLAN fiber [15]. Figure 4.5 shows the linear increase in the SC average output power with an increase in the seed laser

repetition rate, with the corresponding 976 nm power-amp pump power labeled next to the data point. The results shown in Fig. 4.4 and Table 4.1 correspond to our highest power results obtained at the 2 MHz repetition rate and 52 W pump power. Further increase in output power was only limited by the available pump power, and we expect the results to scale up with higher pump power and thermal management of the critical splice points and power-amp gain fiber.

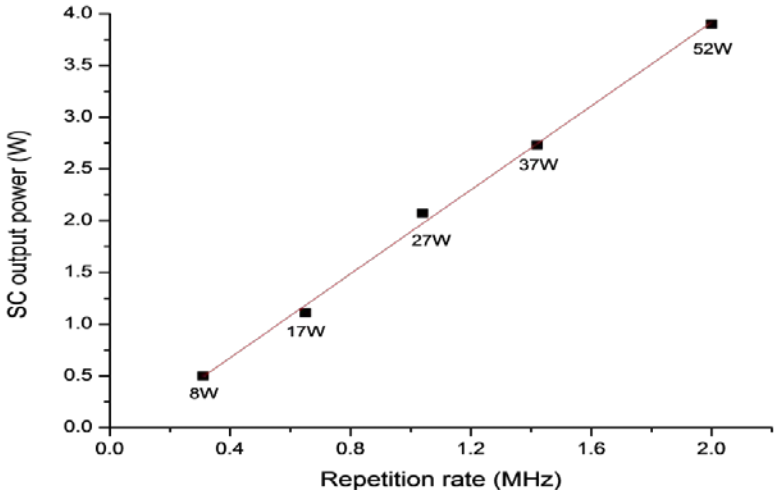

Fig. 4.5. SC output from 9m ZBLAN fiber with 3.9W output power

4.4 Discussion

During the course of the experiments, we observed a consistent degradation of the ZBLAN output end when operating at peak powers ~ 18 kW or higher. The output end damage did not occur at lower peak powers, while at the input end, we never observed any damage regardless of the operating peak power. We believe that output end damage is related to joule heating of the glass material [16] and can be attributed to the following reasons. At high input peak powers >18 kW, the SC output spectrum extends out to ~4300 nm, close to the ZBLAN material absorption edge. The increased absorption coefficient at longer wavelengths causes the core temperature to rise, and ultimately damage the fiber end when it nears the glass transition temperature. The cascaded Raman process responsible for SC generation results in the longer wavelengths being generated

towards the output side of the fiber. Thus, at the input side of the ZBLAN, there is low absorption only due to the pump wavelength at 1543 nm, and we do not observe any damage to this end. Another reason for the damage only occurring at the output end and not anywhere else along the length of the fiber is related to the fiber geometry. The end of the fiber is in thermal contact with the glass on one side, and air on the other. Since air is a poor thermal conductor, the ends of the fiber experience lower conductive cooling compared to the rest of the fiber, and are more susceptible to thermal damage.

A possible solution to the above problem is the end-capping [17] the single mode ZBLAN fiber. This process involves splicing a small section of multimode ZBLAN fiber to the output end of the single mode ZBLAN. The large-core diameter (~100 μm) of the multimode fiber allows for expansion of the optical beam emerging from the 8 μm core ZBLAN fiber currently used for SC generation. The end cap prevents output end damage since the long-wavelength absorption induced heating is now spread over a much large surface area. The configuration of fiber-end caps is shown in Fig. 4.6. The main parameter involved in the design of fiber end-caps is the length of the multimode fiber section. To prevent distortion of the single spatial mode of the beam output from the single mode fiber, the length of the end-cap must be small enough so as not to let the diverging beam expand to dimensions larger than the core of the multimode fiber. This in turn is limited by the largest cladding multimode fiber than can be reliably spliced onto the 125 μm single mode fiber cladding. Calculations suggest that for a 100 μm core multimode fiber the end-cap length must be smaller than 0.2 mm.

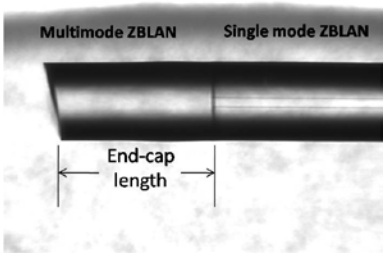

Fig. 4.6. Schematic of ZBLAN fiber end-cap

4.5 Summary

In summary, a mid-IR SC extending from 0.8-4.3 μm with 3.9 W average output power and 0.51 W beyond 3800 nm (with 50% modulation) was generated in 9 m ZBLAN fiber pumped by 1543 nm light from a dual stage EYFA system. Careful thermal management and optimization of the power-amp gain fiber to combiner splice was required to obtain the high power SC spectrum. Degradation of the ZBLAN output end was observed at input peak powers >18 kW and can possibly be prevented through the use of a multimode fiber end-cap to reduce the beam intensity.

References

1. J. Hult, R.S. Watt, C.F. Kaminski, "High bandwidth absorption spectroscopy with a dispersed supercontinuum source," Opt. Express **15**, 11385-11395 (2007)
2. C.J. Zarobila, H.J. Patrick, “Supercontinuum fiber laser source for reflectance calibrations in remote sensing”, Proc. of SPIE **7807**, 78070B (2010)
3. K.D.F. Büchter, H. Herrmann, C. Langrock, M. M. Fejer, and W. Sohler, "All-optical Ti:PPLN wavelength conversion modules for free-space optical transmission links in the mid-infrared," Opt. Lett. **34**, 470-472 (2009)
4. K. Ke, C. Xia, M.N. Islam, M.J. Welsh, M.J. Freeman, "Mid-infrared absorption spectroscopy and differential damage in vitro between lipids and proteins by an all-fiber-integrated supercontinuum laser," Opt. Express **17**, 12627-12640 (2009)
5. M. Ebrahimzadeh, “Mid-infrared ultrafast and continuous-wave optical parametric oscillators”, Solid-state mid-infrared laser sources, Springer-Verlag Berlin (2003)
6. G. Cerullo, S. De Silvestri, “Ultrafast optical parametric amplifiers”, Rev. Scientific Instr.**74**, 1-18 (2003)
7. C. Gmachl, F. Capasso, D.L. Sivco, A.Y. Cho, “Recent progress in quantum cascade lasers and applications”, Reports on progress in Physics **64**, 1533-1601 (2001)
8. C. L. Hagen, J.W. Walewski, S.T. Sanders, “Generation of a continuum extending to the midinfrared by pumping ZBLAN fiber with an ultrafast 1550-nm source,” IEEE Photon. Technol. Lett. **18**, 91-93 (2006)
9. G. Qin, X. Yan, C. Kito, M. Liao, C. Chaudhari, T. Suzuki, and Y. Ohishi, "Supercontinuum generation spanning over three octaves from UV to 3.85 μm in a fluoride fiber," Opt. Lett. **34**, 2015-2017 (2009)
10. R.E. Slusher, G. Lenz, J. Hodelin, J. Sanghera, L.B. Shaw, I.D. Aggarwal, “Large Raman gain and nonlinear phase shifts in high purity As2Se3 chalcogenide fibers”, JOSA B **21**, 1146-1155 (2005)
11. M. Liao, C. Chaudhari, G. Qin, X. Yan, T. Suzuki, Y. Ohishi, "Tellurite microstructure fibers with small hexagonal core for supercontinuum generation," Opt. Express **17**, 12174-12182 (2009)
12. C. Xia, M. Kumar, O. P. Kulkarni, M. N. Islam, F. L. Terry, Jr., M. J. Freeman, M. Poulain, G. Mazé, "Mid-infrared supercontinuum generation to 4.5 μm in ZBLAN fluoride fibers by nanosecond diode pumping," Opt. Lett. **31**, 2553-2555 (2006)
13. C. Xia, Z. Xu, M.N. Islam, F.L. Terry Jr., M.J. Freeman, A. Zakel, J. Mauricio, “10.5W time-averaged power mid-IR supercontinuum generation extending beyond 4 micron with direct pulse pattern modulation”, IEEE Sel. Top. Quant. Elec. **15**, 422-434 (2009)
14. D.C. Brown and H.J. Hoffman, “Thermal, Stress, and Thermo-Optic Effects in High Average Power Double-Clad Silica Fiber Lasers”, IEEE J. of Quant. Electronics, **37**, 207-217 (2001).

15. M. Kumar, C. Xia, X. Ma, V.V. Alexander, M. N. Islam, F. L. Terry, C. C. Aleksoff, A. Klooster, and D. Davidson, "Power adjustable visible supercontinuum generation using amplified nanosecond gains-witched laser diode," Opt. Express **16**, 6194-6201 (2008)
16. B. C. Stuart, M. D. Feit, S. Herman, A. M. Rubenchik, B. W. Shore, and M. D. Perry, “Nanosecond-to-femtosecond laser-induced breakdown in dielectrics,” Phys. Rev. B **53**, 1749-1761 (1996)
17. J. Limpert, S. Höfer, A. Liem, H. Zellmer, A. Tünnermann, S. Knoke, H. Voelckel, “100W average-power high energy nanosecond fiber amplifier”, App. Phys. B **75**, 477-479 (2002)

Chapter 5

Stand-off reflection spectroscopy using a mid-infrared supercontinuum source

5.1 Introduction

Diffuse reflection spectroscopy is a widely used technique for both qualitative and quantitative analysis of IR active samples. The most common method involves the use of a conventional Fourier transform infrared (FTIR) instrument fitted with an attenuated total reflection or diffuse reflectance measurement accessory [1]. While the above technique covers the entire near-IR to far-IR spectral range of 0.8-20 μm, the substance to be analyzed must be confined to the sample chamber of the instrument, thereby limiting its use to offline measurements in a laboratory environment. Recent advances in mid-IR fiber technology have enabled the use of fiber probe accessories for use with FTIR instruments. Fiber optic reflectance spectroscopy uses fluoride or chalcogenide fiber bundles that enable portable field analysis by allowing the light to be transmitted and collected outside the sample chamber [2,3]. However, poor SNR due to the lamp light source and fiber loss restrict the distance of the sample from the fiber probe tip to a few centimeters.

The need for stand-off detection of samples requires the transition from lamp based sources to high power and high spatial coherence laser sources. For the detection of gases, lasers with very low line width are ideal due to the narrow spectral absorption features of the gas. The differential absorption light detection and ranging (DIAL) [4] technique uses two laser wavelengths (either discrete or tunable) to measure the concentration of gases at distances of up to a few kilometers. The technique works by measuring the relative difference in the back-scattered signal from the two lasers – one which is tuned to the center of an absorption peak while the other is tunes outside the peak. However, each target gas requires the use of different laser sources in the respective absorption bands or a widely wavelength tunable source, such as an optical parametric amplifier/oscillator.

Remote Raman spectroscopy is a popular technique for identification of solid and liquid samples at stand-off distances. The sample is illuminated with a high energy pulse from a visible or ultraviolet YAG laser, and the emitted Raman spectrum unique to the sample is detected with a gated charge coupled device camera. While this technique offers excellent overall selectivity, some samples are difficult to analyze due to fluorescence caused by the intense pump beam. Another drawback is the need for extremely sensitive detection with large collection optics due to the inherent weak nature of the Raman effect. However, the sensitivity can be increased using resonance Raman spectroscopy [5], in which the probe laser wavelength tuned near an electronic transition within the molecule gives rise to significant enhancement of certain Raman lines. Coherent anti-stokes Raman spectroscopy [6] is another variation to improve sensitivity, though at the cost of a big increase in system complexity. It is based on a non-linear conversion of three laser beams into a coherent laser-like Raman beam of high intensity in the anti-Stokes wavelength region. Stand-off Raman spectroscopy has successfully been used in the fields of geology, chemical sensing and explosives detection at distances of up to 200 m [7].

Laser induced breakdown spectroscopy (LIBS) is another widely used technique for stand-off detection of explosives at distances of up to 50m [8]. A high energy laser pulse is used to create a plasma on the sample surface, and the characteristic atomic emission lines of the constituent elements are analyzed to determine the sample composition. However, the high beam intensity required for the breakdown limits the spot size on the sample to a few millimeters and may cause thermal degradation of the samples. While LIBS offers high sensitivity, the selectivity of the technique is reduced due to contamination from atmospheric gases. A different technique called photofragmentation laser induced fluorescence (LIF) uses an initial fragmentation of the explosive molecule followed by LIF detection of characteristic fragments [9]. The technique is used to detect the NO molecule and is thus limited to explosives containing the nitro group. Photo-thermal spectroscopy [10] is another novel method that has been recently shown to detect the presence of explosive residues at 1m distance using tunable quantum cascade lasers. As the laser is tuned to the peak of an absorption feature of the sample of interest, a thermal camera is used to measure the rise in temperature of the sample. The limitation of this technique is similar to DIAL, i.e. each sample of interest requires a different laser specifically tuned to the absorption wavelength.

In this chapter, we demonstrate the detection of solid targets at a stand-off distance of 5m with diffuse reflection spectroscopy using a mid-IR supercontinuum (SC) light source. The SC output spectrum extends from 0.75-4.3μm, has a maximum time-average output power of 3.9W and is obtained by pumping a 9m long ZBLAN fluoride fiber with the output of a dual stage Erbium-Ytterbium fiber amplifier. The SC source is used to obtain the reflection spectra of a wide range of samples including explosives, fertilizers and paint coatings. We observe unique spectral fingerprints in the near and mid-IR wavelength regions of the reflection spectrum, and develop a correlation function based algorithm to distinguish between the samples. The demonstrated SC light source has excellent beam quality due to the single mode fiber output, covers multiple atmospheric

transmission windows and is all-fiber integrated with no moving parts or free space optics. Thus, it is well suited for spectroscopy applications in a wide range of fields such as defense, homeland security, remote sensing, geology and others.

This chapter is organized as follows. We begin by evaluating the feasibility of using the SC source for spectroscopy in a simple transmission spectroscopy setup. The experimental setup is described in section 5.2 with the corresponding results in section 5.3. The details of the experimental setup for stand-off reflection spectroscopy are provided in section 5.4 while the experimental results obtained with three different sample sets are described in section 5.5. The first set consists of 4-8% explosives deposited on fused silica crystals. The second set consists of a variety of samples such as ammonium nitrate, urea, gypsum and pine wood. The third set consists of aluminum blocks painted with different automotive and military paints. The repeatability of the reflectance measurements and comparison of the stand-off spectra with that obtained using an FTIR instrument are also described in this section. Section 5.6 describes a correlation algorithm for distinguishing between the different samples on the basis of their unique reflection spectra. The various performance metrics of the system, their limitations and scope for further improvement are discussed in section 5.7. Finally, we summarize the results in section 5.8.

5.2 Experimental setup – transmission spectroscopy

The experimental setup for a SC based transmission spectroscopy system is shown below in Fig. 5.1. The mid-IR SC described in Chapter 4 is used as the light source for the experiments. First, the light exiting from the output ZBLAN fiber of the SC source is collimated using a CaF_2 lens and then focused into the entrance slit of the monochromator. At the exit slit, light at the selected wavelength is collimated again and passed through a mid-IR polarizer before being incident on a calcium fluoride beam splitter. The polarizer is essential to the setup since the split ratio of the beam splitter is strongly dependent on the polarization state of the input light. After passing through the

beam splitter, the light is split into a sample and reference arm to enable ratiometric detection that will cancel out effects of intensity fluctuations in the SC source. The light in the sample arm passes through the sample of interest and then focused onto a HgCdTe detector connector to a pre-amp. A chopper and lock-in amplifier setup enable low noise detection of the sample arm signal. The light in the reference arm passes through an empty container (cuvette, gas cell etc.) of the same kind as used in the sample arm. An identical detector, pre-amp and lock-in amplifier is used for detection of the reference arm signal.

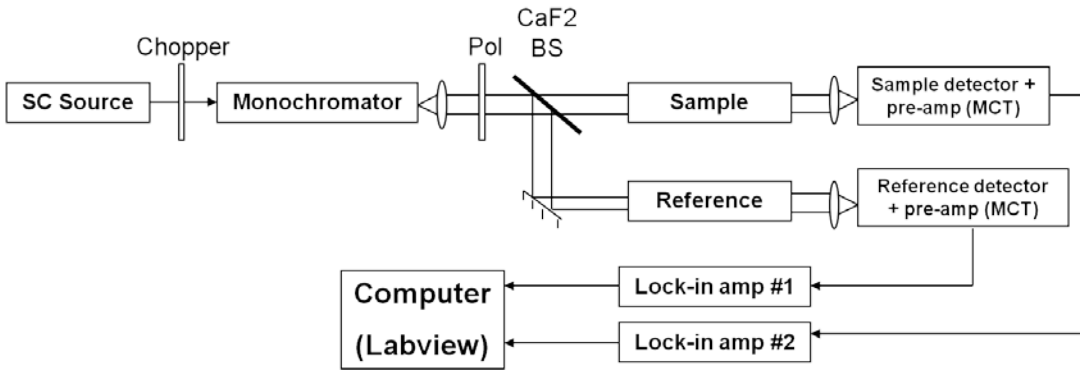

Fig. 5.1. Experimental setup for SC based transmission spectroscopy

The process of obtaining a transmission spectrum of the sample requires a two step process. First, a background wavelength scan is performed with no sample in the sample arm. The ratio of the sample signal to reference signal is used to determine the wavelength dependence of the beam splitter split ratio. Next, the sample of interest is inserted into the sample arm and another wavelength scan is taken. Again, the wavelength dependent ratio of the sample signal to reference signal is computed. Finally, dividing the main scan ratio to the background scan ratio gives the absorption spectrum of the sample free from any wavelength dependent artifacts of the system optics.

5.3 Experimental results – transmission spectroscopy

In the first set of experiments, we wanted to compare the transmission spectrum shape obtained via the SC based system to that in the NIST database [11] for an easily available

set of test substances. We decided to use acetone and ethanol as our test substances since the high vapor pressure of these volatile liquids enabled us to transmit the beam through the vapors above the liquid level rather than through the liquid itself. The liquids were held in a glass cuvette with CaF_2 windows and a 2 cm path length. The obtained transmission spectra of the acetone and ethanol vapor are shown in the blue curves in Fig. 5.2 and Fig 5.3 respectively. Since the windows of the cuvette were not wedged and a collimated beam was incident upon them, distinct Fabry Perot fringes were superimposed on the resulting spectrum. This is a well known problem is transmission spectroscopy and can easily be solved by using a container with wedged windows. Alternately, the spectrum can also be numerically low-pass filtered to remove the high frequency fringes while maintaining the shape of the comparatively broader spectral features of the sample.

The transmission curves in the NIST spectral database are shown in red to the right of the blue curves. For both the acetone and ethanol samples, there is an excellent agreement in the shape of the 2 curves but a difference in the absolute transmission percentage levels. This difference is attributed to two reasons. First, the path length in the NIST data is 5 cm while that for the SC measurements is 2 cm. Thus, we expect the NIST data to have higher absorption i.e. lower transmission than the SC data. Second, the vapor pressure in the 2 cases is different. For the SC measurements, the liquids were kept in an open top bottle at atmospheric pressure resulting in some equilibrium vapor pressure on the top of the liquid. For the NIST measurements, the vapor pressure was explicitly controlled and set to be 100 mm of Hg for acetone and 30 mm of Hg for ethanol. Different vapor pressures imply a different concentration of the test samples and thus a difference in absorption and a corresponding difference in the transmission percentage. No effort was made to determine the vapor pressure for our SC measurements or setup a gas-cell with a pressure gauge as the motivation behind this set of experiments was to only qualitatively verify that the correct transmission spectrum shape was obtained with our system.

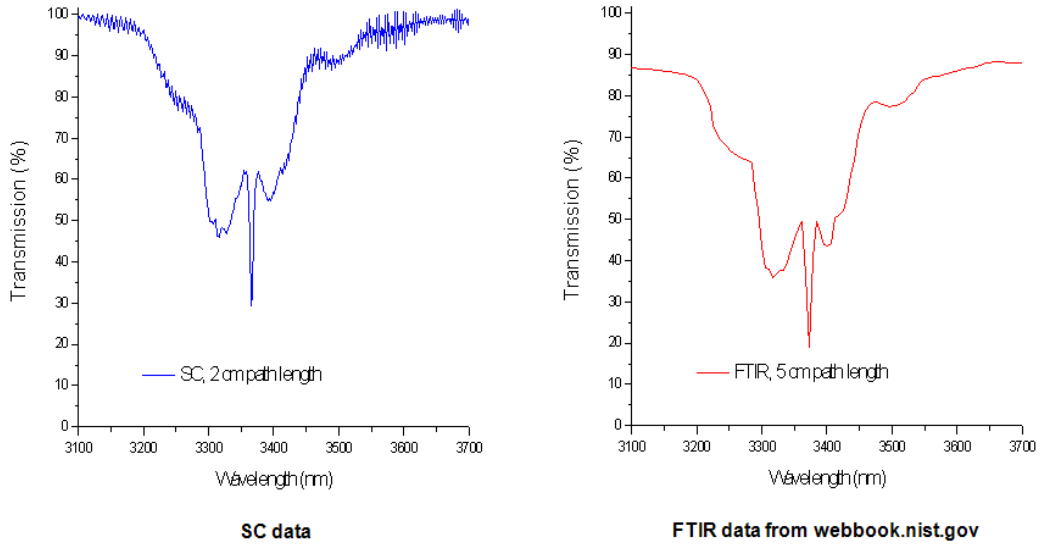

Fig. 5.2. Comparison of acetone transmission spectrum from SC and NIST database

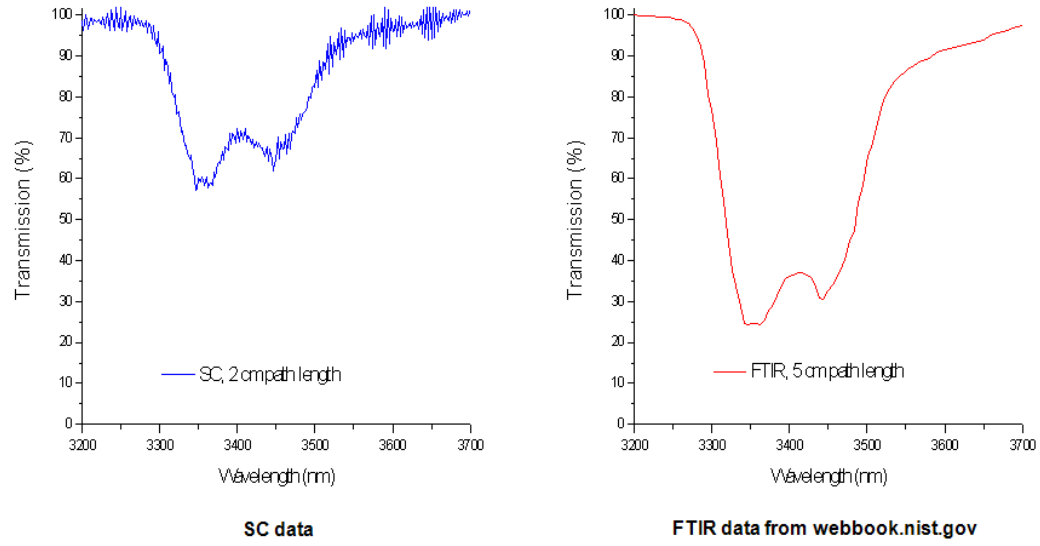

Fig. 5.3. Comparison of ethanol transmission spectrum from SC and NIST database

While transmission spectroscopy is relatively straightforward for samples in the gas phase, additional sample preparation steps are required to analyze solid powdered samples. Typically, the sample is ground in a mortar and pestle and diluted (~1%) with a non-absorbing powder such as KBr. The resulting mix is then pressed into a transparent pellet using a steel die and can be analyzed by placing the disc in the conventional beam path of a transmission spectroscopy setup. However, since we did not have access to a pellet press, we used an alternate technique to prepare our powdered samples for

inspection [12]. In this technique, a small amout of the sample (~10 mg) was first ground in a mortal and pestle along with a substance called Nujol to create a mull i.e. a thick suspension. Nujol is a heavy paraffin oil which is chemically inert and has a relatively featureless IR spectrum. A thin layer of the mull was then sandwiched between an IR transparent KCl slide and KCl cover slip. The KCl slide was then placed in the sample beam path to obtain the transmission spectrum of the mull. A second slide was also prepared with only Nujol (no sample) and placed in the reference beam path. Thus, by taking a ratio of the sample to reference signals, a pure sample spectrum was obtained with no contribution from the spectral features of Nujol.

The powdered samples chosen for this experiment were ammonium nitrate and urea. In addition to the transmission spectrum obtained by the SC based system, the same samples were also analyzed with a conventional FTIR instrument at approximately the same wavelength resolution (~5 nm). Figures 5.4 and 5.5 show the transmission spectra obtained by the SC system (blue curve) and FTIR (red curve) for ammonium nitrate and urea respectively. A possible reason for the slight mismatch between the two curves could be the differences in beam diameters of the two systems. While the SC instrument had a beam diameter of ~1 cm and covered almost the entire surface area of the cover slip, the beam diameter of the FTIR instrument was only ~2 mm. Thus, differences in positioning of the KCl slide with respect to the beam could have resulted in slightly different spectra if the mull was not uniformly sandwiched with the cover slip (different thickness in different regions) or the distribution of ammonium nitrate within the mull was not uniform. Another difference between the two spectra is the apparent lower noise on the FTIR instruments. This was primarily due to the fact that the FTIR results are the average of 32 scans while the SC results are for a single scan.

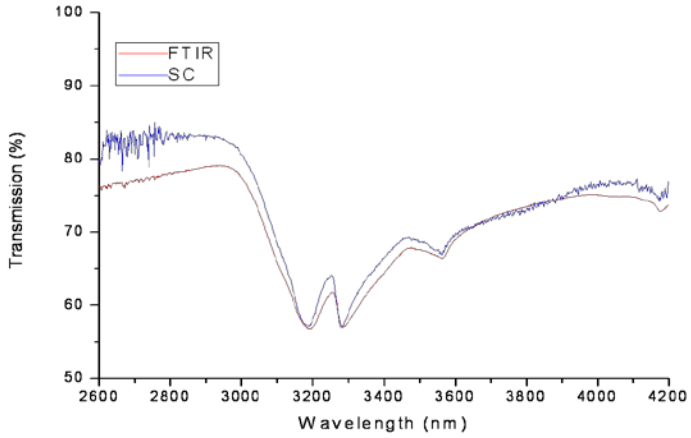

Fig. 5.4. FTIR transmission spectrum of ammonium nitrate

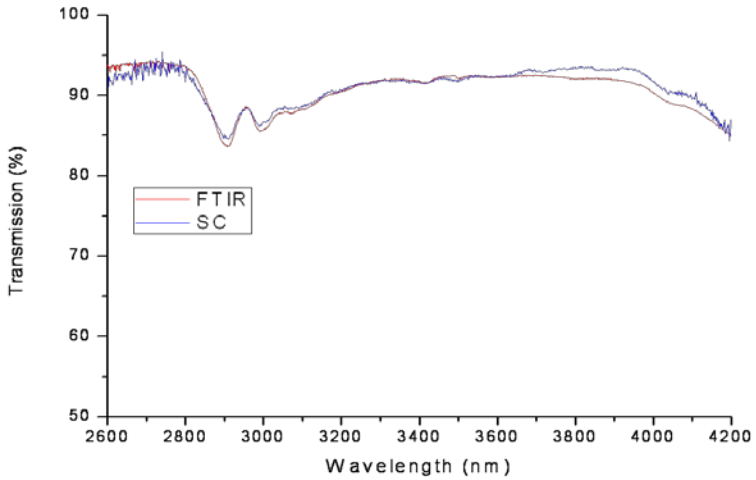

Fig. 5.5. FTIR transmission spectrum of urea

5.4 Experimental setup – reflection spectroscopy

While the results of the previous section proved the feasibility of using the SC light source for transmission spectroscopy applications, a stand-off detection system must necessarily operate in the reflection mode. The experimental setup for a reflection spectroscopy based stand-off detection system is shown in Fig. 5.6. First, the diverging SC output from the ZBLAN fiber is collimated to a 1 cm diameter beam using a 25 mm focal length, 90 degrees off-axis, gold coated, parabolic mirror. To reduce the effects of chromatic aberration, refractive optics are avoided in the setup. All focusing and collimation is done using metallic mirrors that have almost constant reflectivity and focal length over the entire SC output spectrum. The sample is kept at a distance of 5 m from

the collimating mirror, which corresponds to a total round trip path length of 10 m before reaching the collection optics. A 12 cm diameter silver coated concave mirror with a 75 cm focal length is kept 20 cm to the side of the collimation mirror. The mirror is used to collect a fraction of the diffusely reflected light from the sample, and focus it into the input slit of a monochromator. Thus, the beam is incident normally on the sample, but detected at a reflection angle of $\tan^{-1}(0.2/5) \sim 2.3$ degrees. Appropriate long wavelength pass filters mounted in a motorized rotating filter wheel are placed in the beam path before the input slit to avoid contribution from higher wavelength orders from the grating (300 groves/mm, 2 μm blaze). The output slit width is set to 2 mm corresponding to a spectral resolution of 10.8 nm, and the light is detected by a 2 mm x 2 mm liquid nitrogen cooled (77K) indium antimonide (InSb) detector. The detected output is amplified using a trans-impedance pre-amplifier with a gain of $\sim 10^5$ V/A, and connected to a lock-in amplifier setup for high sensitivity detection. The chopper frequency is 400 Hz, and the lock-in time constant is set to 100 ms corresponding to a noise bandwidth of ~1 Hz.

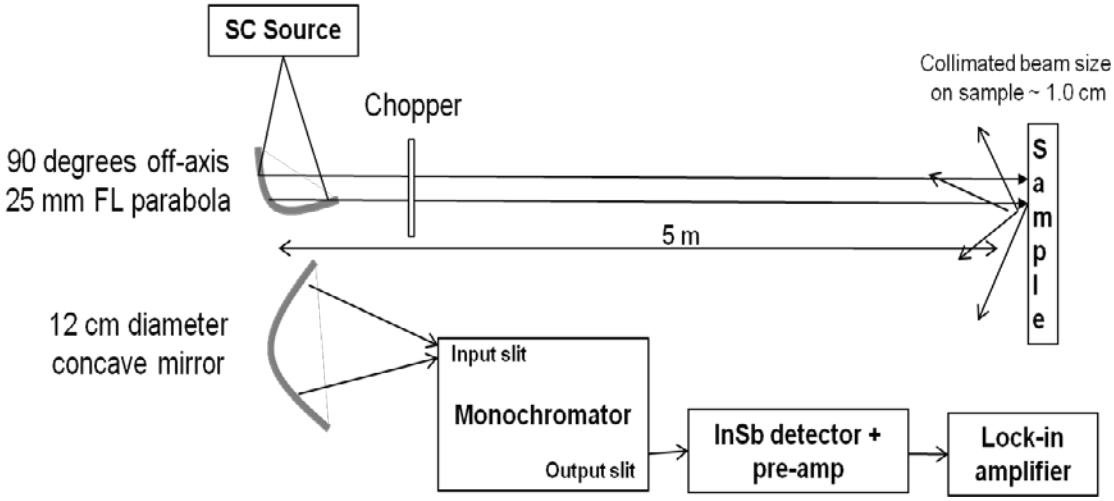

Fig.5.6. Experimental setup for SC based stand-off diffuse reflection spectroscopy

The reflection spectrum of a given sample is obtained using the following procedure. First, a reference scan is obtained using an 'Infragold' diffuse reflectance target as the sample. 'Infragold' from Labsphere Inc. is an electrochemically plated diffuse gold metallic coating that has >95% reflectivity from 1 to 20 μm, and a nearly ideal

Lambertian scattering profile. Although the SC short wavelength edge is 750 nm, the scans we obtain start at 1200 nm due to the rapid fall-off of the grating efficiency as well as detector responsivity at shorter wavelengths. The scan from 1200-4200 nm comprised of 3 different scans, each with a different long pass filter rotated into place via a circular stepper motor. A Silicon filter (1100 nm long pass) is used to scan from 1200-2100 nm, a Germanium filter (1800 nm long pass) to scan from 1800-3400 nm and a 3000 nm long pass filter to scan from 3100-4200nm. The three different sections are then stitched together using the overlap regions to form a single continuous scan from 1200-4200 nm.

After obtaining a reference scan, the 'Infragold' target is replaced with the sample of interest, and a second scan is obtained using the same procedure described above. Since, the beam passes through the same optics in each case, the wavelength dependence of the system due to the SC shape, detector response, grating response etc. is identical for both the reference and sample scans. Thus, dividing the sample scan by the reference scan gives the reflectance spectrum of the sample normalized to a Lambertian reflector kept at the same distance. Some samples cannot be oriented in the vertical plane normal to the collimated SC beam due to their powdered nature. To solve this problem, a fold mirror inclined at 45 degrees is added close to the sample to bend the beam 90 degrees, and allow the sample to be placed horizontally on the table.

After the reference and sample scans are acquired, post-processing of the data is performed in Matlab. The percentage sample reflectance is obtained by dividing the sample scan by the Infragold reference scan, followed by smoothening of the reflectance curve using a 5-point Savitzky-Golay filter [13]. The 3 outlier data points at 1530, 1540 and 1550 nm are also deleted from the final reflectance curve due to the saturation of the lock-in amplifier signal level close to the seed laser wavelength of 1543 nm. Finally, for a better visualization of absorption features as peaks instead of valleys, a mathematical transformation from reflectance to pseudo-absorbance is carried out using the equation, $A = \log(1/R)$ [14].

When a light beam is incident on a sample, it is reflected, scattered and transmitted through the sample. Only the part of the beam that is scattered within a sample and returned to the surface is considered to be diffuse reflection. In order for a one to one comparison with transmission spectroscopy, the sample must be diluted, ground, and mixed with a non-absorbing matrix such as KBr. Diluting ensures a deeper penetration of the incident beam into the sample which increases the contribution of the scattered component in the spectrum and minimizes the specular Fresnel reflection component. The specular reflectance component in diffuse reflectance spectra causes changes in band shapes, their relative intensity, and, in some cases, it is responsible for complete band inversions i.e. Restrahlen bands [15]. Dilution of the sample with a non-absorbing matrix minimizes these effects.

While the dilution technique provides a reflection spectrum that is quantitatively comparable to the transmission spectrum, it is not a practical technique for field applications outside the laboratory setting. Thus, the samples measured in the next section were used in their original form for the reflectance measurements. Due to the very nature of stand-off detection, the samples are measured at angles close to the specular reflection direction. Thus, it is not possible to completely avoid contributions from the Fresnel reflection while intending to measure a diffuse reflection spectrum. In order to accurately identify unknown sample on the basis of their stand-off reflection spectra, there is a need to build a database of relevant sample spectra measured using the same technique i.e. undiluted pure samples measured at near specular reflection angles.

Three sets of solid samples are chosen to demonstrate the stand-off diffuse reflection spectra measurement capability of our system. The first set consists of 'Non-hazardous Explosives for Security Training and Testing' (NESTT) manufactured by the XM Division of VanAken International. These samples contain small amounts of explosives deposited on an inert fused silica powder substrate. The resulting products are non flammable, shock-insensitive and easily transportable, while retaining the unique chemical signature of the explosive that makes them detectable. NESTT samples have previously been used as substitutes for pure explosives in stand-off optical detection using Raman spectroscopy [16]. In our experiments, we use the following samples – trinitrotoluene (TNT), research department explosive (RDX), Pentaerythritol tetranitrate (PETN), and potassium nitrate. The TNT, RDX and potassium nitrate NESTT samples have 8% (by weight) explosives, while the PETN sample has 4%.

The second sample set consists of ammonium nitrate, urea, gypsum and pinewood. Ammonium nitrate and urea are common fertilizers, but are also often used as explosives. These samples are in the form a fine powder, and are filled to a depth of ~5 mm in a shallow glass container. We also measure the reflection spectrum of a 10 cm diameter x 0.5 cm thick Gypsum ($CaSO_4.2H_2O$) disk and a 5 cm x 5cm x 0.5cm piece of pine wood, since these samples are relevant the remote sensing community (minerals and vegetation).

The final set of samples is selected to distinguish between commercial automotive and military vehicle paints based on their reflection signatures. We obtained red, black and green acrylic based spray paints from an auto supply store and sprayed 3 coats on different areas of a sanded aluminum block to make our automotive paint samples. The sample of the military paint consisted of an aluminum block coated with a chemical agent resistant coating (CARC) green paint, and was loaned to us by General Dynamics – Advanced Information Systems (Ypsilanti, MI).

5.5 Experimental Results – Reflection spectroscopy

5.5.1 Sample set #1 – TNT, RDX, PETN, Nitrate NESTT explosives

The chemical formula and structure of the 4 NESTT samples is shown in Fig. 5.7, and the absorbance spectra obtained at a stand-off distance of 5m in Fig. 5.8. For each sample, the positions of the strongest / unique peaks [17-19] have been labeled for clarity. The common broad absorption feature around 2720 nm present in all 4 samples arises due to the O-H stretching vibration of hydroxyl groups from absorbed water in the fused silica host.

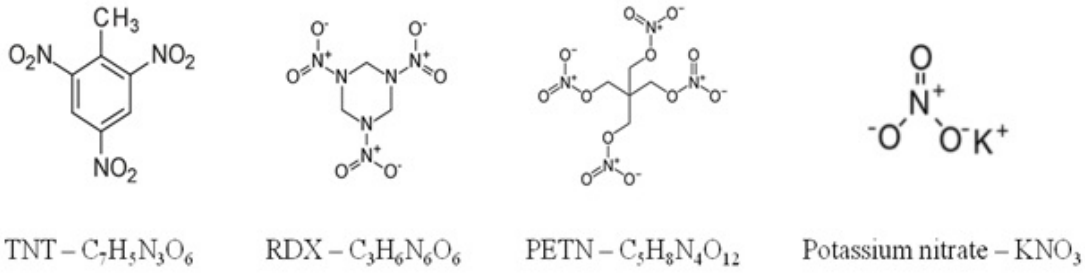

Fig. 5.7. Chemical structure and formula of NESTT samples – TNT, RDX, PETN, Potassium nitrate

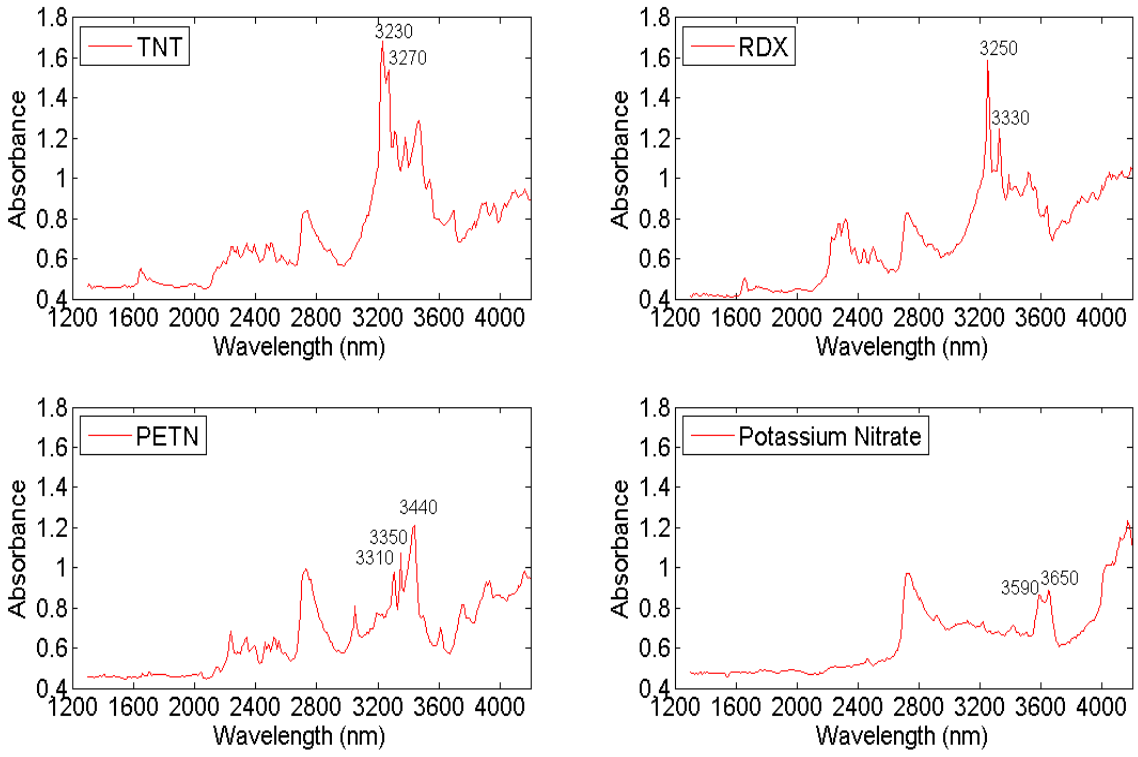

Fig. 5.8. Absorbance spectra of NESTT sample set #1 – TNT, RDX, PETN, Potassium Nitrate.

TNT belongs to a class of compounds known as nitro-aromatics, in which the carbon directly attached to the nitro (NO_2) group is part of an aromatic ring. The strongest peaks in the spectrum observed at 3230 nm and 3270 nm are due to the fundamental C-H stretching vibrations in the aromatic ring. The remaining peaks from 3300-3500 nm are also due to the C-H stretch, but from the alkyl group. We also observe sharp but weak features between 2200-2600 nm, which arise due to the combination between the C-H stretch and C-H bend vibrations. Finally, the features between 3600-3850 nm are due to the first overtone of the nitro group symmetric stretch.

RDX belongs to the nitramines class containing the N-NO_2 bond and also has multiple features in the 3200-3500 nm band due to the C-H stretch vibrations. The two strongest peaks in this region are at 3250 nm and 3330 nm. The spectrum also contains the C-H combination bands from 2200-2600 nm and very weak nitro group overtones from 3600-3850 nm.

PETN is classified as a nitrate ester containing the C-O-NO_2 bond, and its reflection spectrum is characterized by a triplet of peaks at 3310 nm, 3350 nm and 3440 nm due to the C-H stretch vibration from the aliphatic groups. The C-H combination band is also present from 2200-2600 nm while the peak around 3900 nm corresponds to the first overtone of symmetric stretching vibration of the O-NO_2 bond. We will show later in section 4 that the bands from 3200-3500 nm and 2200-2600 nm will be used to distinguish between the three explosive samples due to the unique positions and shapes of various peaks.

Potassium nitrate being an inorganic compound does not contain any absorption features due to the C-H bond present in the other three samples. Instead, the unique spectral feature for this sample is a pair of peaks at 3590 nm and 3650 nm, which arise due to the first overtone of the asymmetric N-O stretching vibration of the nitrate ion (NO_3^-).

5.5.2 Sample set #2- Gypsum, pine wood, ammonium nitrate and urea

The reflection spectrum for the 4 samples is shown in Fig. 5.9. While the absorption features show up as peaks in the absorbance spectrum, they are present as valleys in the reflection spectrum. The predominant spectral features in the Gypsum ($CaSO_4.2H_2O$) reflectance [20] occur due to the fundamental as well as combination bands of the water molecule. These valleys are present at 1450 nm, 1750 nm, 1940 nm and 2860 nm. In addition to the features from water, we also observe small dips in the spectrum at 2220, 2260 and 2480 nm which arise due to the first overtone of the S-O bending vibration. Finally, the valley at 3970 nm occurs due to the first overtone of the –O-S-O stretching vibration of the sulfate (SO_4^{2-}) ion.

The pine wood spectrum [21] comprises of bands due to its main constituents – cellulose, lignin and water. As is the case in the gypsum reflection spectrum, the valleys at 1450 nm, 1920 nm and 2860 nm are due to water. The dip at 2100 nm is due to the first overtone of the C-O asymmetric stretch, the one at 2270 nm due to the combination band of O-H and C-H, and the one at 2490 nm due to combination band of C-H and C-O. Finally, the broad feature around 3450 nm is due to the C-H stretching vibration.

Ammonium nitrate (NH_4NO_3) has 3 prominent features in the near-IR region of the spectrum [22]. The dip at 1270 nm is due to the combination of N-H stretching and N-H bending vibrations, while the dip at 1570 nm is due to the first overtone of N-H stretch. The doublet at 2050 nm and 2140 nm are possibly due to the second overtone of the N-H bending vibrations, while the fundamental N-H stretch appears as a broad feature around 3000 nm.

Urea $(NH_2)_2CO$ has two amide ($-NH_2$) groups joined by a carbonyl (C=O) functional group. The absorption line at 1490 nm occurs due to the third overtone of the C=O stretching vibration, while the line at 1990 nm is due to the second overtone of the same [23].

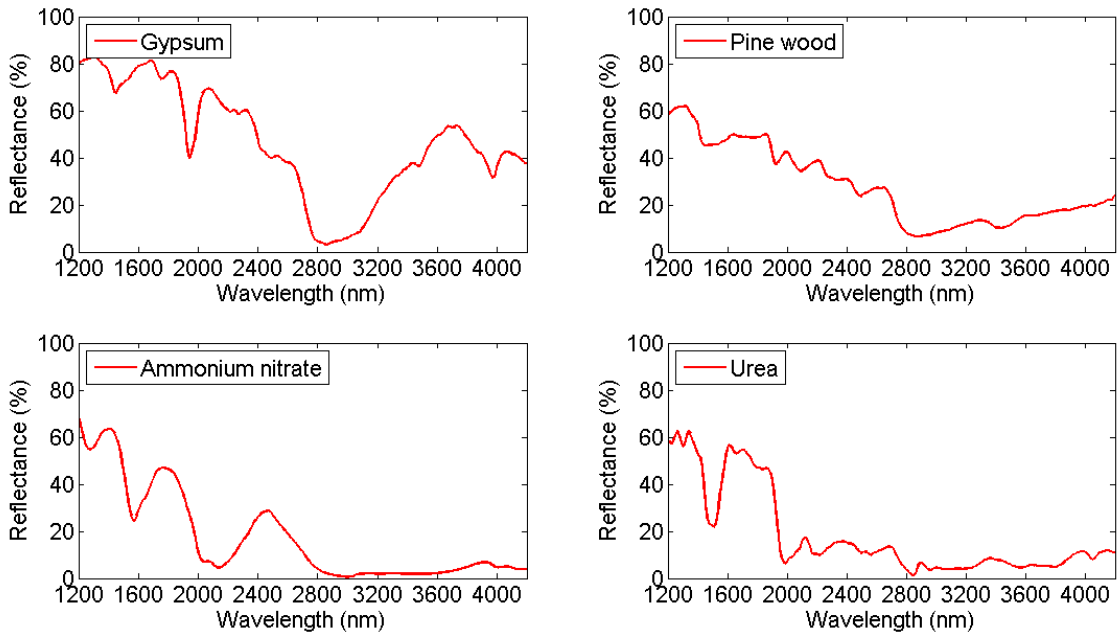

Fig.5.9. Reflection spectra of sample set #2 –Gypsym, Pine wood, Ammonium Nitrate, Urea.

5.5.3 Sample set #3- Automotive and military paints

In our final set of samples, the objective is to distinguish between commercial automotive paints and military grade CARC (chemical agent resistant coating) paint based on the differences in their reflection spectra. The obtained reflection spectra of the three automotive and one military paint samples are shown in Fig.5.10. Unlike the previous sample sets, the paints consist of a complex mixture of many different chemicals, and, hence, it is not possible to identify individual absorption lines. However, we can make some broad observations regarding the spectral features of the paints.

The difference in reflectance levels of the 4 paints can primarily be attributed to the surface finish of the paint coats. While the auto-red has a glossy finish, the auto-green, auto-black and CARC-green paints have a more matt finish. Since our reflection measurement is performed at an angle of only 2.3 degrees away from the specular direction, we expect a higher reflection from the glossy paint. It is important to note that we expect different reflectance levels for the same sample with different surface finish and at different measurement angles. Thus, in section 4, we will demonstrate a sample identification algorithm that is only sensitive to the shape and feature positions of the

spectrum, and not the absolute reflectance level.

Since all 4 paints contain a variety of organic compounds, we observe strong features between 3200-3500 nm from the C-H stretch and from 2200-2600 nm due to the C-H stretch and C-H bend combination band. In addition, the 2850-3150 nm band in automotive red and green paints has absorption features due to the N-H stretch from the Acrylic-melamine base. However, the primary difference between the automotive and CARC paint is the presence of a strong dip between 1200-1850 nm in the latter. We attribute the above feature due to the absorption from Cobalt chromite - a green pigment found in CARC-green [24]. The measured spectrum of CARC-green is in good agreement with that reported in literature [25].

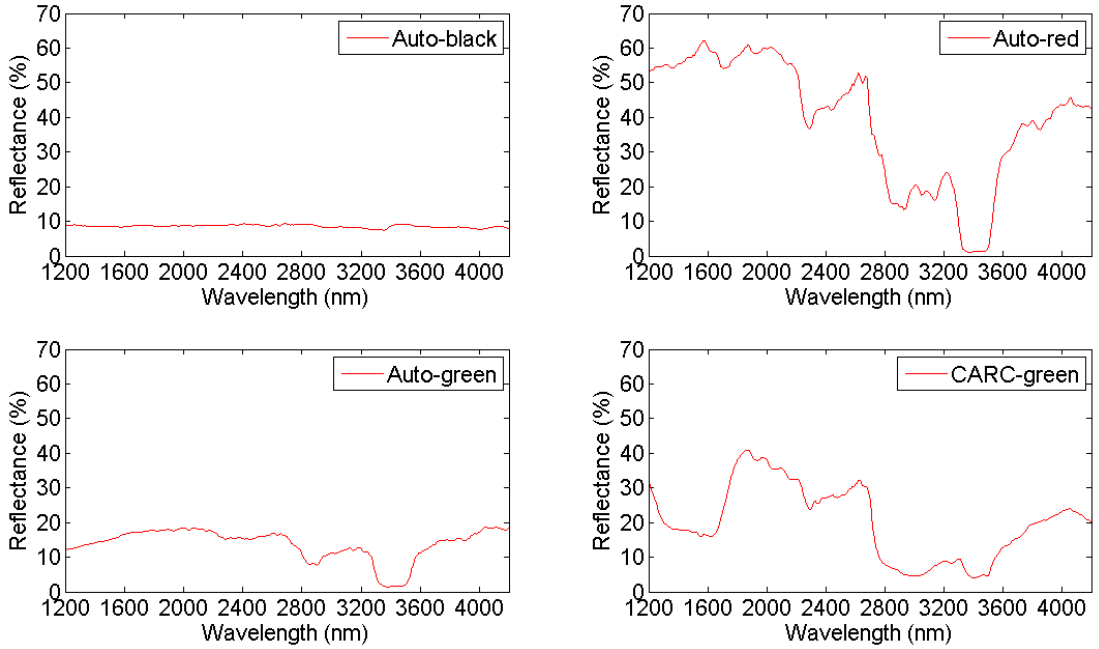

Fig. 5.10. Reflection spectra of sample set #3 –automotive and military CARC paints

5.5.4 Repeatability of reflection measurements

The repeatability of the sample reflectance measurements is directly related to the amplitude stability of the SC source. We measure the magnitude of the SC fluctuations by directly coupling the SC output to the monochromator input, and recording the output versus time for a given wavelength. The lock-in amplifier time constant is kept at 100 ms (the same value as the setup for sample measurements) and corresponds to an effective

noise bandwidth of ~1 Hz. Figure 5.11 shows the variation of the SC output at 4000 nm over a time period of 300s. The plot has been normalized to a mean of 100%, and we obtain a standard deviation of 0.16%. While the plot is shown for a wavelength of 4000 nm, we obtain similar values across the entire SC spectrum. Next, the laser is attenuated by 10 dB using a neutral density filter and the experiment is repeated. We find that the standard deviation is almost identical to the previous case, confirming that the SC fluctuations can be modeled as a fixed root mean square percentage fluctuation superimposed on the mean SC signal level. Thus, the error bar on the reflectance measurements can be equated to the percentage standard deviation (root mean square error) of the normalized SC output.

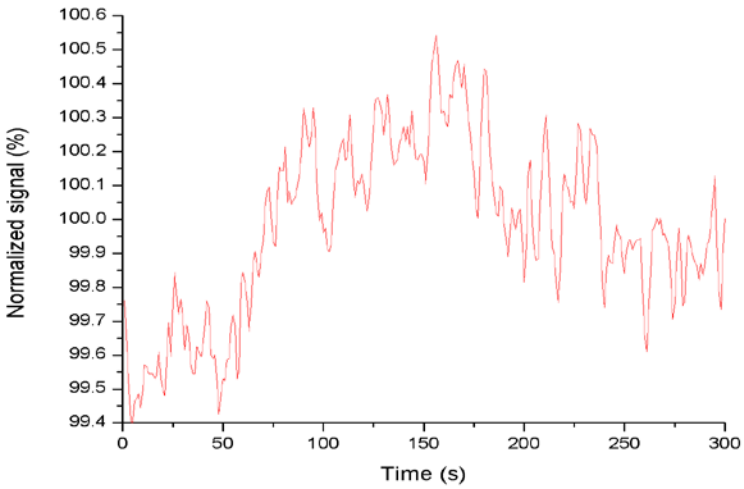

Fig.5.11 Variation of SC output at 4000 nm over 300 seconds.

5.5.5 Comparison of SC and FTIR measurements

In order to verify the validity of our measurements, we compared the reflection spectrum obtained using our setup, with that obtained using a diffuse reflectance accessory in an FTIR spectrometer. As an example, Fig.5.12 shows a comparison of the powdered urea reflection spectrum obtained using the two methods. There is good agreement in the shape and wavelength position of the various spectral features. However, there is a difference in the absolute reflectance levels of the 2 curves. We attribute the difference in scale to the different measurement geometries of the two setups. The SC based setup

described in section 5.4 measures the reflection spectrum of the sample at a fixed angle of 2.3 degrees from the normal. However, the FTIR accessory uses a concave mirror that collects light over almost the entire hemisphere above the sample. Thus, the latter method produces a directionally integrated spectrum, compared to a single direction spectrum from the former. The shape and positions of the absorption lines depends mostly on the chemical composition of the sample, and hence does not change significantly between the two methods. However, the magnitude of light reflected along different directions depends on the sample texture, and thus, is responsible for the scale difference between the two spectra.

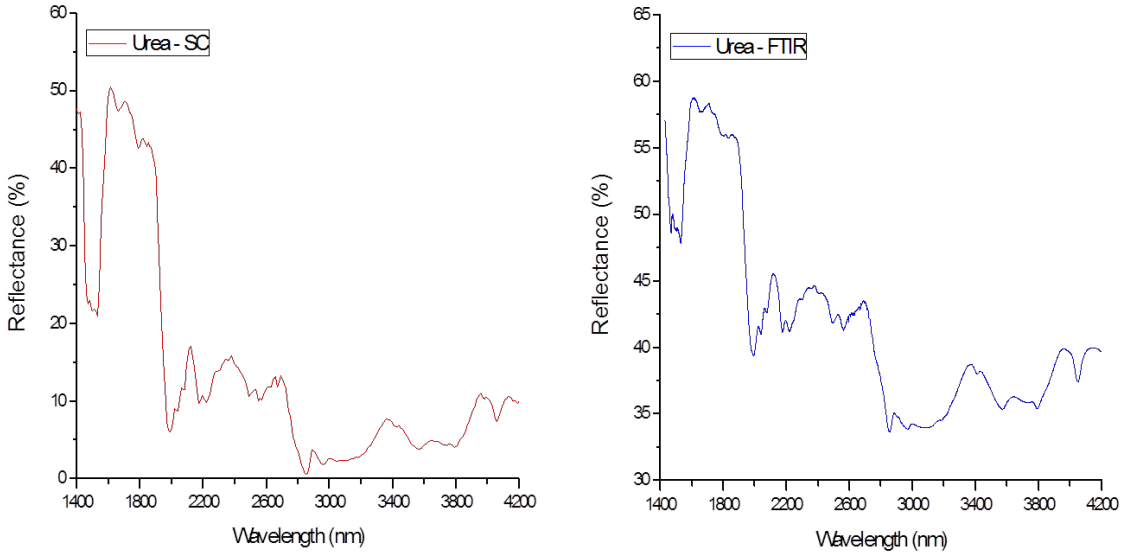

Fig.5.12. Comparison of urea reflection spectrum obtained using the SC and FTIR

5.6 Sample Identification Algorithm

This section describes an algorithm that demonstrates the selectivity of our technique i.e. the ability to distinguish one sample from another based on the unique spectral features of each sample. As an extension, the algorithm can also be used to identify an unknown sample by comparing it against a pre-compiled library of relevant samples. A flowchart describing the different steps of the algorithm is shown in Fig.5.13.

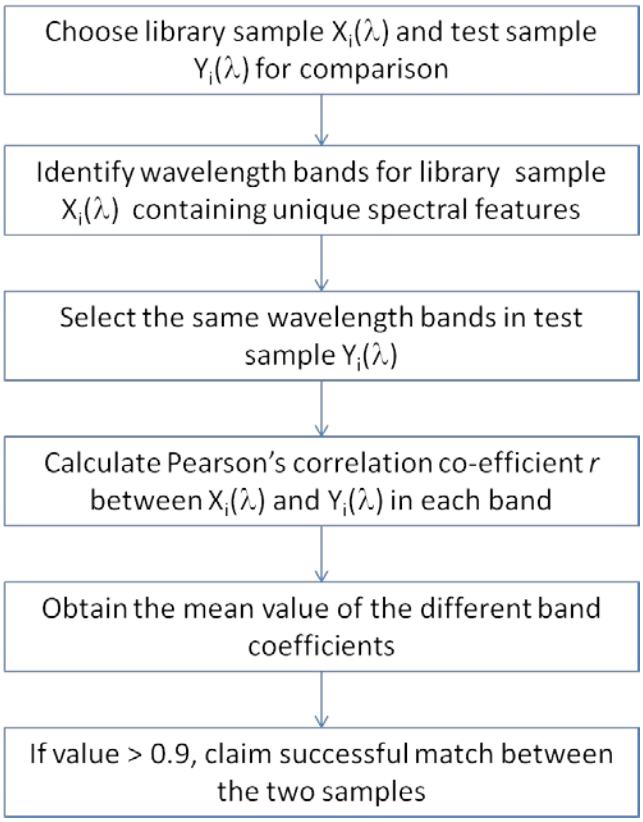

Fig. 5.13. Flowchart describing algorithm to demonstrate selectivity between two samples.

The Pearson's correlation coefficient *r* always lies between -1 and 1, with 1 indicating perfect positive correlation and -1 indicating perfect negative correlation. The equation for *r* is given below.

$$r = \frac{\sum_{i=1}^{n}(X_i - \bar{X})(Y_i - \bar{Y})}{\sqrt{\sum_{i=1}^{n}(X_i - \bar{X})^2}\sqrt{\sum_{i=1}^{n}(Y_i - \bar{Y})^2}}.$$

We test the above algorithm on each of the three sample sets. For each sample in a given set, one or two wavelength bands containing a unique spectral signature is chosen. Tables 5.1, 5.2 and 5.3 show the results of the correlation between different samples in sample set #1, #2 and #3 respectively. As expected, all the diagonal elements of the tables are equal to 1 (auto correlation) while the others are below 0.9, thus confirming the ability to distinguish different samples within a set. Table 3 only contains a single row for CARC paint, as the objective was to distinguish the military paint from the automotive paints and not the difference between the different color automotive paints themselves.

Reference Sample	Band 1	Band 2	Test samples			
			TNT	RDX	PETN	Potassium Nitrate
TNT	2200 – 2600	3200 – 3500	1.00	0.47	0.05	0.01
RDX	2200 – 2600	3200 – 3500	0.47	1.00	-0.05	-0.33
PETN	2200 – 2600	3200 – 3500	0.05	-0.05	1.00	0.03
Potassium Nitrate	3500 - 3700	-	-0.81	-0.46	-0.38	1.00

Table 5.1. Correlation table for sample set#1: NESTT - TNT, RDX, PETN, Potassium nitrate

Reference Sample	Band 1	Band 2	Test samples			
			Ammonium Nitrate	Urea	Gypsum	Pine wood
Ammonium Nitrate	1400-1770	1780-2470	1.00	0.34	-0.25	0.24
Urea	1340-1620	3980-4150	-0.24	1.00	0.15	0.67
Gypsum	1820-2070	3730-4070	-0.16	-0.23	1.00	-0.11
Pine wood	1300-1840	1850-2200	0.62	0.67	0.39	1.00

Table 5.2. Correlation table for sample set #2: Ammonium nitrate, Urea, Gypsum, Pine wood

Reference Sample	Band 1	Band 2	Test samples			
			CARC-green	Auto-black	Auto-red	Auto-green
CARC-green	1200 – 1850	2850 – 3150	1.00	0.21	-0.27	0.17

Table 5.3. Correlation table for sample set #3: Military CARC-green and auto-black, auto-red and auto-green paints

The advantage of the correlation based algorithm we have chosen is the insensitivity to the absolute level of the sample reflectance. The correlation value only depends on the shape and position of the spectral features, and can be used to compare samples measured using different reflection geometries as mentioned in section 5.5.5. While the above algorithm demonstrates proof of concept for distinguishing between distinct samples

using multiple wavelength bands, more sophisticated algorithms [26] have been used by the remote sensing community for distinguishing between geological samples with similar compositions. In addition to the detection of pure samples, algorithms using derivative spectroscopy [27] and multivariate curve resolution [28] have also been demonstrated for the detection of trace amounts in the presence of interfering species.

5.7 Discussion

The limitations and scope for further improvement of the different aspects of the SC based diffuse reflection spectroscopy technique are discussed in this section.

5.7.1 Signal to noise ratio of reflection measurements

We begin by performing a detailed signal to noise ratio (SNR) estimate of our system, which determines the smallest relative percentage change in sample reflectivity that can be measured at a given stand-off distance. The signal voltage measured at the lock-in amplifier can be computed by determining the power reaching the InSb detector after diffuse reflection from the sample. Our analysis assumes a detection wavelength of 4000 nm, and a sample reflectivity of 10%. First, the SC output spectral power density at the detection wavelength is determined from Fig. 4.4 in section 4.3. Next, the power density reaching the sample is calculated after reflection from the collimating mirror, transmission through the chopper, and a second reflection from the turn mirror next to the sample. Assuming the sample to be a Lambertian reflector, the amount of light captured by the concave collection mirror placed a given distance from the sample can also be calculated. Finally, after taking into account the grating efficiency and the monochromator output slit bandwidth, the power incident on the detector can be determined. The voltage signal on the lock-in amplifier is calculated by multiplying the optical power incident on the detector with the detector responsivity, followed by the trans-impedance gain of the pre-amplifier. Using the actual values of the various terms in our system, the analysis is performed below.

Detection wavelength, λ = 4000 nm (assumption)

SC spectral power density, P_{SC} = 1 mW/nm

Mirror 1 reflection, R_{m1} = 95%

Chopper transmission, T_{ch} = 50%

Mirror 2 reflection, R_{m2} = 95%

Sample reflectivity, R_s = 10% (assumption)

Sample to collection mirror distance, d (variable parameter)

Collection mirror radius, r = 6 cm

Spectrometer output slit bandwidth, $\Delta\lambda$ = 10.8 nm

Grating efficiency, η = 27%

InSb detector responsivity, D = 1.9 A/W

Pre-amp trans-impedance gain, $G = 1.07 \times 10^5$ V/A

Signal voltage measured at the lock-in amplifier,

$$V_{signal} = P_{SC} \times R_{m1} \times T_{ch} \times R_{m2} \times R_s \times (\pi/d^2) \times (\pi r^2) \times \Delta\lambda \times \eta \times D \times G = 0.096/d^2 \quad (1)$$

The total noise floor of the measurement is a combination of the detector noise, SC fluctuations, pre-amplifier noise, and lock-in amplifier noise. Since each noise term is independent, the total noise can be computed from the square root of the sum of the squares of the various terms. The detector noise term is calculated by multiplying the shot noise current density (from the dark current) with the trans-impedance gain of the pre-amplifier. As was shown in section 3.4, the SC fluctuations are proportional to the SC output power. Thus, the noise term can be modeled as a fixed root mean square percentage fluctuation with respect to a mean signal level. Finally, we also include contributions to the noise from the trans-impedance pre-amplifier and lock-in amplifier voltage noise. However, we will show later that the last two terms are much smaller compared to the detector and SC noise. Hence, they can be neglected for further analysis.

After computing the total voltage noise density, the total voltage noise in the measurements is calculated by multiplying the noise density with the square root of the detection bandwidth (as set by the lock-in amplifier).

InSb detector dark current, I_{det} = 36 μA (manufacturer spec)

Detector dark current shot noise current density, $i_{det} = (2eI_{det})^{1/2}$ = 3.4 pA/Hz$^{1/2}$

Detector dark current shot noise voltage density, $e_{det} = i_{det}$ x G = 363 nV/Hz$^{1/2}$ (2)

SC noise density, $e_{SC} = 0.0016 * V_{signal}$ nV/Hz$^{1/2}$ (from section 3.4) (3)

Lock-in amplifier noise, e_{lia} = 7 nV / Hz$^{1/2}$ (manufacturer spec)

Detector pre-amp noise, e_{pa} = 20 nV/Hz$^{1/2}$ (manufacturer spec)

Total noise floor density, $e_{tot} = (e_{det}^2 + e_{SC}^2 + e_{lia}^2 + e_{pa}^2)^{1/2} \sim (e_{det}^2 + e_{SC}^2)^{1/2}$ (4)

Lock-in detection bandwidth, B = 1 Hz

Total noise floor, $V_{noise} = e_{tot}$ x $B^{1/2}$ (5)

SNR (linear) = V_{signal} / V_{noise} (6)

SNR (dB) = $10 * \log (V_{signal}/V_{noise})$

The SNR equation can be further simplified for two limiting cases. At a critical sample distance d_c ~ 20.5 m, $e_{SC} = e_{det}$ - using eq. (1) ,(2) and (3).

Case 1: At distances $d << d_c$, $e_{SC} >> e_{det}$, and $e_{tot} \sim e_{SC}$

Thus, SNR = V_{signal} / (0.0016 V_{signal}) = 625 = 28 dB (constant)

Case 2: At distances $d >> d_c$, $e_{det} >> e_{SC}$, and $e_{tot} \sim e_{det}$

Thus, SNR = $(0.096/d^2)/(363e\text{-}9) = 2.6e5/d^2$ (inversely proportional to square of sample distance)

Using the generalized equations (1)-(6), the predicted variation of the SNR with sample distance is shown in Fig. 5.14. The top curve is calculated for the actual experimental noise bandwidth of 1 Hz, while the middle and bottom curves are for higher noise bandwidths of 10 Hz and 100 Hz, corresponding to smaller lock-in time constants of 10 ms and 1 ms respectively. We observe that the curves have two different shapes in two distinct regions. At sample distances below 10m, the curve is flat corresponding to the limiting case 1. We observe a constant SNR~28 dB, 23 dB, and 18 dB respectively for the top, middle and bottom curves. We call this region as the SC fluctuation noise limited region. However, at longer distances corresponding to case 2, there is a constant drop in the SNR with increasing distance. In this region, the SNR is detector noise limited, and the SNR falls by 6 dB for every doubling of the sample distance.

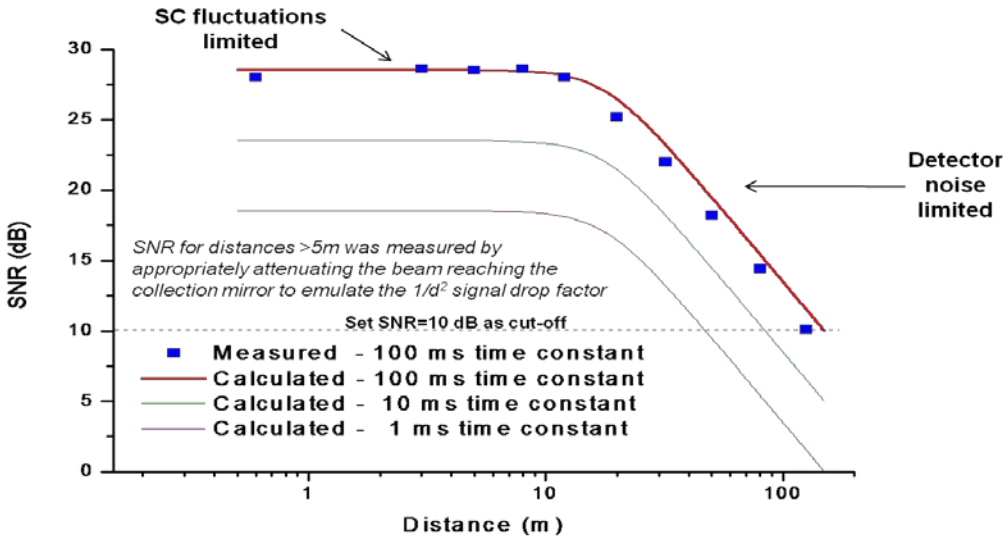

Fig. 5.14. Variation in predicted system SNR versus sample stand-off distance

Finally, we verify the calculations by experimentally measuring the SNR at different distances and comparing it to the predicted value. At a wavelength of 4000 nm, the

reflected signal from a 10% reflectivity sample is acquired for a period of 5 minutes, and the ratio of the mean to standard deviation is defined as the SNR. The available space in our lab limited the maximum sample distance to 5m. The effect of longer sample distances is emulated by keeping the sample at the maximum physical distance of 5m, and adjusting an aperture opening in front of the collection mirror to reduce the collected light by the required $1/d^2$ factor. The experimentally measured results for a 1 Hz noise bandwidth are plotted using square markers in Fig. 5.14, and are found to be in good agreement with the theoretically predicted curve. Future improvements in the short distance SNR can be accomplished using a ratiometric dual beam detection scheme [29] to reduce the effect of the SC fluctuations, and achieve detector noise limited performance.

5.7.2 System sensitivity

The system sensitivity for a given SNR is defined as being equal to the minimum band depth (Fig. 5.15) that can be measured. Under the assumption that a band depth ~ 3 standard deviations above the noise floor can be measured, the system sensitivity expressed as a percentage is equal to 300/SNR. As an example, the SNR at 5m is 625 corresponding to a system sensitivity of 0.48%. Assuming a cut-off value of SNR=10 dB (minimum band depth of 30%), our current system can be used to make measurements up to a distance of 150 m. If the time constant is reduced from 100 ms (1 Hz noise bandwidth) to 10 ms (10 Hz bandwidth) or 1 ms (100 Hz noise bandwidth), the distance is reduced to 85 m or 45 m respectively according to Fig. 5.14. The system sensitivity at large distances can be improved using two methods. First, as discussed earlier in section 4.3, the SC output power can be scaled up further using higher 976 nm pump power and a corresponding increase in pulse repetition rate. Second, the detector noise can be reduced by using a detector with a smaller area, since the noise equivalent power for a photodiode is directly proportional to the square root of the active area.

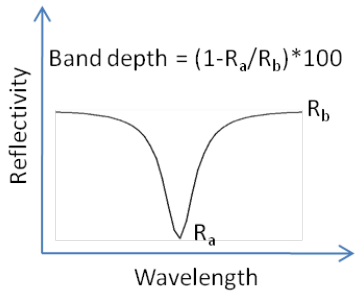

Fig. 5.15. Definition of absorption band depth.

5.7.3 System selectivity

The selectivity of a system is defined as the ability to distinguish between various samples based on their spectral signatures. The conventional 'fingerprint' region of a sample is defined as 6.5-25 μm, as it contains many of the strong fundamental bending and stretching vibrations. However, we have shown in section 5.5 that the SC spectral coverage from 1.2-4.2 μm also contains unique spectral features due to various overtone, combination and fundamental bands. The selectivity of the system was demonstrated in section 4, where the correlation function based algorithm was used to quantitatively demonstrate the dissimilarity between different samples using bands within the 3000 nm wide reflection spectra.

In this chapter, we have demonstrated the measurement of the reflectance spectrum of pure samples or those diluted in high concentrations (4-8%) in a non-absorbing matrix. However, further research needs to be performed on the detection of trace amounts of relevant samples mixed with other samples to determine the selectivity of the technique in the presence of interfering species. The biggest improvement in the system selectivity can be achieved by using a light source with a wider spectral bandwidth that covers more absorption features of a sample. An SC source using a 2 cm long fluoride fiber has recently been demonstrated with a spectrum extending to 6.3 μm and average output power of ~ 20 mW [30]. While the above light source would provide an increase in system selectivity due to the wider bandwidth, it would also produce a decrease in system sensitivity due to the lower output power.

5.7.4 Acquisition time

The feasibility of using a stand-off technique in a real-world field application is strongly dependent on the data acquisition time. Since the lock-in amplifier time constant in our setup is 100 ms, the acquisition time should ideally only be ~0.5 s (5 time constants for the signal to settle). However, the need to rotate the grating and step through each wavelength means that a complete scan from 1200-4200 nm takes ~150 s (300 data points 10 nm apart). The replacement of the current scanning monochromator with a linear detector array spectrograph would reduce the acquisition time by over two orders of magnitude by measuring the entire spectrum in a single shot. By averaging N such shots, the SNR of the measurements can be improved by a factor of $N^{1/2}$. Spectrographs for the visible and near-IR regions using Silicon and InGaAs arrays are widely commercially available. However, the high cost of manufacturing of mid-IR arrays has kept their use largely limited to the defense and astronomical imaging communities [31].

5.7.5 Comparison with other optical stand-off techniques

In this section, we summarize the various performance metrics of our system and provide a comparison with other optical stand-off detection techniques. A recent review by Wallin et. al. [32] on laser based stand-off detection of explosives features a comparison table of different optical techniques. Table 5.4 has been adapted from the above publication, and an additional row with our SC based diffused reflection spectroscopy system has been added to the top. The different techniques are compared on the basis of sensitivity, selectivity, sensitivity to interferents, stand-off distance, detection time, and system complexity.

Method	Sensitivity	Molecular Selectivity	Sensitivity to interferents	Distance (m)	Detection time (s)	Complexity
SC based DRS	High	Medium	NA	~150	~0.5	Low
LIBS	High	Medium	Medium to high	>45	~1	Low to medium
Raman spectroscopy	Medium	High	Low to medium	470	~1	Low
RRS	High	Very high	Low	>30	~10	Medium
CARS	Very high	High	Low	>12	~10	Very high
PF-LIF	Medium	Medium	Medium	~30	~1	Medium

Table 5.4. Comparison of optical stand-off detection techniques

Based on our previous results, we can claim the SC based diffuse reflection spectroscopy technique as having 'high' sensitivity due to the high output power of the SC source combined with the low noise detection scheme. However, like all the other techniques, the system sensitivity decreases with increasing distance for a constant detection time. We have listed the stand-off distance as 150m, since the SNR drops below the cut-off value of 10 dB at larger distances. In terms of selectivity, the SC based DRS technique is inferior compared to the Raman based techniques, and is hence listed as 'medium'. Since the SC spectrum does not cover the conventional molecular vibration fingerprint region of the spectrum beyond 6 μm, we are limited to identifying samples based on the weaker overtone and combination bands, or a limited number of fundamental vibration bands associated with the constituent functional groups. In comparison, the Raman spectroscopy methods usually measure the entire Raman spectral range of ~3800 cm^{-1} containing very unique fingerprints for each sample. Thus, they provide high selectivity, but often at the cost of increased system complexity.

The sensitivity to interferents is closely related to the selectivity of the technique. We expect our technique to detect trace amounts of a substance in the presence of interfering species, provided the absorption feature of the target sample has a strong absorption cross section in a wavelength region where the interfering species does not absorb strongly [33]. However, since we have not experimentally measured the reflection spectra under these conditions, this field in the comparison table has been left blank. Finally, in the detection time column, we have listed the value for our technique as 0.5 s. As discussed earlier, a complete sample scan in our setup takes ~150 s due to a limitation of the scanning monochromator instrument. However, from a fundamental SNR stand-point, the demonstrated light source has enough output power to perform a sample reflectance measurement in just 0.5 s.

5.8 Summary

We measured the diffuse reflection spectrum from 1200-4200 nm of various solid samples at a stand-off distance of 5m, using a mid-IR SC light source with 3.9W average output power and spectrum spanning 750-4300 nm. The first sample set comprised NESTT explosives containing between 4-8% of TNT, RDX, PETN and potassium nitrate on a fused silica substrate. The second sample set consisted of ammonium nitrate, urea, gypsum and pine wood, while the third sample set was made of Aluminum blocks painted with automotive and military CARC paint. For each sample, we observed unique spectral features in the reflection spectrum, attributed to the fundamental and overtone vibration frequencies of the various molecular bonds in the sample structure. A correlation function based algorithm was used to demonstrate system selectivity by quantifying the dissimilarity between various spectra based on selected spectral features in chosen wavelength bands.

Finally, the variation of the SNR with distance was theoretically calculated, and also verified experimentally. For a time constant of 100 ms corresponding to ~1 Hz noise bandwidth, we obtained a SNR ~ 625 at distances <10m. Assuming a minimum

detectable SNR ~ 10, the maximum stand-off distance with the current SC output power and integration time was determined to be ~150m. Future work on the system includes faster acquisition time using a linear detector array spectrograph, and measurement of trace amounts of a sample to determine the sensitivity of the technique to interferents.

References

1. M. P. Fuller, P. R. Griffiths, “Diffuse reflectance measurements by infrared Fourier transform spectroscopy,” Anal. Chem. **50**, 1906-1910 (1978)
2. I. Schneider, G. Nau, T.V.V. King, I. Aggarwal, “Fiber optic near-infrared reflectance sensor for detection of organics in soils,” IEEE PTL. **7(1)**, 87-89 (1995)
3. M.Leona, J.Winter, “Fiber optics reflectance spectroscopy: a unique tool for the investigation of Japanese paintings,” Studies in Conservation. **46**, 153-162 (2001)
4. B.I. Vasil’ev, O.M. Mannoun, “IR differential-absorption LIDARs for ecological monitoring of the environment,” Quant. Elec. **36**, 801-820 (2006)
5. G. Comanescu, C.K. Manka, J. Grun, S. Nikitin, D. Zabetakis, "Identification of Explosives with Two-Dimensional Ultraviolet Resonance Raman Spectroscopy," Appl. Spectrosc. **62**, 833-839 (2008)
6. H. Li, D.A. Harris, B. Xu, P.J. Wrzesinski, V.V. Lozovoy, M. Dantus, "Standoff and arms-length detection of chemicals with single-beam coherent anti-Stokes Raman scattering," Appl. Opt. **48**, B17-B22 (2009)
7. A.J. Hobro, B. Lendl, “Stand-off Raman spectroscopy,” Trend. Anal. Chem. **28**, 1235-1242 (2009)
8. J.L. Gottfried, F.C.D. Lucia Jr., C.A. Munson, A.W. Miziolek, “Laser induced breakdown spectroscopy for detection of explosives residues: a review of recent advances, challenges and future prospects,” Anal. Bionanal. Chem. **395**, 283-300 (2009)
9. V. Swayambunathan, G. Singh, R. C. Sausa, "Laser Photofragmentation–Fragment Detection and Pyrolysis–Laser-Induced Fluorescence Studies on Energetic Materials," Appl. Opt. **38**, 6447-6454 (1999)
10. R. Furstenberg, C. Kendziora, M. Papantonakis, S.V. Stepnowski, J. Stepnowski, V. Nguyen, M. Rake, R.A. McGill, “Stand-off detection of trace explosives via resonant infrared photothermal imaging,” App. Phys. Lett. **93**, 224103 (2008)
11. http://webbbook.nist.gov
12. L.J. Lohr, R.J. Kaier, “Preparation of micro Nujol mulls for infrared analysis”, Anal. Chem. **32**, 301-302 (1960)
13. Savitzky, M. Golay, “Smoothing and differentiation of data by simplified least squares procedures,” Anal. Chem. **44**, 1627-1638 (1964)
14. D.A. Burns, E.W. Ciurczak, “Hand-book of near-infrared analysis,” Third Edition, Marcel Dekker (1992)
15. B. Hapke, “Bidirectional reflectance spectroscopy 1: Theory,”, Journal of Geophysical Research **86**, 3039-3054 (1981)
16. J.C. Carter, S.M. Angel, M. Lawrence-Snyder, J. Scaffidi, R.E. Whipple, J.G. Reynolds, "Standoff Detection of High Explosive Materials at 50 Meters in Ambient Light Conditions Using a Small Raman Instrument," Appl. Spectrosc. **59**, 769-775 (2005)

17. S.V. Ingale, P.U. Sastry, A.K. Patra, R. Tewari, P.B. Wagh, S.C. Gupta, "Micro structural investigations of TNT and PETN incorporated silica xerogels," J. Sol-Gel Sci Technol. **54**, 238-242 (2010)
18. A.Banas, K. Banas, M. Bahou, H.O.Moser, L.Wen, P.Yang, Z.J. Li, M. Cholewa, S.K. Lim, Ch.H. Lim, "Post-blast detection of traces of explosives by means of Fourier transform infrared spectroscopy," Vibrational Spectroscopy **51**, 168-176 (2009)
19. J. Janni, B.D. Gilbert, R.W. Field, J.I. Steinfeld, "Infrared absorption of explosive molecule vapors," Spectrochimica Acta Part A **53**, 1375-1381 (1997)
20. G. Anbalagan, S. Mukundakumari, K.S. Murugesan, S. Gunasekaran, "Infrared, optical absorption, and EPR spectroscopc studies on natural gypsum," Vibrational Spectroscopy **50**, 226-230 (2009)
21. T. Poli, O. Chiantore, M. Nervo, A. Piccirillo, "Mid-IR fiber-optic reflectance spectroscopy for identifying the finish on wooden furniture," Anal. Bioanal. Chem. **400**, 1161-1171 (2011)
22. C. M. Canal, A. Saleem, R.J. Green, D.A. Hutchins, "Remote identification of chemicals concealed behind clothing using near infrared spectroscopy," Anal. Methods **3**, 84-91 (2010)
23. J.E.Stewart, "Infrared Absorption Spectra of Urea, Thiourea, and Some Thiourea-Alkali Halide Complexes," J. Chem. Phys. **26**, 248-255 (1957)
24. Lawrence Berkeley National Laboratory Pigment Database – Cobalt Chromite Green Spinel, http://coolcolors.lbl.gov/LBNL-Pigment-Database/paints/G05.html
25. P.J. Kaste, R.G. Daniel, R.A. Pesce-Rodriguez, M.A. Schroeder, J.A. Escarsega, “Hydrogen plasma removal of military paints: chemical characterization of samples,” Army Research Lab Aberdeen Proving Ground, Report No. A128453 (1998)
26. F.V.D. Meer, W. Bakker, “CCSM: Cross correlogram spectral matching,” International Journal of Remote Sensing **18**, 1197-1201 (1997)
27. T.H. Demetriades-Shah, M.D. Steven, J.A. Clark, "High Resolution Derivatives Spectra in Remote Sensing," Remote Sens. Environ. **33**, 55-64, 1990.
28. N. B. Gallagher, T. A. Blake, P. L. Gassman, J. M. Shaver, and W. Windig, “Multivariate curve resolution applied to infrared reflection measurements of soil contaminated with an organophosphorus analyte,” Appl. Spectrosc. **60**, 713 (2006).
29. M.G. Allen, K.L. Carleton, S.J. Davis, W.J. Kessler, C.E. Otis, D.A. Palombo, and D.M. Sonnenfroh, "Ultrasensitive dual-beam absorption and gain spectroscopy: applications for near-infrared and visible diode laser sensors," Appl. Opt. **34**, 3240-3249 (1995)
30. G. Qin, X. Yan, C. Kito, M. Liao, C. Chaudhari, T. Suzuki, Y. Ohishi, “Ultrabroadband supercontinuum generation from ultraviolet to 6.28 μm in a fluoride fiber”, App. Phys. Lett. **95**, 161103 (2009)
31. J.T. Rayner, D.W. Toomey, P.M. Onaka, A.J. Denault, W.E. Stahlberger, W.D. Vacca, M.C. Cushing, S. Wang, “A medium-resolution 0.8-5.5 micron spectrograph

and imager for the NASA Infrared Telescope Facility," Publications of the astronomical society of the Pacific **115**, 362-382 (2003)
32. S. Wallin, A. Pettersson, H. Ostmark, A. Hobro, "Laser based standoff detection of explosives: a critical review," Anal. Bioanal. Chem., Vol. **395**, 259-274 (2009)
33. L.A. Averett, P. R. Griffiths, "Mid-Infrared Diffuse Reflection of a Strongly Absorbing Analyte on Non-Absorbing and Absorbing Matrices. Part I: Homogeneous Powders," Appl. Spectrosc. **62**, 377-382 (2008)

Chapter 6

Summary and Future Work

6.1 Visible supercontinuum generation

In chapter 2 of my thesis, I have demonstrated power scalable visible supercontinuum generation in a 1.9 μm core PCF pumped by the frequency doubled output of a 1550 nm Er-Yb fiber amplifier. The power scalability was limited by the available 976 nm pump power in the power-amp stage as well as non-linear broadening in the power-amp gain fiber due to its small core size of 10 μm. Detailed simulations based on solving the non-linear Schrodinger equation were also performed to verify that the supercontinuum generation process was initiated by modulation instability. Further, it was predicted that the bandwidth of the supercontinuum could be enhanced using a two step process – MI initiated pulse break up in a short length of anomalous dispersion fiber followed by non-linear broadening in a low dispersion and high n_2 material.

While the above system was suitable for a laboratory demonstration of a visible supercontinuum source, its use in an industrial environment would be hindered by the following two aspects of the design. First, the second harmonic generation process requires the use of multiple lenses in a free space optical configuration to generate the 775 nm light using the temperature controlled PPLN crystal. Second, the output from the frequency doubling stage needs to be coupled into the small core PCF via a high NA microscope objective mounted on a precision xyz stage.

Thus, while the first part of the visible SC laser comprising of the dual stage Er and Er-Yb amplifiers has the advantage of being all-fiber integrated (spliced) and robust, the latter stages suffer from packaging problems associated with free space coupling. One way of solving the problems mentioned above would be to get rid of the free space frequency doubling stage and chose a PCF that could be directly spliced to the output of the first stage amplifier system. However, due to the pump wavelength now being 1550 nm instead of 775 nm, this would result in the generation of a near-IR SC rather than the visible continuum that we were interested in. If the first stage was instead changed to a dual stage 1060 nm Ytterbium (Yb) fiber amplifier [1] and spliced to a PCF with anomalous dispersion at the pump wavelength, we could obtain SC generation in the visible region. Travers et. al [2] demonstrated that by cascading two PCFs with decreasing zero dispersion wavelength, the short wavelength edge of the SC could be extended down to 450 nm. The proposed experimental setup for visible SC generation using the above scheme is shown in Fig. 6.1.

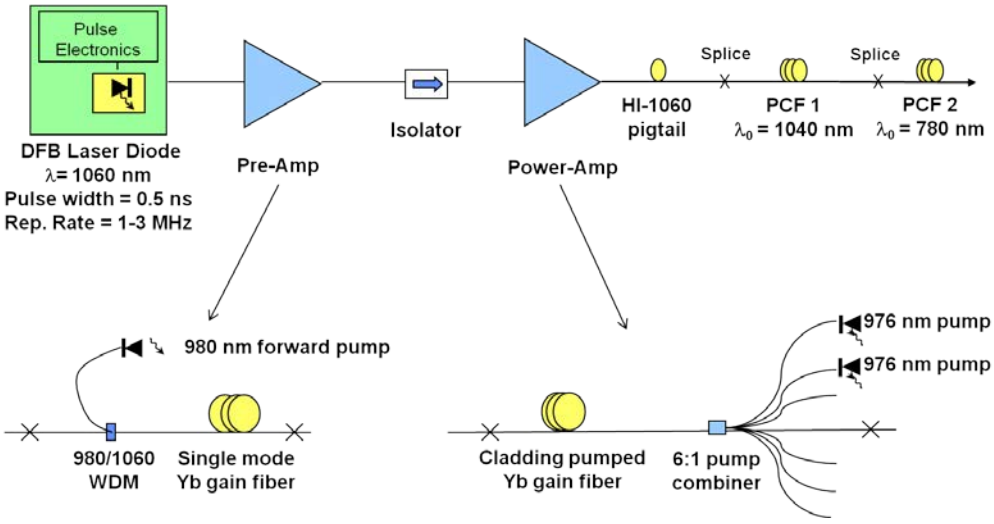

Fig. 6.1. Proposed experimental setup for visible SC generation using a 1060 nm Yb amplifier

A non-mode locked nanosecond pulse width amplifier operating at 1060 nm would retain the feature of being average power scalable through an increase in repetition rate along with a corresponding increase in the pump power. While the peak power used to pump the PCF was limited ~ 1 kW in the Er-Yb based system due to the limited doubling

bandwidth of the PPLN crystal, much higher peak powers could be obtained in the proposed Yb based system. The higher peak power could be used to generate a wider SC spectrum and mitigate the inherent problem of a longer short wavelength edge for 1060 nm pumped systems compared to 775 nm. Another advantage of the new system is the higher efficiency of Yb fiber amplifiers at ~60% compared to ~30% for the Er-Yb amplifiers [3]. Finally, the core size of the PCF with a zero dispersion wavelength of 1040 nm is ~5 μm thereby making it easier to be fusion spliced directly to the output of the power-amp stage.

6.2 Line scan 3D imaging system

Chapter 3 of my thesis demonstrated an application of the previously demonstrated visible SC source in the field of 3D imaging. The light source was coupled to a line scan Fourier domain white light interferometer to obtain 3D images of both flat and curved surfaces with ~100 nm axial and ~15 μm lateral resolution. In particular, the line scan system was used to determine both the height as well as shape defects of ~300 μm high solder balls in a ball grid array by mapping the surface profile over an angular range of +/- 20 degrees from the ball normal. It was found that the measurement of surfaces at larger incidence angles was strongly dependent on the surface roughness of the sample. As an example, measurement over +/- 60 degrees was demonstrated on a 3.17 mm diameter steel ball bearing whose surface was roughened with sand paper. While the demonstrated speed of the line scan system was too slow for practical use in a commercial wafer inspection system, the scan speed was not limited by the SNR of the light source but instead by the slow frame rate of the CCD camera.

Apart from the demonstrated application in the semiconductor industry, the line scan system also has potential use in the automotive manufacturing industry by measuring the surface finish of machined parts. Based on discussions with our sponsor (Coherix Inc.) on this project, a specific application of the line scan sensor was envisioned in the form of a hand held waviness meter. Waviness is the spatial component of surface finish between

form and roughness and is conventionally determined by running a profilometer needle along the surface [4]. This process is slow and also requires the part to be bought to the profilometer. Instead, if a hand held optical profiler similar in shape to a barcode scanner could be simply placed in contact with the surface, an instantaneous height profile along the projected line could be obtained from which the waviness with a desired cut-off wavelength could be extracted.

A possible design of such an instrument is shown below in Fig. 6.2. In order to make the system compact, the visible SC source has been replaced with a superluminescent laser diode (SLD) source [5]. The advantages and disadvantages of this source over the SC source have already been discussed previously in Section 3.5. The setup is in principle identical to the setup from Chapter 3 with mirror M2 and the sample positioned at the ends of the two arms of the interferometer. The exact values of the lens diameters, focal lengths and camera size would have to be chosen to meet the space constraints. The main challenge in building such an instrument would be isolating the interferometer assembly from mechanical vibrations that might cause a path length change between the two arms thereby resulting in erroneous measurements. Table 6.1 lists the expected technical specifications for the proposed system.

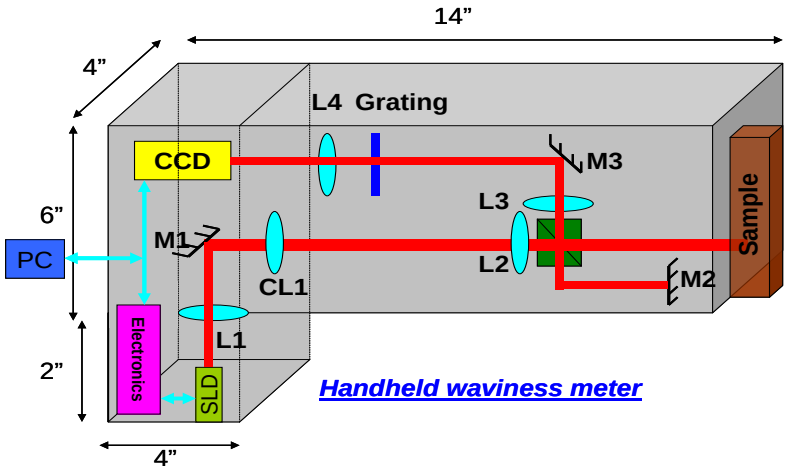

Fig. 6.2. Design of a line scan system based hand-held waviness meter

Parameter	Value
Line length	30 mm
Waviness spatial wavelength	80 μm – 6 mm
Axial (z) resolution	200 nm (with 30x super-resolution)
x- resolution (along the line)	15 μm
y- resolution (thickness of line)	30 μm
Ambiguity range	+/- 0.8 mm
Acquisition time	<1 second

Table 6.1. Expected specifications for a hand-held waviness meter

6.3 Mid-infrared supercontinuum generation

In chapter 4 of my thesis, I demonstrated a mid-IR SC source extending from 0.8-4.3 μm with 3.9 W time averaged output power. The SC was obtained by pumping a 9 m ZBLAN fiber with an 8 μm core and 0.27 NA from the output of a dual stage cladding pumped Er-Yb fiber amplifier. The SC output was power scalable and the maximum output power was only limited by the available pump power and thermal management ability of the setup.

A weak point of the current system is the configuration of the mechanical splice between the power-amp output and ZBLAN fiber. Currently, the two fibers are mounted in a v-groove on a nanomax stage and aligned under a microscope. Due to the slow drift of the stage, the fibers had to be realigned every few days for maximum power throughput. While the remainder of the system is all fiber spliced, the delicate mechanical coupling to the ZBLAN presents a major challenge in designing a robust packaging for the entire laser. Figure 6.3 below shows a prototype mount design (Omni Sciences Inc.) for holding the mechanical splice. While the mount is still initially aligned on a nanomax stage under a microscope, once the alignment is complete, the two halves of the mount are screwed together and removed from the stage. The mount is kept at a constant temperature by a thermoelectric cooler and long term testing over a few weeks has shown that it maintained good coupling. However, the ultimate solution for this problem would

be the ability to successfully splice fused silica fiber to ZBLAN fiber with low loss. Due to the different melting temperatures of the two glasses (265C for ZBLAN and 1200C for fused silica), this has been a very difficult problem to solve and requires careful control of the fiber temperatures using a high-end filament splicer. Preliminary results using a glue splicing method [6] are encouraging having demonstrated splices with <1 dB loss. But, the results were obtained for average power levels of a few mW and the ability of the splice to withstand power levels three orders of magnitude higher is yet to be proven.

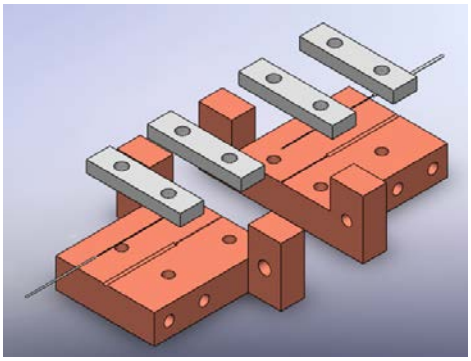

Fig. 6.3. Mechanical mount for coupling power-amp output fiber to ZBLAN fiber

Another limitation of our system is the poor efficiency of power generation in the long wavelength band beyond 3.8 μm. For a modulated pump power of 52W, we generate ~510 mW beyond 3.8 μm, corresponding to an efficiency of ~1%. Ojas et. al. [7] demonstrated a novel technique to improve the efficiency by 2.5x by breaking the continuum process into two stages separated by an intermediate amplification stage. First, an Er-Yb system operating at 1.55 μm was used to generate SC extending to ~2.2 μm in a standard fused silica SMF. Next, a high efficiency Thulium (Tm) fiber amplifier was used to amplify the wavelength components around 2 μm, before coupling the output into an 8m long ZBLAN fiber. The improvement in efficiency was attributed to two main factors. The first was the higher inherent efficiency of Tm amplifiers (~55%) compared to Er-Yb amplifiers (~30%). The second was the increase in quantum efficiency by starting the SC generation process closer (2 μm instead of 1.55 μm) to material absorption edge of the ZBLAN fiber.

Finally, we discuss the possibility of extending of the long wavelength edge of the SC. Previous work by Xia et. al. had shown the ultimate long wavelength limit of a ZBLAN based SC is determined the inherent material loss which exceeds 1 dB/m beyond 4.5 μm. However, the material loss limit can be overcome by reducing the length of the fiber and increasing the peak power to generate a broader SC in a shorter length of fiber. Qin et. al. [8] demonstrated SC extending to 6.28 μm in a ~2 cm long fluoride fiber pumped by a 1450 nm femtosecond laser with 50 MW peak and 20 mW average power. The SC long wavelength edge can also be extended by using fiber made from Tellurite glass which has ~10x higher Raman gain coefficient [9] compared to ZBLAN, thereby enabling the use of shorter lengths. Using ~17 kW peak power pulses at 1.55 μm, SC generation out to 4.8 μm with 90 mW average power has been demonstrated in just 0.8 cm length of Tellurite fiber [10]. However, the maximum power demonstrated to date with Tellurite fibers is ~1.2W [11] indicating difficulty in high quality fiber fabrication.

6.4 Mid-infrared spectroscopy

In the final part of my thesis, the mid-IR SC source was used to demonstrate its application in the field of stand-off reflection spectroscopy. The reflection spectra of a wide range of sample types such as explosives, paints and fertilizers were measured at a distance of 5m and could be distinguished from each other based on correlation functions in unique spectral bands. SNR calculations confirmed that the maximum distance was limited only by the available space in our lab and a reflection spectrum with SNR = 10 dB could be obtained at a distance of ~150m with a 100 ms time constant.

At distances <10m, it was found that the SNR was limited by the SC fluctuations and not the detection noise floor. Thus, for applications that operate at these distances, it would be useful to develop a dual beam ratiometric measurement technique that improved SNR by cancelling the SC fluctuations in each arm. An additional advantage of the dual beam technique would be to eliminate the need for a reference scan before each sample scan that is currently required to remove the effect of the SC spectral shape. With

a dual beam technique, the only parameter that needs to be accurately determined is the split ratio of the beam splitter versus wavelength. This parameter only needs to be determined once and can then be treated as a constant for all future measurements. Changes in the SC spectrum shape over time would no longer affect the reflection measurements as the relevant quantity would no longer be the absolute power level but rather the split ratio between the two arms. Figure 6.4 shows the proposed experimental setup for the dual beam technique. The use of 2 choppers running at different frequencies allows the use of two lock-in amplifiers to independently detect the signal in each arm. By taking a ratio of the signal in each arm at each wavelength, common mode intensity fluctuations of the SC light source are expected to be cancelled out while differences in reflectivity between the sample and reference (Infragold) will be preserved.

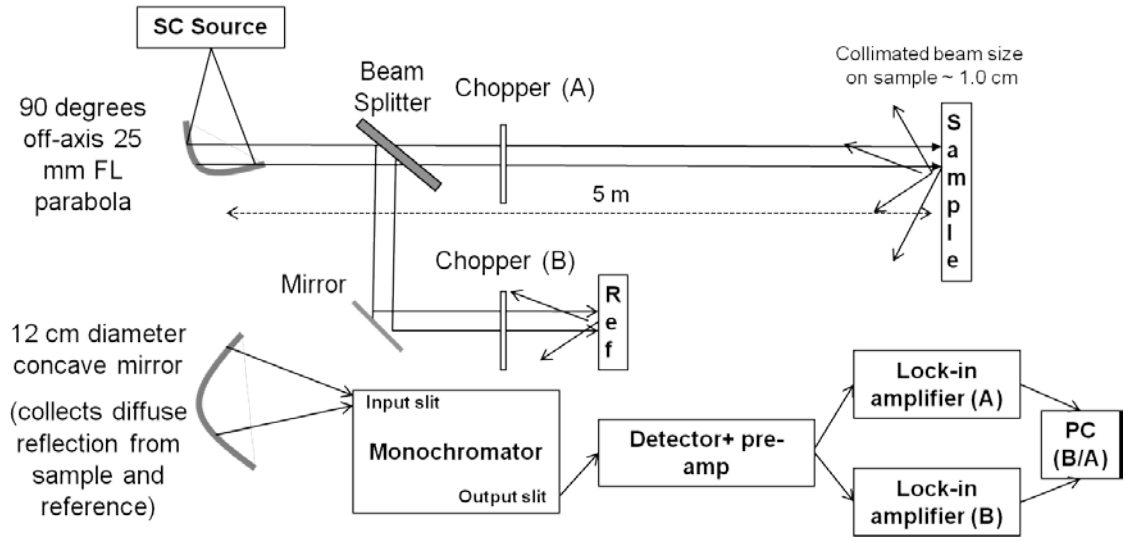

Fig. 6.4. Proposed dual beam detection setup for cancellation of SC fluctuations

While chapter 5 demonstrated the use of the SC source for stand-off detection up to ~150m, modifications to the light source can enable its use in other fields such as hyper spectral imaging from aircraft. Current hyper-spectral imaging systems use the sun as the light source, and the acquired reflection spectrum is limited to below 2.5 μm, allowing the use of inexpensive Silicon and InGaAs detector arrays. Unlike the sun, an active broadband illumination source such as the SC can be used at any time of the day and is less sensitive to ambient weather conditions. However, the sampled area on the ground

needs to be kept small enough to ensure that the spectral density per unit area of the SC source equals or exceeds that of the sun. While our current SC source extends to 4.3 μm, the reduction of the long wavelength edge to 2.5 μm can be made by replacing the ZBLAN fiber with a short length of high non-linearity fused silica fiber. The fused silica fiber can be directly spliced to the power-amp output, and does not have end-degradation issues like the ZBLAN. Thus an all fused silica near-IR SC system will be more robust and can be scaled up to higher average powers compared to the ZBLAN based mid-IR SC system.

Lastly, we discuss some applications of the supercontinuum source in the field of health and medicine. Many biological targets have their fundamental vibration absorption bands in the mid-IR wavelength regime. For example, proteins show primary absorption in the 2.8-3.2 μm range due to the N-H and O-H bands, while lipids exhibit absorption in the 3.2-3.6 μm range associated with the C-H stretching vibration. Using an FTIR, Paluszkiewicz et. al. [12] demonstrated spectral differences between non-cancerous, cancerous, and hyper-plastic human prostate tissues. Since the mid-IR SC is output from a fiber, it is well suited for an in-vivo catheter based spectroscopic diagnostic tool. In addition to diagnosis, the SC can also be used for selective ablation of tissues by using band pass filters to select the appropriate portion of the spectrum [13]. SC sources in the visible and near-IR region of the spectrum have also been used for optical coherence tomography, a technique which provides high resolution cross-section images of internal tissues in a biological sample [14]. Broad bandwidth light sources are desirable for OCT, because they give rise to short temporal coherence length, and determine the axial resolution of the system.

References

1. F.D. Teodoro, C.D. Brooks, “Multistage Yb-doped fiber amplifier generating megawatt peak-power, subnanosecond pulses,” Opt. Lett. **30**, 3299-3301 (2005)
2. J.C. Travers, S.V. Popov, J.R. Taylor, "Extended blue supercontinuum generation in cascaded holey fibers," Opt. Lett. **30**, 3132-3134 (2005)
3. J. Limpert, T. Schreiber, T. Clausnitzer, K. Zöllner, H. Fuchs, E. Kley, H. Zellmer, and A. Tünnermann, "High-power femtosecond Yb-doped fiber amplifier," Opt. Express **10**, 628-638 (2002)
4. J. Raja, B. Muralikrishnan, S. Fu, “Recent advances in separation of roughness, waviness and form,” Journal of precision engineering **26**, 222-235 (2002)
5. T. Ko, D. Adler, J. Fujimoto, D. Mamedov, V. Prokhorov, V. Shidlovski, S. Yakubovich, "Ultrahigh resolution optical coherence tomography imaging with a broadband superluminescent diode light source," Opt. Express **12**, 2112-2119 (2004)
6. M.M. Kozak, W. Kowalsky, R. Caspary, “Low-loss glue splicing method to join silica and fluoride fibers,” Elec. Lett. **41**, 897-899 (2005)
7. O. Kulkarni, V. Alexander, M. Kumar, M.J. Freeman, M.N. Islam, F.L. Terry Jr., M. Neelakandan, A. Chan, “Supercontinuum generation from ~1.9-4.5 μm in ZBLAN fiber with high average power generation beyond 3.8 μm using a Thulium doped fiber amplifier,”, Accepted for publication in JOSA B (2011)
8. G. Qin, X. Yan, C. Kito, M. Liao, C. Chaudhari, T. Suzuki, Y. Ohishi, “Ultrabroadband supercontinuum generation from ultraviolet to 6.28 μm in a fluoride fiber,” App. Phys. Lett. **95**, 161103 (2009)
9. M.D. O'Donnell, K. Richardson, R. Stolen, C. Rivero, T. Cardinal, M. Couzi, D. Furniss, A.B. Seddon, “Raman gain of selected tellurite glasses for IR fibre lasers calculated from spontaneous scattering spectra,” Opt. Materials **30**, 946-951 (2008)
10. P. Domachuk, N. A. Wolchover, M. Cronin-Golomb, A. Wang, A. K. George, C. M. B. Cordeiro, J. C. Knight, and F. G. Omenetto, "Over 4000 nm bandwidth of mid-IR supercontinuum generation in sub-centimeter segments of highly nonlinear tellurite PCFs," Opt. Express **16**, 7161-7168 (2008)
11. K. Li, G. Zhang, L. Hu, “Watt-level ~2 μm laser output in Tm^{3+}-doped tungsten tellurite glass double-cladding fiber,” Opt. Letts. **35**, 4136-4138, (2010)
12. C. Paluszkiewicz, W. M. Kwiatek, A. Banas, A. Kisiel, A. Marcelli, and A. Piccinini, “SR-FTIR spectroscopic preliminary findings of non-cancerous, cancerous, and hyperplastic human prostate tissues,” Vib. Spectrosc. **43**, 237-242 (2007)
13. K. Ke, C. Xia, M. N. Islam, M.J. Welsh, M.J. Freeman, "Mid-infrared absorption spectroscopy and differential damage in vitro between lipids and proteins by an all-fiber-integrated supercontinuum laser," Opt. Express **17**, 12627-12640 (2009)
14. A.M. Zysk, F.T. Nguyen, A.L. Oldenburg, D.L. Marks, S.A. Boppart, “Optical coherence tomography: a review of clinical development from bench to bedside,” J. Biomed. Opt. **12**, 051403 (2007)